2024

The Reconstruction of Climate in Beringia by analysis of Glycerol Dialkyl Glycerol Tetraether (GDGT) Distributions using High Performance Liquid Chromatography Mass Spectrometry (HPLC-MS).

Pankhurst, Lauren Beth

https://pearl.plymouth.ac.uk/handle/10026.1/22327

COPYRIGHT STATEMENT

UNIVERSITY OF PLYMOUTH

The Reconstruction of Climate in Beringia by analysis of Glycerol Dialkyl Glycerol Tetraether (GDGT) Distributions using High Performance Liquid Chromatography – Mass Spectrometry (HPLC-MS).

by

Lauren B. Pankhurst

A thesis submitted to the University of Plymouth

in partial fulfilment for the degree of

Research Masters

School of Geography, Earth and Environmental Sciences

April 2024

Dedicated to Vanessa Ansell who always believed in my academic and personal successes. You may be gone, but your belief in me made this entire thesis possible.

Acknowledgements

Authors Declaration

At no time during the registration for the degree of Research Masters has the author been registered for any other University award without prior agreement of the Doctoral College Quality Sub-Committee.

Work submitted for this research degree at the University of Plymouth has not formed part of any other degree either at the University of Plymouth or at another establishment.
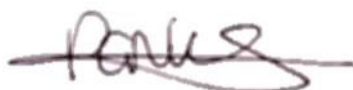
A programme of advanced study was undertaken, which included taught modules:

GEES506 – Climate Change: Science & Policy
GEES519 – Environmental Knowledge: From Field to Stakeholder

Word count of main body of thesis: 17,800 words

Signed:

Date: 08/04/23

Abstract

Lauren Beth Pankhurst

The Reconstruction of Climate in Beringia by analysis of Glycerol Dialkyl Glycerol Tetraether (GDGT) Distributions using High Performance Liquid Chromatography - Mass Spectrometry (HPLC-MS).

The reconstruction of past environments, including temperatures, aids in the production of climate models which predict how the Earth will respond to future climatic changes that are occurring at an accelerated rate, due to global warming. High-latitude seas, including the Bering Sea, are sensitive to changes in global climate, across both glacial and interglacial timescales. Membrane lipids synthesised by archaea and bacteria are retained within the sediment and when extracted give evidence to the environmental conditions present during the organism's lifetime. The membrane lipids are structured in a way that is chemically favourable to their environment, and calibrations derived in other works were used to reconstruct paleoclimates herein.

Thirty polar sediment extracts were analysed by high-performance liquid chromatography coupled via atmospheric pressure chemical ionisation to mass spectrometric detection (HPLC-APCI-MS). Glycerol dialkyl glycerol tetraether (GDGT) ratios within the extracts were used to reconstruct sea surface temperatures (SSTs), mean air temperatures (MATs) and pH. Climatic and environmental parameters were successfully assessed and reconstructed using isoprenoid GDGTs (isoGDGTs), finding that GDGT distributions were characteristic of the open marine environment in most cases. Temperatures were found to be lowest on the transition from marine isotope stage (MIS) 6 to 5, while they peaked as MIS 5 closed. SSTs appeared to get cooler throughout glacial periods, while interglacial times were much more variable, particularly within MIS 5. Consideration was also given to the origin of the isoGDGTs, with the deep-water contribution found to be greatest across the 160-thousand-year (kya) period investigated. Branched GDGTs (brGDGTs) were also present, in lesser quantities and were used to determine MAT (between -5.8 and 10.4 °C) and pH (6.7 – 8.2) The findings showed a significant relationship between the GDGT distributions and numerous environmental proxies.

Table of Contents

List of Figures

List of Tables

Commonly used symbols and abbreviations

ACR	Atlantic Cold Reversal
AMOC	Atlantic Meridional Overturning Circulation
APCI	Atmospheric Pressure Positive Ion Chemical Ionisation
ASE	Accelerated Solvent Extraction
B/A	Bølling/Allerød
brGDGT(s)	Branched Glycerol Dialkyl Glycerol Tetraether(s)
BSC	Bering Slope Current
BSS	Bering Sea Shelf
Cal BP	Calendar years before present
CCSF	Core Composite depth below Sea Floor
CH_4	Methane
CIE	Carbon Isotope Excursion
CO_2	Carbon dioxide
DCM	Dichloromethane
GC-FID	Gas Chromatography Flame Ionisation Detection
GC-MS	Gas Chromatography Mass Spectrometry
GDGT(s)	Glycerol Dialkyl Glycerol Tetraether(s)
GHG(s)	Greenhouse Gas(es)
G-IG	Glacial-Interglacial
HPLC-APCI-MS	High Performance Liquid Chromatography Coupled via Atmospheric Pressure Chemical Ionisation to Mass Spectrometric Detection
IODP	Integrated Ocean Drilling Program
IPCC	International Panel on Climate Change
isoGDGT(s)	Isoprenoid Glycerol Dialkyl Glycerol Tetraether(s)
kya	Thousand Years
LC-MS	Liquid Chromatography Mass Spectrometry
LGM	Last Glacial Maximum
Ma	Million Years
MAE	Microwave Assisted Extraction
MAT	Mean Annual/Air Temperature
MBT	Methylation Index of Branched Tetraethers

mbsf	Metres Below the Sea Floor
MeOH	Methanol
MIS	Marine Isotope Stage
MPT	Mid-Pleistocene Transition
NH	Northern Hemisphere
NPDW	North Pacific Deep Water
OM	Organic Matter
SST(s)	Sea Surface Temperature(s)
TEX$_{86}$	TetraEther indeX of tetraethers consisting of 86 carbon atoms
TOE	Total Organic Extract
YD	Younger Dryas
δ^{13}C	Carbon Isotope Composition
δ^{18}O	Oxygen Isotope Composition

Chapter 1: Literature Review

1.1 Introduction

The current climate change episode is threatening humanity and biodiversity with irreversible and unwanted changes across the biosphere (Kaushik *et al.*, 2020). Natural and anthropogenic systems are undergoing unprecedented changes which are accelerating the current global warming event (Cox *et al.*, 2000). The reconstruction and quantification of previous climatic changes across the Earth's system provides data that can be used to test and refine climate models, which contributes to better predictions of future climatic changes (Harrison *et al.*, 2015; Schmidt *et al.*, 2014). Earth's climate is variable and has undergone glacial and interglacial cycling over millennial timescales. The current warming period is not a new phenomenon; however, temperatures are rising at an unprecedented rate (IPCC, 2021). Present day atmospheric carbon dioxide (CO_2) concentrations are higher than at any point in the last 2 Ma and atmospheric methane (CH_4) concentrations today are at levels not reached in over 800 thousand years (kya; IPCC, 2021), as determined through paleoclimatic research and reconstructions.

Paleoclimatology is the study of Earth's climate history at a time for which measurements were not directly taken. To be able to define past climate changes different proxy records can be exploited. This chapter forms a literature review wherein short term paleoclimates, spanning the Quaternary, are discussed globally and on a more localised scale, focusing in on the high-latitude location of the Arctic and the Bering Sea, as climate change events have been found to be much stronger at high-latitudes (Bernardi *et al.*, 2018; Kent *et al.*, 2003; Rohling *et al.*, 2012; Zachos *et al.*, 2006). The current

knowledge of biomarkers, specifically Glycerol Dialkyl Glycerol Tetraethers (GDGTs), are then reviewed, including their source, structure and how they came to have an application in paleoclimatology, before finally discussing advances in the methodology used to extract, isolate and analyse them.

1.2   Climate Change and the Carbon Cycle

The carbon cycle describes the processes in which carbon compounds in biota, both living and dead, are interconverted through the atmosphere, hydrosphere, cryosphere and the lithosphere. This is becoming increasingly important as Earth's climate is being rapidly altered due to human activity increasing emissions of greenhouse gases (GHGs) including CO_2 and CH_4. The warmer temperature trends generally lead to more extreme weather events due to natural feedback cycles. Ocean acidification, due to the dissolution of raised atmospheric CO_2, can have catastrophic consequences for marine biota and as atmospheric CO_2 emissions increase, carbon sinks within the ocean and land hold greater amounts of carbon, sequestering approximately half the total CO_2 emitted (Figure 1.1; Friedlingstein *et al.*, 2020). Forests, soils and wetlands are also considered carbon sinks; however, as deforestation, drought and land-use changes increase, these natural sinks could become net sources of carbon (Kaushik *et al.*, 2020; Yang *et al.*, 2018).
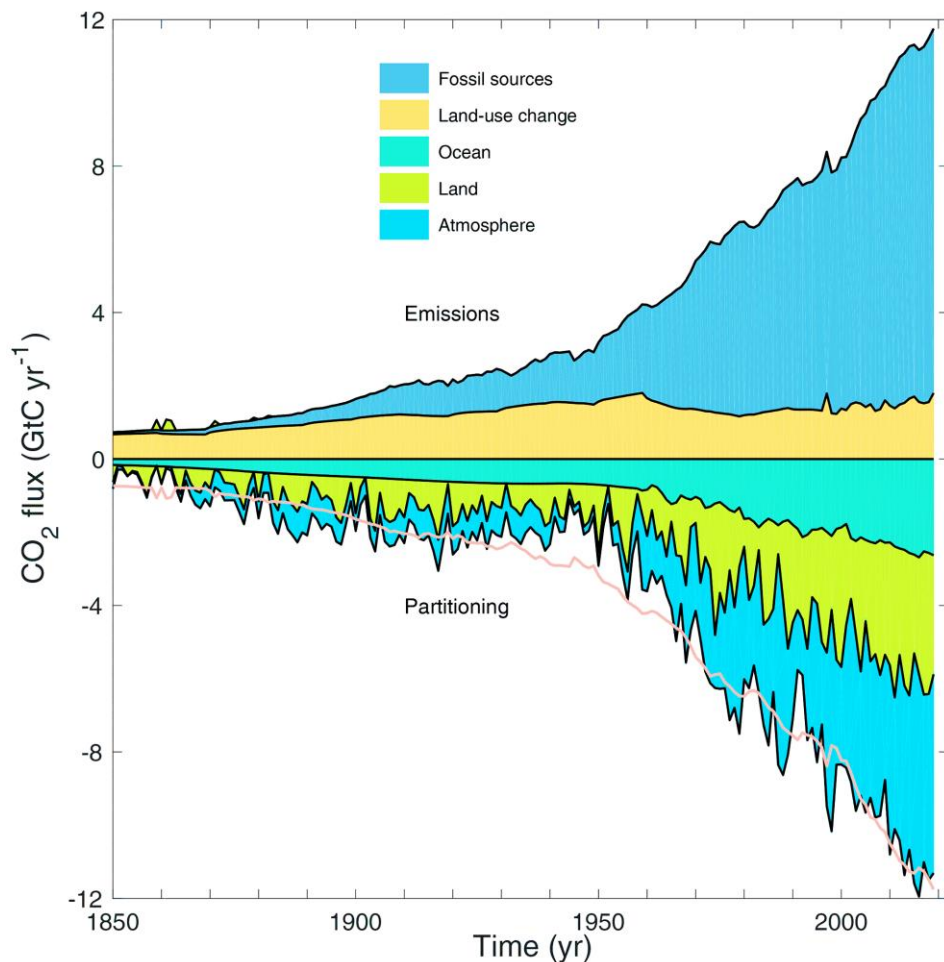
Figure 1.1. Combined components of the global carbon budget in GtC yr^{-1}, illustrating carbon dioxide emissions from fossil sources and land use change and their respective partitioning across the ocean, land and atmosphere. The pink line denotes the sum of the emissions, and sequestered CO_2 quantities. Figure taken from Friedlingstein *et al.* (2020).

The increase in atmospheric CO_2 increases the efficiency of photosynthesis and widens the concentration gradient between the atmosphere and oceans, driving the dissolution of CO_2 into the ocean (Thompson *et al.*, 2017). These negative feedback cycles aid in the reduction of atmospheric CO_2. However, there are also positive feedback mechanisms involved in climate change, including the decreased solubility of CO_2 in warmer waters (Friedlingstein, 2015). Warmer oceans absorb less CO_2, therefore more remains in the atmosphere. There is

also a positive feedback mechanism attributed to sea ice, the surface albedo feedback. Sea ice is bright white and when covered in snow has a high albedo, meaning it has a high reflectivity. However, as the snow and sea ice melt, on seasonal timescales and over larger timeframes, this albedo decreases until a major proportion of the sunlight is instead absorbed by the oceans, triggering additional melting.

There have been major climatic events in Earth's past where a large emission of GHGs over a relatively short time period have accelerated global warming episodes. These sudden and large-magnitude carbon-based perturbations are visible in carbon isotope data spanning back millennia. For example, on the transition between the Palaeocene and Eocene epochs, approximately 56 million years (Ma) ago, a large temperature rise of 5 – 8 °C ensued following an increase in sea level. A rapid increase in atmospheric carbon (ca. 2000 GtC), predominantly CH_4, occurred, causing a negative carbon isotope excursion ($\delta^{13}C$; CIE) event, recorded in marine sedimentary rocks, termed the Palaeocene-Eocene Thermal Maximum (PETM; Haynes & Hönisch, 2020; Sluijs *et al.*, 2008; Zachos *et al.*, 2005; Zachos *et al.*, 2003). Before this, the Permian Triassic mass extinction event of approximately 250 Ma ago occurred, known for the turnover of the terrestrial ecosystem and severe loss of marine invertebrate biodiversity (Schneebeli-Hermann *et al.*, 2013). Like the PETM, a negative CIE shift and rebound event was recorded in marine carbonate records (Brand *et al.*, 2016). Although the cause and magnitude of this CIE is still widely debated, it is thought that approximately 36,000 GtC was injected into the atmosphere, which led to severe global warming, ocean anoxia and extreme ocean acidification (Cui *et al.*, 2021; Joachimski *et al.*, 2020; Zhang *et*

al., 2018; Brand *et al*., 2012), causing the most-severe loss of biodiversity in Earth's known history (Cui *et al*., 2021; Burgess *et al*., 2014).

These CIE events are well documented by multi-proxy data (Gehler *et al*., 2016), and by reconstructing these extreme climatic events it has informed climatologists how the Earth operates during a warm interglacial, with atmospheric CO_2 greater than double the concentration of the present day (>840 ppm; Beerling & Royer, 2011; NOAA, 2022).

1.3   Global Climates in the Quaternary

The Quaternary period (ca. 2.28 Ma - Present) is a well-studied section of the geological past, owing to the archives and records being well preserved in ice cores, tree rings and sediments (Lowe & Walker, 2014). Boundary conditions of the Quaternary, including continental positioning, sea-ice cover and atmospheric CO_2, are similar to the environments present today (Ravelo *et al*., 2004; Stroynowski *et al*., 2015). By reconstructing how the Earth responded to previous climatic influences, more accurate inferences can be made regarding the effect of the current global warming episode.

The Quaternary period is characterised by cyclic glacial-interglacial (G-IG) periods, which involved the expansion and retraction of the Earth's icesheets. Table 1.1 adapted from Wenban-Smith *et al*. (2010), gives approximate ages and a summary of climate throughout each MIS in the Quaternary.

Table 1.1. Marine Isotope Stage Framework and associated epochs adapted from Wenban-Smith *et al.* (2010)

Epoch	Approximate Age (BP)	Marine Isotope Stage	Climate
Holocene	Present 10,000	1	Warm – full interglacial
Late Pleistocene	25,000	2	Mainly cold; coldest in MI Stage 2 (LGM). Short-lived periods of relative warmth ('Interstadials')
	50,000	3	
	70,000	4	
	110,000	5a-d	
	125,000	5e	Warm – full interglacial
Middle Pleistocene	190,000	6	Alternating periods of cold and warmth
	240,000	7	
	300,000	8	
	340,000	9	
	380,000	10	
	425,000	11	Warm – full interglacial
	480,000	12	Cold
	620,000	13-16	Cycles of cold and warmth
	780,000	17-19	
Early Pleistocene	1,800,000	20-64	Cycles of cold and warmth

Climatic research to date has focused on the lead up to, and out of, the last glacial maximum (LGM; ca. 20 kya). Lisiecki & Raymo (2005) produced one of the most widely used age models, termed the 'LR04 stack' (Figure 1.2) which denotes the mean of 57 globally distributed benthic $\delta^{18}O$ records, representing global ice volume and deep-water temperatures, spanning 0 – 5.3 Ma (Ahn *et al.*, 2017).
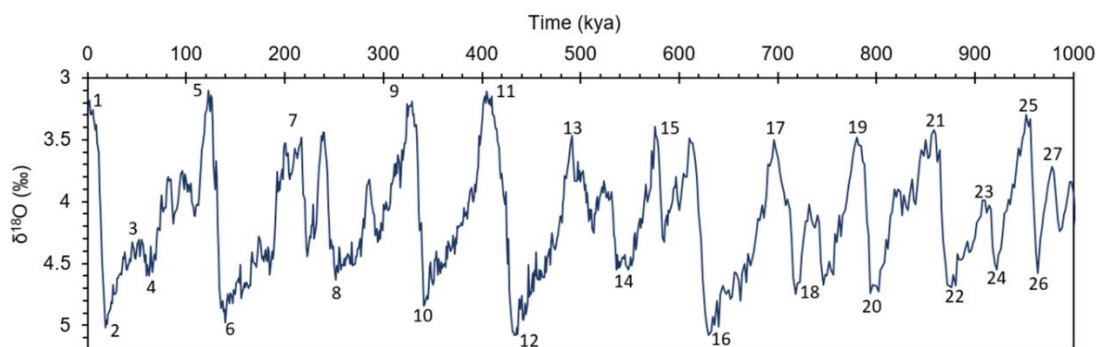
Figure 1.2. The LR04 benthic $\delta^{18}O$ stack from graphic correlation of 57 globally distributed benthic $\delta^{18}O$ records of foraminifera by Lisiecki & Raymo (2005). The marine isotope stages are identified.

Lisiecki and Raymo (2005; Figure 1.2) compiled benthic $\delta^{18}O$ data that show extreme differences in foraminiferal oxygen isotope ($\delta^{18}O$ ‰) values, which are identified as Marine Isotope Stages (MIS), or sometimes Oxygen Isotope Stages (OIS; Railsback *et al.*, 2015; Lisiecki & Raymo, 2005). The production of orbital-scale age models across the Quaternary period is essential in the understanding of climatic changes throughout G-IG cycles (Asahi *et al.*, 2016). Low $\delta^{18}O$ (‰) values represent warm periods, denoted by an odd MIS, whereas even numbers represent colder, glacial, times. This occurs due to evaporation and precipitation; lighter isotopes (^{16}O) evaporate from warm waters first, and the heavier isotopes (^{18}O) precipitate first. Warm, or interglacial, climates

therefore have greater proportions of ^{18}O in the ocean than during glacial events.

The Quaternary period is subdivided into two distinct epochs, the Pleistocene, which began about 2.6 Ma ago and ended upon introduction to the Holocene, 11.7 kya ago. The Pleistocene and Holocene epochs had an oscillating global climate, formed of stadials and interstadials, minor climate fluctuations that were punctuated with abrupt climatic changes known as Dansgaard-Oeschger (D-O) interstadial events (Lécuyer *et al.*, 2021; Cooper *et al.*, 2015). Some of the more abrupt climate events are well-defined in ice core records across both hemispheres and given in Table 1.2. The compilation of 104 high-resolution paleoclimate studies showed that both hemispheres had greater spatial heterogeneity than previously thought (Shakun & Carlson, 2010). The Younger Dryas (YD) of the Northern Hemisphere (NH) became cold and dry while the Southern Hemisphere became increasingly warm and wet (Shakun & Carlson, 2010). Similarly, the Antarctic Cold Reversal (ACR) was out of phase with Bølling/Allerød of the NH and led to the redistribution of heat, owing to changes in current including the weakening of the Atlantic Meridional Overturning Circulation (AMOC; Shakun & Carlson, 2010; Liu *et al.*, 2009).

Table 1.2. Abrupt deglaciation events spanning the late Pleistocene across both hemispheres.

Hemisphere	Event Name	Approximate Date (kya)
Northern	Oldest Dryas	18 – 14.7
	Bølling/Allerød (B/A)	14.7 – 12.9
	Younger Dryas (YD)	12.9 – 11.7
Southern	Antarctic Cold Reversal (ACR)	15 – 13

The ice age peaked at the LGM which occurred approximately 20 kya ago, in MIS 2, when ice sheets covered large portions of the Earth and global mean surface air temperatures were approximately 6.1 °C (6.5 to 5.7 °C, 95% CI) cooler than today (Tierney *et al.*, 2020). Following the deglaciation events listed in Table 1.2, the cooler temperatures of the Pleistocene were replaced by the relatively warm temperatures of the Holocene (MIS 1).

Marcott *et al.* (2013) reconstructed climate across the Holocene using 73 globally distributed records, finding that warming was not consistent across all latitudes. Extratropical Northern Hemisphere locations (30° – 90°N) contributed the greatest variance, with temperature decreases shown to be ca. 2 °C from 7000 – 100 cal BP, whereas the extratropical Southern Hemisphere (30° – 90°S) cooled ca. 0.4 °C between 11,000 – 7000 cal BP and remained rather constant until 2500 cal BP, where multicentennial variability was strong (Marcott *et al.*, 2013). Temperature increases were found to be much stronger at high latitudes, which can be attributed in part to the positive feedback mechanism of the land snow-cover albedo effect (Bernardi *et al.*, 2018; Li *et al.*, 2017; Marcott *et al.*, 2013; Kent *et al.*, 2003; Rohling *et al.*, 2012; Zachos *et al.*, 2006).

1.3.1 Arctic Responses to a Changing Climate

Snow cover has a substantial influence on the land surface albedo, but in the Arctic sea-ice albedo also forms a positive feedback mechanism that can have irreversible consequences on both a global and more regional scale. The present-day Arctic and sub-Arctic regions harbour a large quantity of organic carbon in both peatlands and the frozen soils (permafrost; Hugelius *et al.*, 2020; Swindles *et al.*, 2015). Permafrost is defined as any substrate remaining below

0 °C for more than two consecutive years (Douglas *et al.*, 2014). Increased atmospheric temperatures lead to increased microbial activity that could rapidly convert the 1700 Gt carbon predicted to be locked up in permafrost into GHGs, including CO_2 and CH_4, which return to the atmosphere over short timescales (Friedlingstein *et al.*, 2020; Castro *et al.*, 2010; Vonk and Gustafsson, 2013; Gruber *et al.*, 2004). Climate models suggest that permafrost regions could transition from atmospheric sinks of organic carbon to a net carbon source following a mass permafrost thaw (Gorham, 1991; Yu *et al.*, 2010). This feedback mechanism further accelerates climatic warming, however the rates and magnitudes, of the resultant temperature increase, remain relatively unknown (Schuur *et al.*, 2015; Voigt *et al.*, 2019).

A large-scale permafrost thaw, and subsequent GHG release, has only recently been modelled with confidence, with Canadell *et al.* (2021; Figure 1.3) stating future thaw would contribute to additional warming, but that a 'runaway warming' situation would not be triggered. One of the biggest challenges currently faced by climate researchers is the effect of a permafrost thaw, as this has not fully been incorporated into climate models, with the International Panel on Climate Change (IPCC; 2007) failing to consider future permafrost thaw.
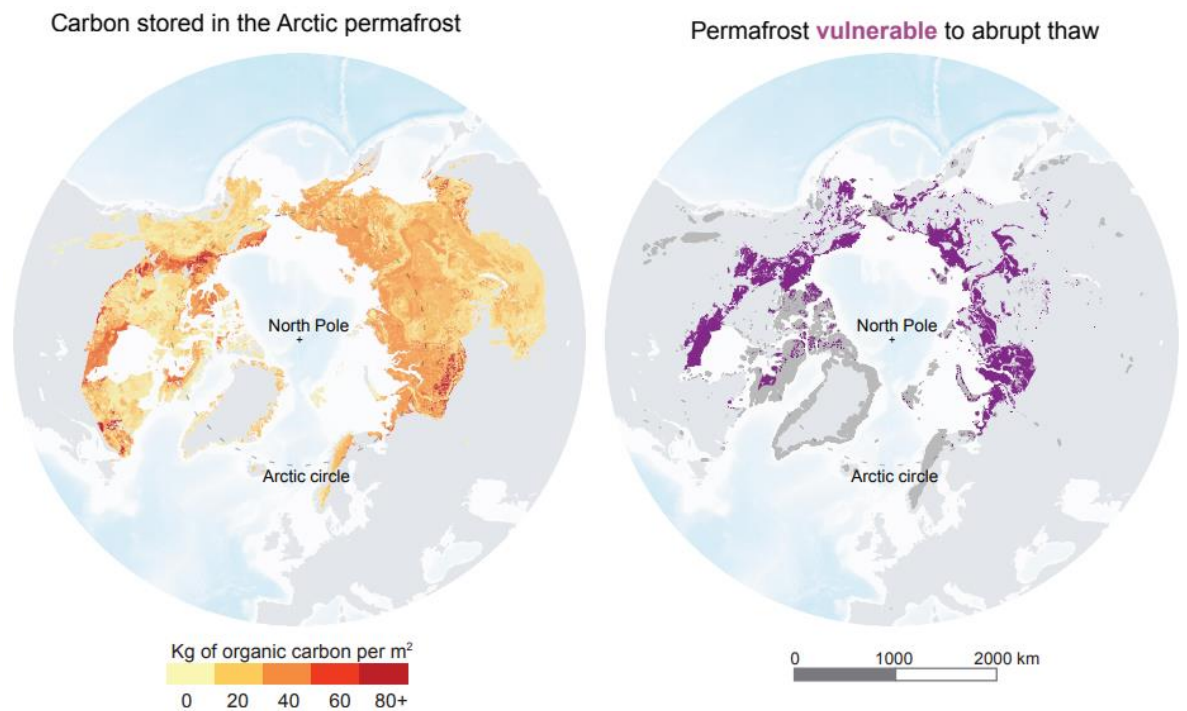
Figure 1.3. Quantity of carbon stored in Arctic permafrost, up to 3 m in depth (left) and the areas of permafrost most vulnerable to abrupt thaw (right). Figure taken from Canadell *et al.* (2021).

A thawing permafrost would not only have an adverse effect on global climate, but on a more localised scale it would have a critical effect on infrastructure, the use of natural resource and the sustainable development of communities in the Arctic (Gautier *et al.*, 2009; Hjort *et al.*, 2018; Larsen *et al.*, 2014; Melvin *et al.*, 2017). Abrupt permafrost thawing occurs in ice-rich peatlands, leading to ground collapse and thermokarst followed by the large release of CH_4 (Hugelius *et al.*, 2020). Hjort *et al.* (2018) predict that approximately three quarters of people living in the NH permafrost area could be affected by damaged infrastruture caused by permafrost thaw by 2050.

Therefore, research into Quaternary climates is increasingly important due to the concerns about future climatic changes and the impact human activity has upon them. The effect increasing temperatures will have on a global scale, or at a more localised level where infrastructure, land and sea ice are critical to Arctic

communities, including the indigenous populations is yet to be fully explored and understood.

The Arctic is the fastest changing region on the planet (Thomas *et al.*, 2022). The Arctic Ocean is characterised by large variability in sea ice extent over seasonal timescales, with paleoceanographic reconstructions also showing massive fluctuations across millennial timescales, from permanent ice-cover to nearly ice-free conditions. Accelerated sea-ice loss, increased permafrost thaw and large temperature warmings have already impacted marine, freshwater and terrestrial sociological-ecological systems in the northern high-latitudes. Continued environmental changes will affect the biological and biogeochemical processes that occur, leading to losses of biodiversity and increased invasions of species, adapted to the warmer waters of lower latitudes (Agustí *et al.*, 2010). Many Arctic coastal communities and facilities will be exposed to more extreme weather events and storms, increasing coastal erosion and the flooding of coastal wetlands (Corell, 2006). Thawing grounds will disrupt transportation, buildings and other infrastructure that local communities rely on. Indigenous peoples rely on hunting and gathering, not only for food and economic purposes, but as a basis for their cultural and social identities (Corell, 2006).

1.3.2 Bering Sea

The Bering Sea is the northernmost marginal sea of the Pacific Ocean, bordered on the north and west by Russia and on the east by Alaska, with the Aleutian Islands located to the south (Stabeno *et al.*, 1999). The continental shelves in the east create average water depths of around 200 m, whereas the deep-water basins in the west, including Bowers Ridge and the Aleutian Basin, have depths greater than 3500 m. The Bering Sea is characterised by the

extreme differences in water depth profiles caused by seasonal sea ice cycles and upwelling along the continental margin, producing a 'green belt' region high in nutrients and primary biological productivity.

The modern Bering Sea is connected to the Pacific Ocean by straits and passes (Figure 1.4). Surface water circulation within the basin forms an anti-clockwise cyclonic gyre, with the southerly Kamchatka Current feeding into the Pacific Ocean, and The Alaskan Stream flowing northward through the Aleutian Islands (Chen *et al*., 2014). Surface circulation maintains the salinity and temperature distributions across the Bering Sea; warm salty water enters the basin from the Northern Pacific, where colder freshwaters are exchanged (Johnson & Stabeno, 2017). The cold fresh waters also flow into the Arctic through the Bering Strait (Woodgate *et al*., 2012). Deep water mixing occurs mostly across the Aleutian Islands, with most of the water exchange occurring in the eastern Bering Sea at the Unimak Pass.
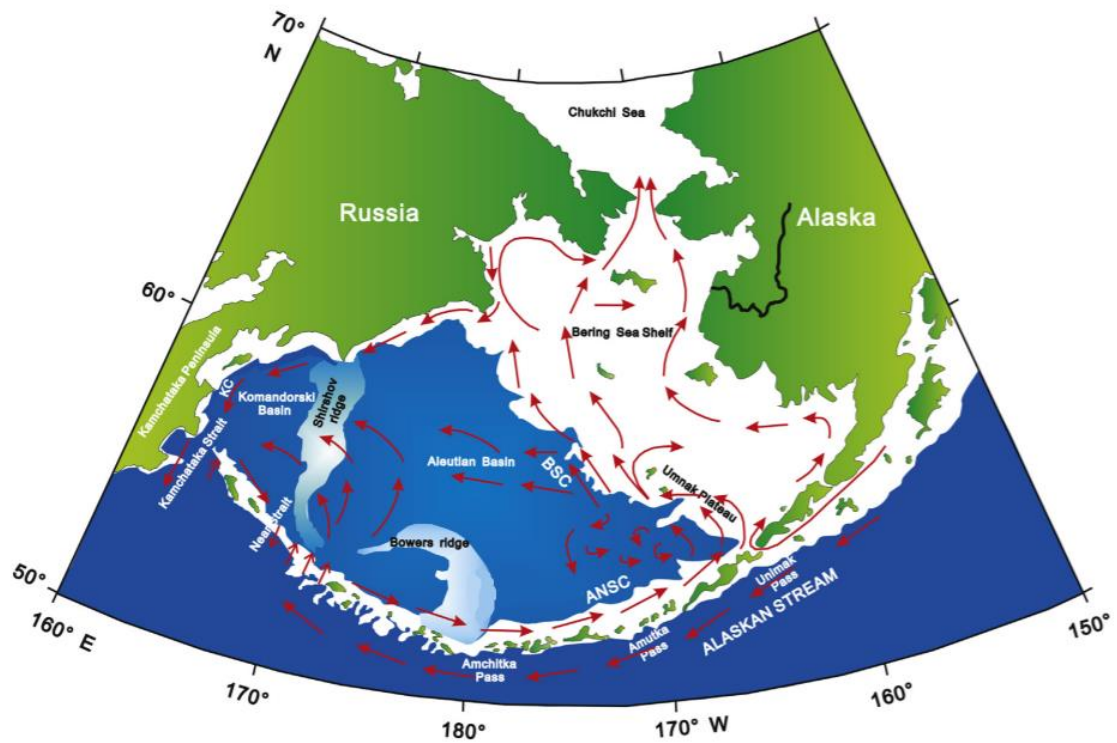
Figure 1.4. Topography and surface water circulation of the Bering Sea (from Stabeno *et al.*, 1999). The Alaskan Stream, Kamchatka Current, Bering Slope Current and the Aleutian North Slope Current are indicated (from Takahashi *et al.*, 2011). Figure adapted from Chen *et al.* (2014).

Acting as a gateway between the Pacific and Arctic Oceans, the Bering Sea and the Bering Strait have received significant attention for studies involved in the understanding of global climate changes of the present and past (Kender *et al.*, 2018; Takahashi *et al.*, 2002). Turbulent eddies extend to depths of approximately 300 m off the Bering Sea Shelf, forming part of the Bering Slope Current (BSC), causing upwelling of North Pacific Deep Water (NPDW), which contains some of the highest nutrient concentrations across the marine environment (Worne *et al.*, 2019; Stabeno *et al.*, 1999). Ecosystem dynamics within the Arctic rely on light and nutrients, including iron. Primary producers in both the sea ice and the underlying ocean require light for growth (Michel *et al.*, 1988; Castellani *et al.*, 2022), while warming events, and subsequent ice loss,

will affect the radiative balance of polar waters, affecting their thermal and light environments.

1.3.3 Bering Strait Closure

The region surrounding the Bering Sea differs significantly between the LGM and present day, by means of surface currents and sea ice extent (Detlef, 2018). The periodic opening and closing of the Bering Strait, due to the rising and lowering of sea level, through G-IG times, disrupts the Northern Pacific-Atlantic connection, which may have significant implications on global climate (De Boer & Nof, 2004; März *et al.*, 2013). The opening or closing of the Bering Strait affects water exchange between the Pacific and North Atlantic, via the Arctic Ocean, leading to global scale oceanic circulation changes involving the AMOC and the Thermohaline Circulation (Hu *et al.*, 2015). The AMOC carries warm and saline upper ocean waters northwards, where the heat is released to the atmosphere, and the resultant dense cold-water sinks and recirculates southwards as the North Atlantic Deep Water (NADW). The collapse of the AMOC can lead to the reversal of water movement through the Bering Strait, instead of transporting Pacific waters into the Atlantic, North Atlantic water is instead transported to the Northern Pacific, resulting in changes to circulation (Hu *et al.*, 2015).

1.4 Glycerol Dialkyl Glycerol Tetraethers (GDGTs) in Sediments as Proxies for Climate Change

Many microorganisms have a series of environmental conditions, such as temperature and oxygen concentrations, that must be within a narrow range to allow the species to thrive. In some cases, these organisms produce, or alter the ratio of, organic compounds to adapt to these specific conditions. Following deposition and degradation over numerous years, compounds have been identified and used as an indicator for one or more environmental parameter for the time of deposition, termed biological markers, or biomarkers (Hebting *et al.*, 2006; Rampen, 2009; Sinninghe Damsté & De Leeuw, 1990). The presence, ratio or concentration of biomarkers can therefore identify or indicate a climatic or environmental variable present at the time of deposition. GDGTs are one type of compound known to be molecular biomarkers, initially proposed by Schouten *et al.* (2002) as a proxy for sea surface temperatures (SSTs).

The analysis of intact core lipids, without the need for an ether cleavage to release the carbon chains, was made possible through the development of HPLC-MS (Hopmans *et al.*, 2000; Hopmans *et al.*, 2016). This allowed for the discovery of new GDGTs and the development of proxies relating to temperature including the TetraEther indeX of tetraethers consisting of 86 carbon atoms (TEX_{86}; Schouten *et al.*, 2002) and the qualitative measure of soil, or terrestrial, OM (%OMsoil) in marine sediments via the branched/isoprenoid tetraether (BIT) index (Hopmans *et al.*, 2004).

The development of the SST proxy TEX_{86} first detailed by Schouten *et al.* (2002) using marine sediments and advances in HPLC-MS methodology (Hopmans *et al.*, 2000) allowed Powers *et al.* (2004) to investigate GDGT

populations in lacustrine systems. They demonstrated that GDGTs were not limited to the marine environment, resulting in terrestrial and continental use of GDGTs as paleoclimate proxies.

1.4.1 Source and Structure of GDGTs

GDGTs are among the most abundant and ubiquitous lipids found on Earth (Schouten *et al.*, 2013) and derive from both archaea and bacteria. The structure of GDGTs synthesised in nature differ depending on their source, with bacteria producing lipids with levorotary configurations of *sn*-1,2-glycerol, whereas archaeal diethers have *sn*-2,3-glycerol stereochemistry (Pancost *et al.*, 2001). Although the pathways in which they are produced and the enzymes involved are still under debate (Zeng *et al.*, 2022).

Archaea are one of the three main domains of life, along with bacteria and eukarya (Woese & Fox, 1977). Prior to their recognition as a novel phylogenetic group, it was believed that archaea belonged to one of three groups, thermophiles, halophiles, or methanogens relating to the extreme environment in which they were found (Brock, 1978; Woese, 1987). An additional subgroup of archaea was later identified, from non-thermophilic conditions, termed Crenarchaeota, found in marine and lacustrine environments (Hopmans *et al.*, 2000; Schouten *et al.*, 2002).

The subgroups of Archaea have since been reclassified, with taxonomists dividing them between five phyla: Crenarchaeota, Euryarchaeota, Korarchaeota, Nanoarchaeota and Thaumarchaeota (Spang *et al.*, 2013). These have been found to have phylogenetic differences in membrane lipids when compared to bacteria or eukaryotes. Bacterial membranes are generally formed from straight-chain fatty acids ester-bound to glycerol arranged into a

bilayer (Huguet *et al.*, 2006a), while Archaea synthesise bilayer membranes (archaeol) that consist of isoprenoid alkyl chains ether-bound to glycerol, or are monolayer membranes formed from GDGTs (Schouten *et al.*, 2013; Zeng *et al.*, 2022).

The ubiquitous Crenarchaeota phylum synthesise isoprenoid GDGTs (isoGDGTs; Figure 1.5) like those of their extremophilic ancestors. Thaumarchaeota also synthesise the structurally divergent crenarchaeol and its regioisomer (a structurally similar molecule, but a functional group has moved position), thought to be an adaptation to cold temperature environments and introduces seasonal variability (Schouten *et al.*, 2000; Sinninghe Damsté *et al.*, 2002; Huguet *et al.*, 2006a; van Bree *et al.*, 2020). The presence of crenarchaeol was proposed to be taxonomically significant and unique to the non-thermophilic archaea (Sinninghe Damsté *et al.*, 2002), however this has since been disproven following the discovery of crenarchaeol in hot springs (Schouten *et al.*, 2007) as well as from cultivated Thaumarchaeota, where it was found to be one of the more dominant GDGTs (de la Torre *et al.*, 2008; Pitcher *et al.*, 2010). Crenarchaeol presence is now attributed to ammonia oxidising Thaumarchaeota (de la Torre *et al.* 2008; Pitcher *et al.*, 2010; Yang *et al.*, 2021).
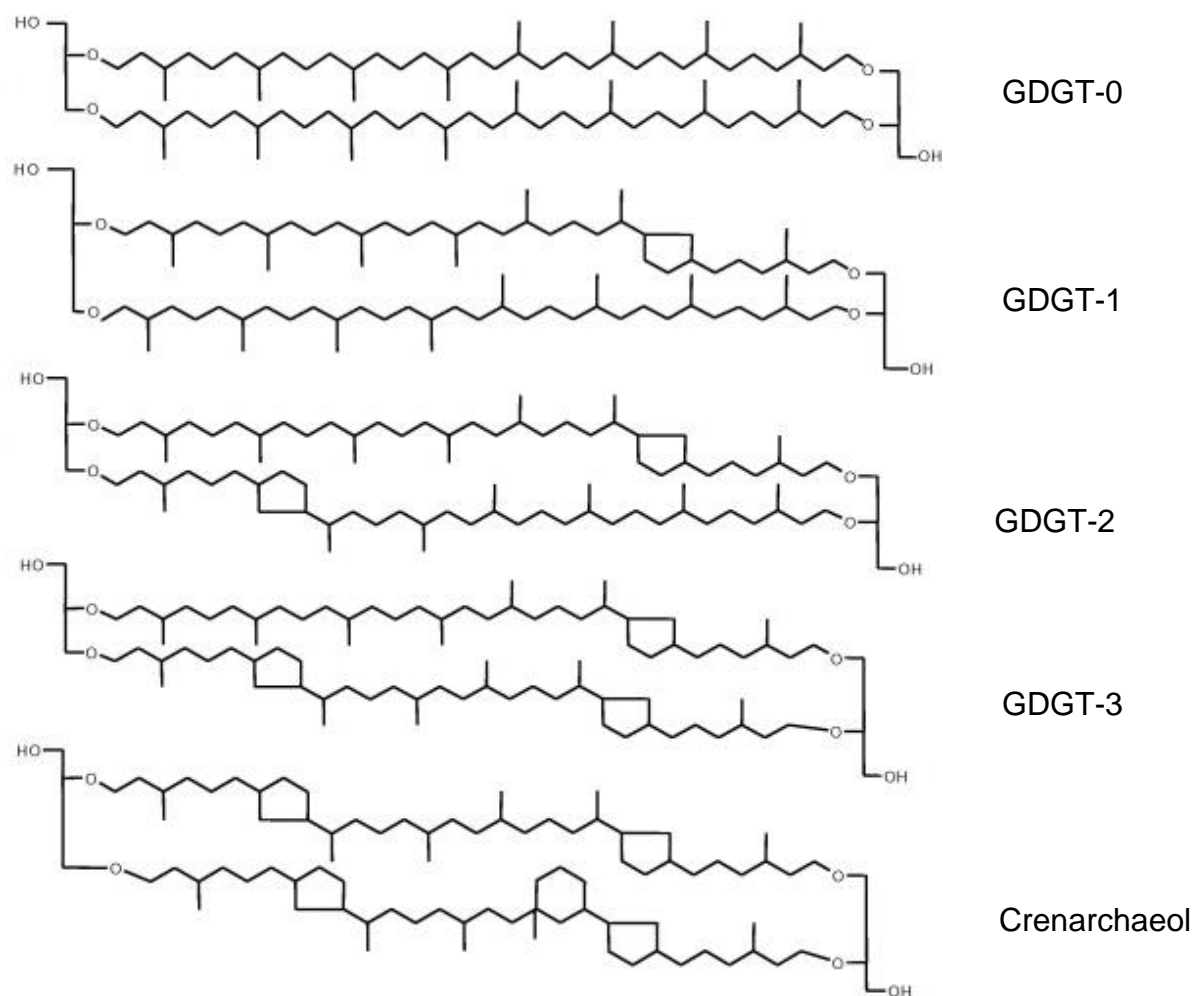
Figure 1.5. Isoprenoid glycerol dialkyl glycerol tetraether (isoGDGT) structures GDGT-0 to GDGT-3, and crenarchaeol.

Whilst isoGDGTs occur ubiquitously in marine water columns (Blaga *et al*. 2009; Guo *et al*., 2021), sediments (Schouten *et al*., 2013; Gies *et al*., 2021) and lakes (Loomis *et al*., 2011; Shanahan *et al*., 2013), branched GDGTs (brGDGTs) are specific to soils and peatlands (Sinninghe Damsté *et al*., 2002, Schouten *et al*., 2013; Naafs *et al*., 2018). However, brGDGTs are not limited to terrestrial environments, and often found in coastal marine sediments as they are also produced in the water column (van Bree *et al*., 2020; Peterse *et al*., 2009). Fluvial transport of terrestrial soil OM also contributes to marine brGDGT abundance, is some shelf systems (Hopmans *et al*., 2004; Schouten *et al*., 2013; Sparkes *et al*,, 2015). Weijers *et al*. (2006a) showed that the membrane

spanning brGDGTs are exclusively of a bacterial origin. The stereochemistry of the glycerol moiety was found to be the inverse to those within archaeal isoGDGTs (Weijers *et al.*, 2006a), with this stereochemistry being fundamental in the evolutionary differences between the Bacteria and Archaea kingdoms (Koga *et al.* 1998; Schouten *et al.*, 2013).

1.4.2 GDGTs as Proxies in the Marine Environment

Marine sediments are one of the most expansive and critical carbon stores on the planet, where it is estimated 2322 Pg C is stored in the top 1 m of the benthos, with the sediments and oceans playing a vital role in global climate regulation (Atwood *et al.*, 2020; Barber *et al.*, 2017). Useful geochemical proxies and biomarkers can be found within these sediments. A number of SST proxies were already established and used in organic geochemical investigations before the conception and development of TEX_{86}, including the Mg/Ca and $\delta^{18}O$ ratios of planktonic foraminifera or the alkenone unsaturation indices (Unsaturated Ketones with 37 carbon atoms; U^K_{37} and $U^{K'}_{37}$; Equations 1.1 and 1.2) developed by Brassell *et al.* (1986) and Prahl & Wakeham (1987), respectively. The alkenone unsaturation index ratio produced is commonly converted to SST using the calibration of Müller *et al.* (1998; Equation 1.3), where T = SST in °C, though other equations have been used (Conte *et al.*, 2006; Prahl *et al.*, 1988; Sonzogni *et al.*, 1997).

$$U^K_{37} = \frac{C_{37:2} - C_{37:4}}{C_{37:2} + C_{37:3} + C_{37:4}}$$ **(Eq. 1.1)**

$$U^{K'}_{37} = \frac{C_{37:2}}{C_{37:2} + C_{37:3}}$$ **(Eq. 1.2)**

$$U^{K'}_{37} = 0.033T + 0.044 \quad (r^2 = 0.958, n = \text{not defined})$$ **(Eq. 1.3)**

Alkenones in sediments were found to be structurally identical to those biosynthesised by a limited group of phytoplankton, haptophyte algae, a dominant primary producer in the modern oceans (Volkman *et al.*, 1980). Unlike isoGDGTs in archaeal membranes, the degree of unsaturation increases with decreased temperatures. Alkenones have been used as a proxy for palaeoceanographic records spanning millions of years (Wang *et al.*, 2021; Zhang *et al.*, 2013), yet the low relative concentrations of $C_{37:2}$ and $C_{37:3}$ at high latitudes, and the significant bias towards warmer temperatures (Wang *et al.*, 2021) leads to errors in SST reconstructions. Similarly, the anomalously high relative distribution of the tetra-unsaturated C_{37} methyl alkenone (%$C_{37:4}$) at high latitudes makes any SST produced unreliable, alternative SST proxies are therefore applied in those latitudes (Rosell-Melé, 1998; Wang *et al.*, 2021). The degree of uncertainty relating to existing SST models led Schouten *et al.* (2002) to investigate the known link between isoprenoid lipid membrane compositions within plankton to the growth temperatures.

1.4.3 Introduction of the TEX$_{86}$ Proxy

Schouten *et al.* (2002) originally analysed 40 surface sediments across 15 locations worldwide, from a variety of environments across upwelling and non-upwelling areas. The annual temperatures ranged between 2 and 27 °C with water depths extending between 10 and 30 m in the Wadden Sea, to greater than 2000 m of the Black Sea. It was identified that the composition of isoGDGTs in colder climates was different to those in warmer ones; in colder climates such as Halley Bay, Antarctica, GDGT-0 (Figure 1.5) dominated followed by crenarchaeol, whereas distributions from warmer areas, such as the Arabian Sea, were dominated by crenarchaeol and had relatively higher distributions of GDGTs 1-3. A regioisomer for crenarchaeol was also identified,

termed herein as *cren'*, though the structure is still debated. This aligned with the belief that the average number of cyclopentane rings increased with the mean local temperature, while simultaneously explaining why crenarchaeota can thrive across broad temperature ranges, i.e. between 0 and 30 °C (Schouten *et al.*, 2002).

The relationship between temperature and number of cyclopentane rings was obtained using the TEX_{86} index (Equations 1.4 and 1.5), which Schouten *et al.* (2002) defined as:

$$TEX_{86} = \frac{[GDGT\text{-}2]+[GDGT\text{-}3]+[cren']}{[GDGT\text{-}1]+[GDGT\text{-}2]+[GDGT\text{-}3]+[cren']} \qquad \textbf{(Eq. 1.4)}$$

Greatest linearity was discovered with mean annual SST ($r^2 = 0.92$, n = 44) as opposed to mean temperature at 100 m depth ($r^2 = 0.86$), correlating the TEX_{86} ratio with temperature was therefore defined as:

$$TEX_{86} = 0.015T + 0.28 \quad (r^2 = 0.92, n = 44) \qquad \textbf{(Eq. 1.5)}$$

Where T = annual mean SST (°C).

Schouten *et al.* (2002) rationalised the increased linearity through consideration of lipid source, where GDGT-0 is produced, not only by the targeted planktonic non-thermophilic crenarchaeota, but also in methanogenic archaea which skewed the signal at deeper depths (Schouten *et al.*, 2000; 2002). Methanogens found in anoxic sediments or micro niches, including the water column or fish guts (DeLong, 2021; Reeburgh, 2007), do not synthesise the crenarchaeol isomer but do increase the total GDGT numbers in marine sediments (Schouten *et al.*, 2002).

Temperature was not the only environmental factor that was different across the core-top sampling locations used to develop the TEX_{86} index. Salinity between

sites also varied. Other works have looked into GDGT distributions with salinity (Dawson *et al.*, 2012; Elling *et al.*, 2015; Wied, 2017), or oxygen (Qin *et al.*, 2015), producing mixed outputs. Dawson *et al.* (2012) and Wied (2017) both found changes in membrane lipid composition with salinity differences, where Dawson *et al.* (2012) described a relative increase in non-cyclic structures. However, Elling *et al.* (2015) found no systematic influence of salinity on lipid composition. Therefore, more research is likely needed to fully understand the effect environmental conditions other than temperature may have on the TEX_{86} index.

The concentrations of GDGT-1, GDGT-2 and GDGT-3 were found to be decreased in low temperature regions compared to GDGT-0 and crenarchaeol (Schouten *et al.*, 2002), leading Kim *et al.* (2008) to conduct a study using a wider number of core-top sediments. The TEX_{86} index was once again found to be strongly correlated with annual mean temperature. For SSTs between 5 and 30 °C, TEX_{86} was linearly correlated using Equation 1.6.

$$SST = 56.2 \times TEX_{86} - 10.8 \quad (r^2 = 0.935, n = 223) \qquad \textbf{(Eq. 1.6)}$$

But the linearity was found to not be as strong at temperatures < 5 °C, leading Liu *et al.* (2009) to propose a non-linear calibration for TEX_{86}. Kim *et al.* (2010) expanded the core-top study previously conducted, focusing on subpolar and polar waters. As there was no evidence that cren' was produced within membranes of marine crenarchaeota as an adaptation to cooler temperatures, it was removed from the TEX_{86} ratio due to poor correlation. The reverse was true for subtropical and tropical waters, leading to the production of two distinct TEX_{86} indices (Kim *et al.*, 2015). One for low temperature regions, between -3 and 30 °C, termed TEX_{86}^L, which does not include cren', (Equations 1.7 and

1.8), and a separate equation correlated with greenhouse periods, with temperatures >15 °C, TEX_{86}^H (Equations 1.9 and 1.10; Kim *et al.*, 2010; Kim *et al.*, 2015).

$$TEX_{86}^L = \log \frac{([GDGT\text{-}2])}{([GDGT\text{-}1])+([GDGT\text{-}2])+([GDGT\text{-}3])}$$ **(Eq. 1.7)**

$$SST = 67.5 \times TEX_{86}^L + 46.9 \quad (r^2 = 0.86,\ n = 393)$$ **(Eq. 1.8)**

$$TEX_{86}^H = \log \frac{([GDGT\text{-}2]) + ([GDGT\text{-}3]) + ([cren'])}{([GDGT\text{-}1])+([GDGT\text{-}2])+([GDGT\text{-}3])+ ([cren'])}$$ **(Eq. 1.9)**

$$SST = 56.3 \times TEX_{86}^H + 30.2 \quad (r^2 = 0.94,\ n = 45)$$ **(Eq. 1.10)**

TEX_{86} is calibrated to represent the mean annual SST, yet within high-latitude seas the production is said to be highly seasonal (Park *et al.*, 2019). Production peaks during the spring-summer months, where seasonal temperatures increase and sunlight hours are longer, increasing organic matter contribution within the sediment. SST reconstruction from the literature show that TEX_{86} calibrations are not improved reconstructing seasonal temperatures over annual ones (Kim *et al.*, 2010; Tierney and Tingley, 2014). Modern observations indicate homogenisation of the seasonal cycles occur within deep marine waters, meaning seasonality has a limited effect on sedimentary TEX_{86} values (Richey and Tierney, 2016; Sluijs *et al.* 2020).

Studies can conduct a multi-proxy approach, wherein multiple proxies for the same environmental parameter are assessed. To recreate SST, the TEX_{86} and $U_{37}^{K'}$ can often be simultaneously assessed (Morcillo-Montalbá *et al.*, 2021; Lawrence *et al.*, 2020; Huguet *et al.*, 2006b; Turich *et al.*, 2013) which generally produce results in which TEX_{86} temperatures fall below those produced using the $U_{37}^{K'}$ (McClymont *et al.*, 2012). Kim *et al.* (2008) and Li *et al.* (2013) attribute

this to $U^{K'}_{37}$ representing the sea surface, while TEX$_{86}$ reconstructs sub-surface temperatures from below the mixed layer, or at greater depths below the thermocline (>50m; McClymont *et al.*, 2012).

1.4.4 GDGTs in the Terrestrial Environment

Non-isoprenoid GDGTs have also been identified and used as a proxy for terrestrial temperatures, initially found by Sinninghe Damsté *et al.* (2000) in peat and characterised by Schouten *et al.* (2000). Instead of being composed of isoprenoids, the GDGTs contained branched alkyl chains which are believed to be from a bacterial origin. The carbon isotope values indicated a heterotrophic bacterial source (Pancost *et al.* 2000; Weijers *et al.* 2006a; Oppermann *et al.* 2010).

Hopmans *et al.* (2004) found that brGDGTs were present in large quantities in peat samples. The absence of GDGT-0 led these workers to hypothesise that brGDGTs originated from a different source to that of isoGDGTs which corroborates the findings of Pancost *et al.* (2000) and later Weijers *et al.* (2006a) and Oppermann *et al.* (2010) that the source was heterotrophic bacteria. The presence of brGDGTs in soils, peats, marine and lake settings led Hopmans *et al.* (2004) to suggest the compounds could be used as a tracer for the transport of organic matter (OM) from peat and soils, with increased abundances found at near-shore locations.

Attributing transport of terrestrial OM as the source of brGDGTs in water-based settings, and simultaneously observing that crenarchaeol dominates water column samples while being present in only minor amounts in peats, led Hopmans *et al.* (2004) to propose the Branched Isoprenoid Tetraether (BIT) index as a proxy for evaluating terrestrial OM contribution to oceanic settings.

The relative abundance of brGDGTs, representing terrestrial OM, and crenarchaeol, representing aquatic OM, gave rise to the BIT index, (Equation 1.11; Hopmans et al., 2004), constituents represent structures, as shown in Figure 1.6.

$$BIT = \frac{(Ia+IIa+IIIa)}{(Ia+IIa+IIIa+cren)}$$ **(Eq. 1.11)**

1.4.4.1 Branched GDGTs as a Proxy for pH and Temperature

Weijers et al. (2007a) analysed the environmental conditions that affected bacterial tetraether membrane lipid distributions, using principal component analysis, finding that structural differences of the brGDGTs correlated with pH and temperature.

A total of 134 soil samples from across 90 global locations were assessed for brGDGT membrane lipid composition (Weijers et al., 2007a). The chromatograms produced from analysis highlighted differences in distribution of the three most abundant brGDGT structures, brGDGT-Ia (Ia), brGDGT-IIa (IIa) and brGDGT-IIIa (IIIa), structurally identified by differences in structure, with 0,1 or 2 additions of methyl chains on C-5 and C-5' carbon chains, respectively (Weijers et al. 2007a; Peterse et al., 2012; Figure 1.6). The brGDGTs containing 1 or 2 cyclopentyl moieties (Ib – IIIb and Ic – IIIc; Figure 1.6) were found to be less abundant, with IIIb, IIc and IIIc not always above the detection limit.
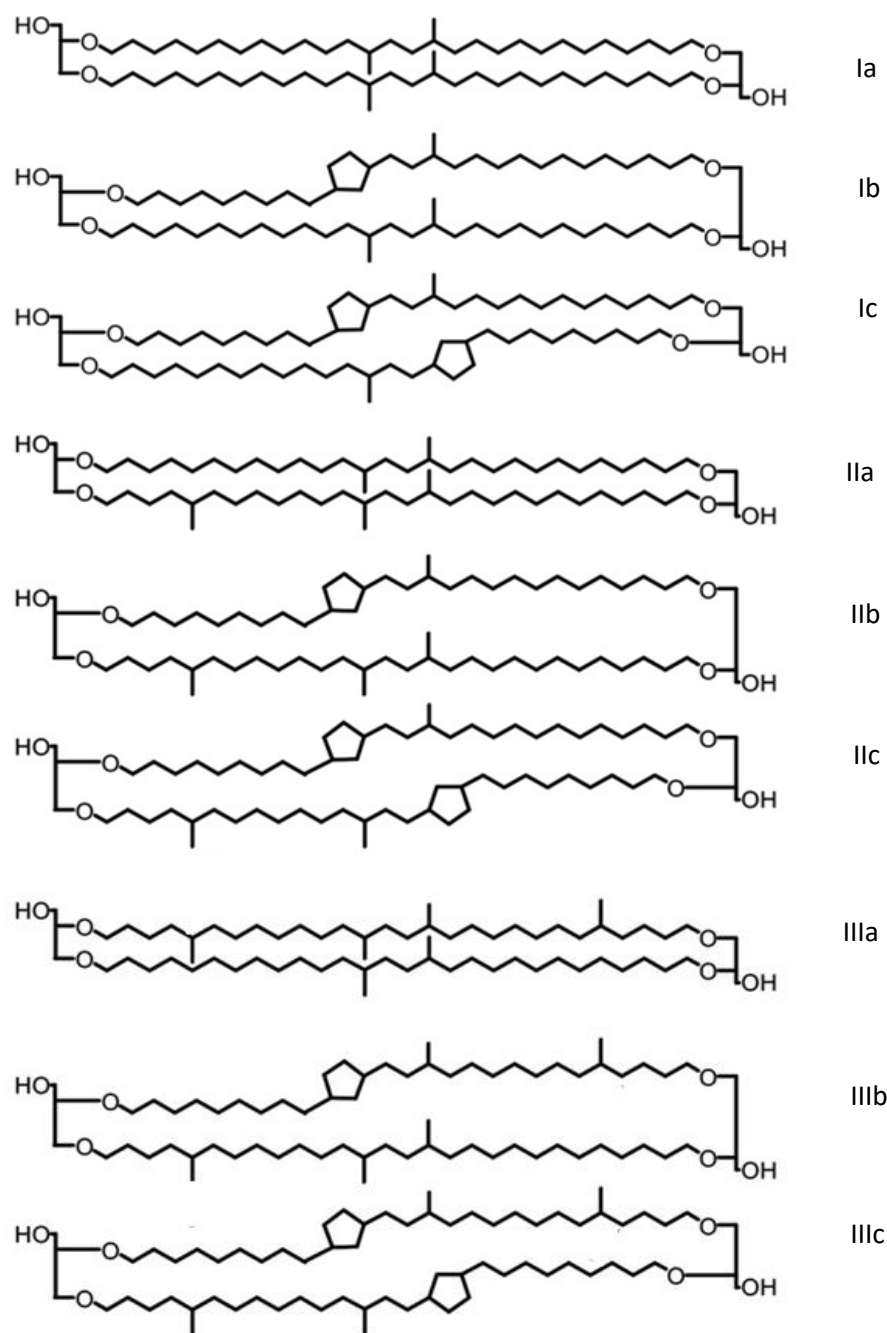
Figure 1.6. The 5-methyl brGDGT structures.

In general, Weijers *et al.* (2007a) found higher concentrations of brGDGTs in soils with a lower pH (<6). Two ratios were defined using PCA; the first, the methylation index of branched tetraethers (MBT), which represents the degree

of methylation at the C-5 and C-5' positions (Weijers *et al.* 2007a; Equation 1.12).

$$MBT = \frac{[Ia + Ib + Ic]}{[Ia+Ib+Ic]+[IIa+IIb+IIc]+[IIIa+IIIb+IIIc]}$$ **(Eq. 1.12)**

Where a high MBT value represents a low degree of methylation, and a low value is a high degree of methylation at C-5 and C-5'.

A cyclisation ratio, relative to the amount of cyclopentyl moieties in brGDGTs, was similarly defined (Weijers *et al.*, 2007a; Equation 1.13), wherein higher values indicate high abundances of cyclopentyl moieties. Low abundances of IIIb, IIc and IIIc excluded the isomers from the ratio.

$$Cyclisation\ ratio = \frac{[Ib]+[IIb]}{[Ia]+[IIa]}$$ **(Eq. 1.13)**

Plotting the cyclisation ratio against pH values of soils produced an exponential correlation ($r^2 = 0.70$). In Crenarchaeota, isoGDGT membrane lipids increase the number of cyclopentyl moieties in increased temperature, yet no such relationship was found by Weijers *et al.* (2007a). Instead the MBT ratio, Eq. 1.12, had a stronger correlation with mean annual temperature (MAT; $r^2 = 0.62$), with higher degrees of methylation found in lower temperature soils. The annual MAT and soil pH together, when plotted in a three-dimensional scatter graph with the MBT index, produces a strong correlation ($r^2 = 0.82$; Eq. 1.14).

$$MBT = 0.867 - 0.096 \times pH + 0.021 \times MAT \quad (r^2 = 0.82, n = 134)$$ **(Eq. 1.14)**

Microorganisms adapt the composition of their cell membranes depending on growth temperature. Archaea change the number of cyclopentyl moieties in their carbon chain, and bacteria change the chain length, and degree of saturation or branching of the fatty acid alkyl chains. Weijers *et al.* (2007a)

found brGDGT distributions with additional methyl branches, II and III isomers, to be dominant in Arctic sediments, suggesting that additional methyl groups, result in a loose packing structure, an adaptation to lower temperature environments.

Combining the correlation between cyclisation with pH (Equation 1.13) and the correlation between MBT, pH and MAT (Eq. 1.14), led Weijers *et al.* (2007a) to produce the cyclisation ratio of branched tetraethers (CBT; Equation 1.15).

$$CBT = -\log \left(\frac{([brGDGT\ Ib])+([brGDGT\text{-}IIb])}{([brGDGT\ Ia])+([brGDGT\ IIa])} \right) \qquad \textbf{(Eq. 1.15)}$$

Plotting CBT with pH of the soil, produced the linear correlation in Equation 1.16:

$$CBT = 3.33 - 0.38 \times pH \ (r^2 = 0.70,\ n = 134) \qquad \textbf{(Eq. 1.16)}$$

Soil pH and annual MAT can be reconstructed using lipid distributions alone by the combination of Equations 1.14 and 1.16, which produces Equation 1.17 (Weijers *et al.* 2007a):

$$MBT = 0.122 + 0.187 \times CBT + 0.020 \times MAT \quad (n = 114;\ r^2 = 0.77) \ \textbf{(Eq. 1.17)}$$

Following this brGDGT lipids have been shown to be reliable proxies for temperature in peats and surface soils (De Jonge *et al.*, 2014, Naafs *et al.*, 2017a; Dearing Crampton-Flood *et al.*, 2020; Peaple *et al.*, 2022), due to the methylation of the membrane lipids adjusting in different temperatures (Naafs *et al.*, 2021; Peaple *et al.*, 2022). Expanding the original core-top investigation by Weijers *et al.* (2007a), Peterse *et al.* (2012) also found that IIIb and IIIc were often absent from soils and represented <1% of the total abundance of brGDGTs when present. The MBT index was adjusted to not include these isomers (Equation 1.18; Table 1.3). De Jonge *et al.* (2013) identified further

brGDGT structures, 6-methyl brGDGTs, Figure 1.7, expanding the proxies able to be used for peat and soils alongside the development of chromatographic separation techniques (Hopmans *et al.*, 2016). De Jonge *et al.* (2014) successfully separated and quantified 6-methyl isomer brGDGTs, which previously co-eluted with their 5-methyl counterparts, these structures are denoted as IIa', IIb', IIc', IIIa', IIIb' and IIIc' and shown in Figure 1.7. Previous indices produced by Weijers *et al.* (2007a) include both 5-methyl and 6-methyl species, as at the time of creation it was assumed that the chromatographic peaks consisted of only one isomer. Table 1.3 shows the indices commonly used following brGDGT analysis today.

Table 1.3. Formulae using and brGDGT ratios for fractional abundances, adapted from Dugerdil *et al.* (2020).

Index / Equation No.	Formula	Proxy Purpose	Reference(s)
BIT (Eq. 1.11) [†]	$= \dfrac{Ia+IIa+IIa'+IIIa+IIIa'}{Ia+IIa+IIa'+IIIa+IIIa'+crenarchaeol}$	OM	Hopmans *et al.* (2004) De Jonge *et al.* (2015)
MBT (Eq. 1.12)	$= \dfrac{Ia+Ib+Ic}{\sum brGDGTs}$	Temperature, Precipitation, pH	Weijers *et al.* (2007a) Huguet *et al.* (2013)
MBT' (Eq. 1.18)	$= \dfrac{Ia+Ib+Ic}{Ia+Ib+Ic+IIa+IIa'+IIb+IIb'+IIc+IIc'+IIIa+IIIa'}$	Temperature, Precipitation	Peterse *et al.* (2012)
MBT'5$_{Me}$ (Eq. 1.19)	$= \dfrac{Ia+Ib+Ic}{Ia+Ib+Ic+IIa+IIb+IIc+IIIa}$	Temperature, Precipitation	De Jonge *et al.* (2014)
CBT (Eq. 1.15) [†]	$= -\log\left(\dfrac{Ib+IIb+IIb'}{Ia+IIa+IIa'}\right)$	pH	Weijers *et al.* (2007a)
CBT' (Eq. 1.20)	$= \log\left(\dfrac{Ic+IIa'+IIb'+IIc'+IIIa'+IIIb'+IIIc'}{Ia+IIa+IIIa}\right)$	pH	De Jonge *et al.* (2014)

† - Equation is the same as in text, but with 5-methyl and 6-methyl isomers explicitly stated.
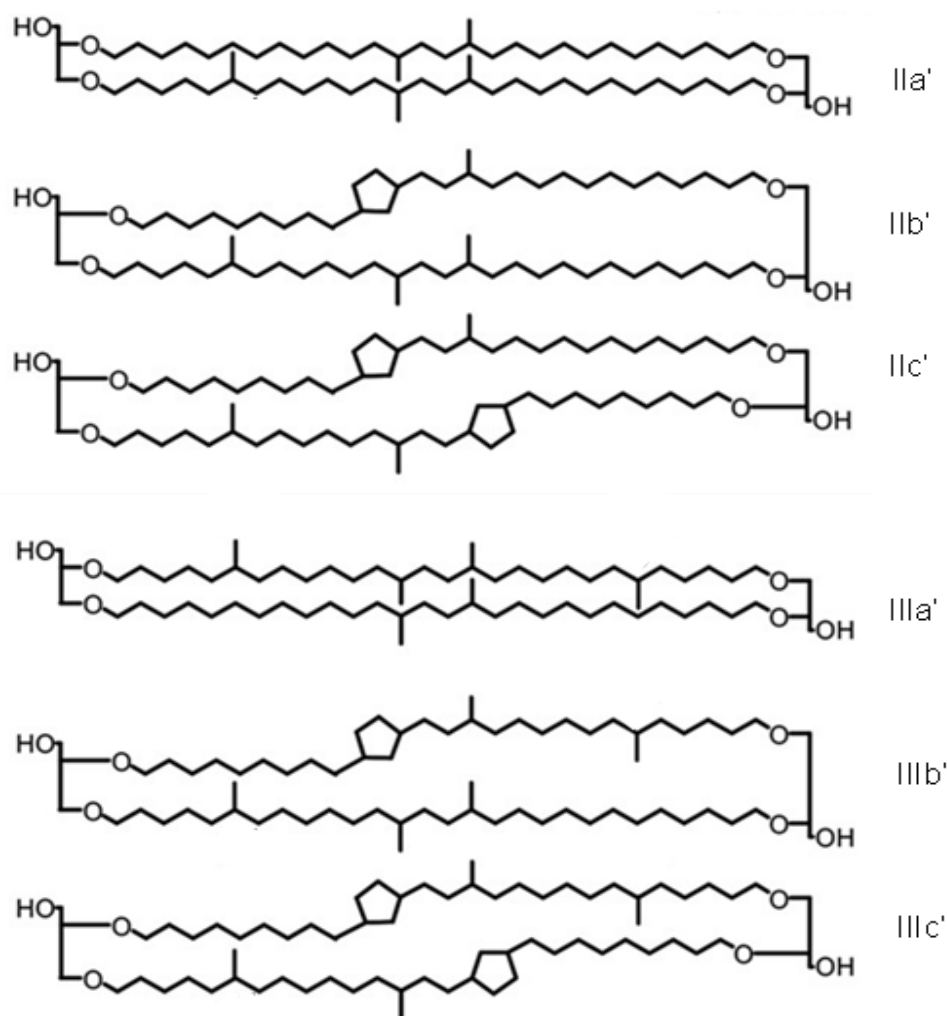
Figure 1.7. The 6-methyl brGDGT structures.

1.4.5 GDGT origin indicators

The ratio of isoGDGTs, brGDGTs and crenarchaeol compounds have previously been plotted on a ternary diagram (Schouten *et al.*, 2013; Figure 1.8.), and generally can be used to distinguish the environment in which they derived. Ternary plots outline the differences in GDGT distributions across different environments, with marine environments having high crenarchaeol and GDGT-0 concentrations and relatively low brGDGTs abundances. Soils, in contrast, contain a high abundance of brGDGTs with small contributions of GDGT-0 and crenarchaeol. Coastal marine and lacustrine environments show great variability, with all three components varying in abundance due to the

32

balance between the aquatic production of archaeal GDGTs, from Thaumarchaeota and methanogenic Euryarchaeota, and the terrestrial-derived contribution in soils, sediments or the water column.
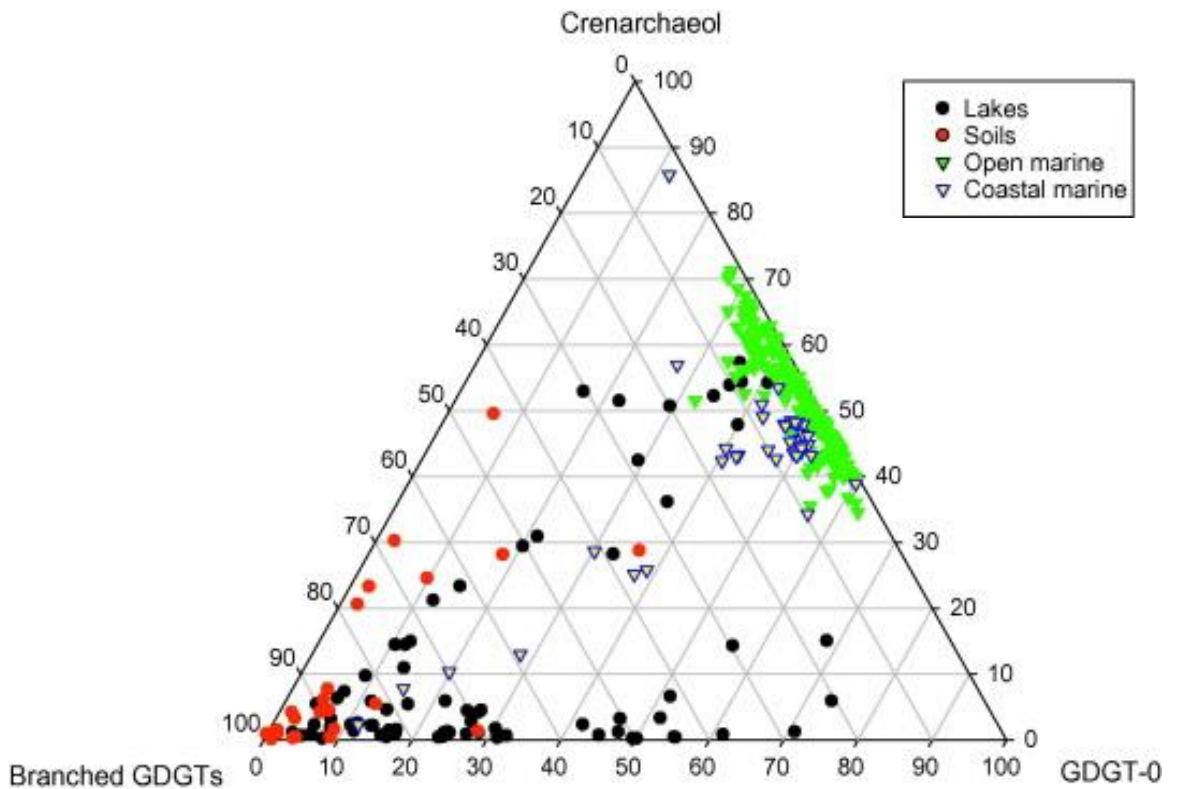
Figure 1.8. Ternary diagram from Schouten *et al.* (2013) revealing distribution of GDGT-0, crenarchaeol and the sum of branched GDGTs from modern environments using data from Blaga *et al.* (2009), Kim *et al.* (2010), Herfort *et al.* (2007), Hopmans *et al.* (2004) and Weijers *et al.* (2006b).

The relative abundances of brGDGTs, GDGT-0 and crenarchaeol indicate a broad environment, but utilising the relative abundances of each of the isoGDGT molecules can evidence their origin, with methanogenic and methanotrophic Euyarchaeota contribution determined through calculation of the methane index (MI; Equation 1.21; Sluijs *et al.*, 2020; Pancost *et al.*, 2001; Zhang *et al.*, 2011).

$$MI = \frac{[GDGT\text{-}1]+[GDGT\text{-}2]+[GDGT\text{-}3]}{[GDGT\text{-}1]+[GDGT\text{-}2]+[GDGT\text{-}3]+[cren]+[cren']}$$ **(Eq. 1.21)**

A significant contribution of anaerobic methanotrophy is concluded when MI values are greater than 0.5, with these values also giving rise to unreliable TEX_{86} values, and this inaccurate SSTs. (Sluijs *et al.*, 2020). Therefore, values should be calculated to assess the validity of TEX_{86}-derived SSTs.

Other indicators of methanogenic archaea include the GDGT-0/crenarchaeol ratio (Equation 1.22) where Blaga *et al.* (2009) describe significant contributions producing values greater than 2.

$$\text{GDGT-0/Cren} = \frac{\text{[GDGT-0]}}{\text{[crenarchaeol]}}$$
(Eq. 1.22)

These high values are rare within open marine environments (Inglis *et al.*, 2015; Zhang *et al.*, 2016). Sinninghe Damsté *et al.* (2012) proposed an additional indicator, %GDGT-0 (Equation 1.23) for methanogenic archaea contributions, with values greater than 67% indicating high methanogenic archaeal origin. All three methanogenic contribution indicators can be strongly influenced differences in crenarchaeol abundance.

$$\text{\%GDGT-0} = \frac{\text{[GDGT-0]}}{\text{[GDGT-0]} + \text{[crenarchaeol]}} \times 100$$
(Eq. 1.23)

The main source of isoGDGTs within the marine environment are from the ammonium oxidising Thaumarchaeota (Besseling *et al.*, 2020), which occur within the water column (Pitcher *et al.*, 2011). Deeper contributions of isoGDGTs have also been inferred from ^{14}C analysis (Shah *et al.*, 2008; Sluijs *et al.*, 2020) in the thermocline and from deep-dwelling archaea (Taylor *et al.*, 2013). The deep contributions are tracked using a GDGT-2 / GDGT-3 ratio (Equation 1.24; Sluijs *et al.*, 2020), with values greater than 5 indicating large contributions from deep water archaea.

$$\text{GDGT-2/GDGT-3 ratio} = \frac{[\text{GDGT-2}]}{[\text{GDGT-3}]} \qquad \textbf{(Eq. 1.24)}$$

1.4.5.1   Ring Index

The isoGDGTs produced at higher SSTs contain a greater number of cyclic groups than those produced in low SSTs. Another temperature-sensitive measure using isoGDGTs is the ring index (RI; Equation 1.25), which demonstrates the weighted number of cyclopentane rings within isoGDGTs 0-3, crenarchaeol and cren' (Zhang *et al.*, 2016).

$$\text{RI} = 0 \times[\%\text{GDGT-0}] + 1\times[\%\text{GDGT-1}] + 2\times[\%\text{GDGT-2}]+ 3\times[\%\text{GDGT-3}]$$

$$+ 4\times[\%\text{crenarchaeol} + \%\text{cren'}] \qquad \textbf{(Eq. 1.25)}$$

The abundance of GDGT-0 is not explicitly used within the calculation, yet the GDGT-0 abundance is needed to determine the proportion of each isoGDGT used within the calculation. The RI has been found to correlate strongly with other GDGT-derived values, including the GDGT-0/crenarchaeol ratio (r^2 = 0.996, n =531; Zhang *et al.*, 2016), where high GDGT-0 abundances produce lower RI values. The relationship between TEX_{86} and RI can be exploited to check for irregularities in distributions of lipids, leading to the inference of isoGDGTs produced by terrestrial, methanogenic or methanotrophic sources (Sluijs *et al.*, 2020).

Global datasets (Ho *et al.*, 2011; 2014; Kim *et al.*, 2010) combined by Zhang *et al.* (2016) showed the strong correlation between RI and GDGT-0/cren ratios (r^2 = 0.996, n = 531). Low RI values correspond to high GDGT-0/crenarchaeol ratios. The RI also correlates with other parameters, including TEX_{86}, SST and RI_{TEX}, a quadratic regression formed from Zhang *et al.* (2016; Equation 1.26):

$$RI_{TEX} = -0.77 \times TEX_{86} + 3.32 \times (TEX_{86})^2 + 1.59$$

($r^2 = 0.87$; $n = 531$; 2σ uncertainty = ± 0.30) **(Eq. 1.26)**

The residual of a samples ring index ($|\Delta RI$) can be used as an indicator of non-temperature influences on the GDGT distributions if values exceed 0.3 (Zhang *et al.*, 2016; Dauner *et al.*, 2021). Although specific links with biological sources are less clearly defined (Dauner *et al.*, 2021).

$$|\Delta RI| = RI_{TEX} - RI$$
(Eq. 1.27)

1.5   Method development for GDGT analysis

Through the development of HPLC-MS analytical methods the ability to analyse GDGT distributions has expanded allowing for the continued development of proxies (Hopmans *et al.*, 2000; 2016). With increased separation of eluents produced by HPLC, additional isomers and novel structures have been determined, allowing for the incorporation of the new structures into existing proxies or used in the development of new ones. Method development has not only occurred for the analytical aspects of analysis, but the extraction procedure also varies between different laboratories.

1.5.1 Extraction and analysis methodology within GDGT-based literature

The method of extraction of GDGTs from peat deposits, soils and sediments has not been standardised. Table A1, updated from Foster (2015), shows the compilation of 30 extraction methods from published works dated since the original paper by Hopmans *et al.* (2000) to 2022. Samples are almost universally freeze-dried, and often homogenised prior to extraction, but extraction and analytical methodologies vary between studies.

Initially workers (Hopmans *et al*., 2000; Schouten *et al*. 2002) used ultrasonic extraction methods in two stages, using a mixture of dichloromethane and methanol (DCM:MeOH, 1:1) followed by the less polar DCM. Later the use of Soxhlet extraction (SE; Sinninghe Damsté *et al*. 2002; Powers *et al*. 2005; Vickers *et al*. 2020) and accelerated solvent extraction (ASE; Weijers *et al*. 2007a; Blaga *et al*. 2009; Lawrence *et al*. 2020; Peaple *et al*. 2022) overtook ultrasonic extraction as preferred methods. Pearson *et al*. (2011) and Foster (2015) used microwave assisted extraction (MAE), highlighting the ability to extract many samples at once, with less solvent than with Soxhlet or ultrasonic extraction methods.

Kornilova & Rosell-Melé (2003) investigated the application of MAE in biomarker studies, comparing the method to ultrasonic extraction, the preferred extraction method at the time. For high-resolution paleoclimate reconstructions large numbers of samples need to be extracted, often with little sample material (ca. 1 g). Ultrasonic extractions were relatively inexpensive, but required multiple extractions to produce a good recovery, making it a time-consuming extraction method. SE often requires large amounts of sediments (Vickers *et al*. 2020), which is impractical in high-resolution studies. ASE and MAE methods are both less time consuming and utilise much smaller volumes of solvent, though commercial ASE systems are expensive (Kornilova & Rosell-Melé, 2003). Microwave methods allow multiple simultaneous extractions, using much smaller quantities of sample and solvent, leading Kornilova & Rosell-Melé (2003) to find it a viable extraction method. Huguet *et al*. (2010) found ASE, and thus MAE, methods result in inconsistent yields and advised the use of ultrasonic or SE methods. Time constraints may influence the extraction method chosen. The Soxhlet extracts completed by Huguet *et al*. (2010) took place over

72 h, whereas multiple samples can be extracted in under 10 minutes using MAE. Different research groups appear to favour different procedures, likely due to available equipment and funding, or time constraints (Foster, 2015).

GDGTs are insufficiently volatile for analysis by gas chromatography (GC) methods (Schouten *et al.*, 2013), and are instead detected and measured almost solely by LC-MS techniques, due to the initial method development of Hopmans *et al.* (2000) and subsequent advances in separation by Hopmans *et al.* (2016). There is little dispute over the analytical technique used to investigate isoGDGT and brGDGT abundances for use in biogeochemistry and paleothermometry. Analysis involves HPLC, typically coupled via atmospheric pressure chemical ionisation to mass spectrometric detection and often in selected ion-monitoring mode (SIM; HPLC-APCI-MS; Hopmans *et al.*, 2000; Lengger *et al.*, 2018).

Many workers, including Schouten *et al.* (2000; 2002), Powers *et al.* (2004; 2005), Weijers *et al.* (2007a), Pearson *et al.* (2011), Woltering *et al.* (2014), Ruan *et al.* (2017), Dugerdil *et al.* (2020) and Peaple *et al.* (2022), have used LC-MS for the analysis of GDGT membrane lipids, usually following methods developed by Hopmans *et al.* (2000; 2016). This approach relies on signal intensities of protonated molecules, $[M+H]^+$, relative to an internal standard (Lengger *et al.* 2018), though there are very few authentic standards for external calibrations. Huguet *et al.* (2006a) found that a synthesised C_{46} GDGT added to extracts could be used as an internal standard, as it eluted in the same fraction as the GDGTs, and independently from target compounds. An internal standard has been used in many studies (Tierney & Russel, 2009; Bechtel *et al.* 2010; Loomis *et al.* 2012; Lei *et al.* 2016; Ruan *et al.* 2017; Dearing Crampton-Flood *et al.* 2020) though it is not readily available, instead

reference materials are utilised. Quantification of GDGTs is not typically needed within current proxy calibrations, as it is the ratio of different GDGT structures that is measured, but the repeatability of samples should be assessed and achieved through replicates.

1.6   Study rationale

The reconstruction of past environments aids in the production of climate models which predict how the Earth will respond to future climatic changes (Masson-Delmotte *et al.*, 2013). Paleoclimate reconstructions provide a deeper understanding of natural climate variability and the impact external forcings, like human activity, have on global and regional scales. Systematic global observational networks of climate were only available from the middle of the 19th century (Zhang *et al.*, 2022; Chrisiansen & Ljungqvist, 2016), and therefore do not encapsulate the broad range of climate changes that previously occurred on Earth. Consequently, to understand a broader range of environmental and climatic variables, indirect measurements are reconstructed using proxy records (Zhang *et al.*, 2022). Temperature-sensitive proxy records typically are found in biological and geological archives including tree rings, ice cores, marine and terrestrial sediments (Chrisiansen & Ljungqvist, 2016). By reconstructing past temperatures, comparisons between the current global warming event and historical temperature excursions can be made.

The polar regions are more sensitive to climate change than the rest of the world, warming at almost twice the rate of the global average over recent decades (Casagrande *et al.*, 2021; Smith *et al.*, 2019). The Quaternary, the most recent period in Earth history, is defined by the quasi-periodic expansion and contraction of the NH ice sheets. Up until the Mid-Pleistocene Transition (MPT; ca. 1.25 – 0.7

Ma ago), G-IG cycles presented symmetrically, where glacial periods were approximately the same duration as the interglacial cycle, with less variation in sea ice volume over 41 kya periods. The MPT marked a change in frequency, to 100 kya cycles, where slow glaciations were followed by rapid deglaciations, with greater extremes in sea ice volume depicted in benthic $\delta^{18}O$ records (Detlif, 2018; Lisiecki & Raymo, 2005). Research involving reconstruction of climate across the Quaternary is vast, yet to date, limited temperature reconstructions have been completed within the sub-Arctic region, and fewer in this region across the latest G-IG cycle, which encompasses the last glacial maximum (LGM), where glaciers were at their greatest extent (Clark *et al.*, 2009). To better understand the mechanisms affecting ice retreat due to the current global warming event, a thorough knowledge of previous deglaciation events is essential (Wagner *et al.*, 2011).

1.6.1 Research Aims and Objectives

The main aim of this research project is to reconstruct SSTs in the Bering Sea by interpretation of the distribution of GDGTs extracted from marine sediments deposited off the Bering Sea shelf (BSS), proximal to the modern-day sea-ice edge, through the latest G-IG cycle, over a time period of approximately 160 kya.

The research objectives were:

1. Complete a small method development study, where two extraction processes and two analytical methods will be compared.

2. The extraction of GDGTs from sediments deposited in the Bering Sea across 160 kya.

3. The use of HPLC-APCI-MS to identify and quantify GDGTs.

4. Use GDGT distributions as a paleothermometer to determine TEX_{86} and SSTs, as well as the BIT index.

To achieve the aim and objectives a sediment core proximal to the modern sea ice edge in the Bering Sea, collected from depths that encompass the latest G-IG cycle and the LGM and covering a time of sedimentary deposition across ca. 160 kya, was analysed.

Chapter 2: Materials, Methods and Methodology

2.1   Site location and characterisation

The material used within this thesis is taken from archival material at Site U1343 from Expedition 323 of the Integrated Ocean Drilling Program (IODP). Expedition 323 was dedicated to the collection of marine sediment cores for the palaeoceanographic study of the Bering Sea. A total of 5741 m of sediment was collected across 7 locations, from the Umnak Plateau, Bowers Ridge and the Bering Sea shelf (Expedition 323 Scientists, 2010). The primary objectives of IODP Expedition 323 were to: characterise changes within the Bering Sea surrounding the intensification of the NH glaciation (2.7 Ma); the MPT (ca. 1.2 – 0.7 Ma); and the subsequent 100 kya G-IG cycles of the most recent 1 Ma (Iwasaki *et al.*, 2016; Takahashi *et al.*, 2009).

Site U1343 (Figure 2.1; 54°33.4′N, 176°49.0′E, water depth ca. 1950 m) is located adjacent to the northern continental shelf, a topographic high within the Bering Sea green belt, proximal to the modern winter sea-ice edge (Worne *et al.*, 2019), where biological productivity has been found to be greatest (Stabeno *et al.*, 1999). Biological productivity is thought to be sensitive to changes in sea surface conditions, including temperature (Iwasaki *et al.*, 2016; Takahashi *et al.*, 2002).

The MPT is important as it saw a shift in the frequency of G-IG cycles, from ca. 41 kya to 100 kya. The LR04 stack (Figure 2.2; Lisiecki & Raymo, 2005) shows increased asymmetry in the G-IG cycles, with slow glaciations followed by rapid deglaciations, and generally greater $\delta^{18}O$ values indicate larger continental ice volume or a decrease in deep ocean temperatures, or both (Detlif, 2018).
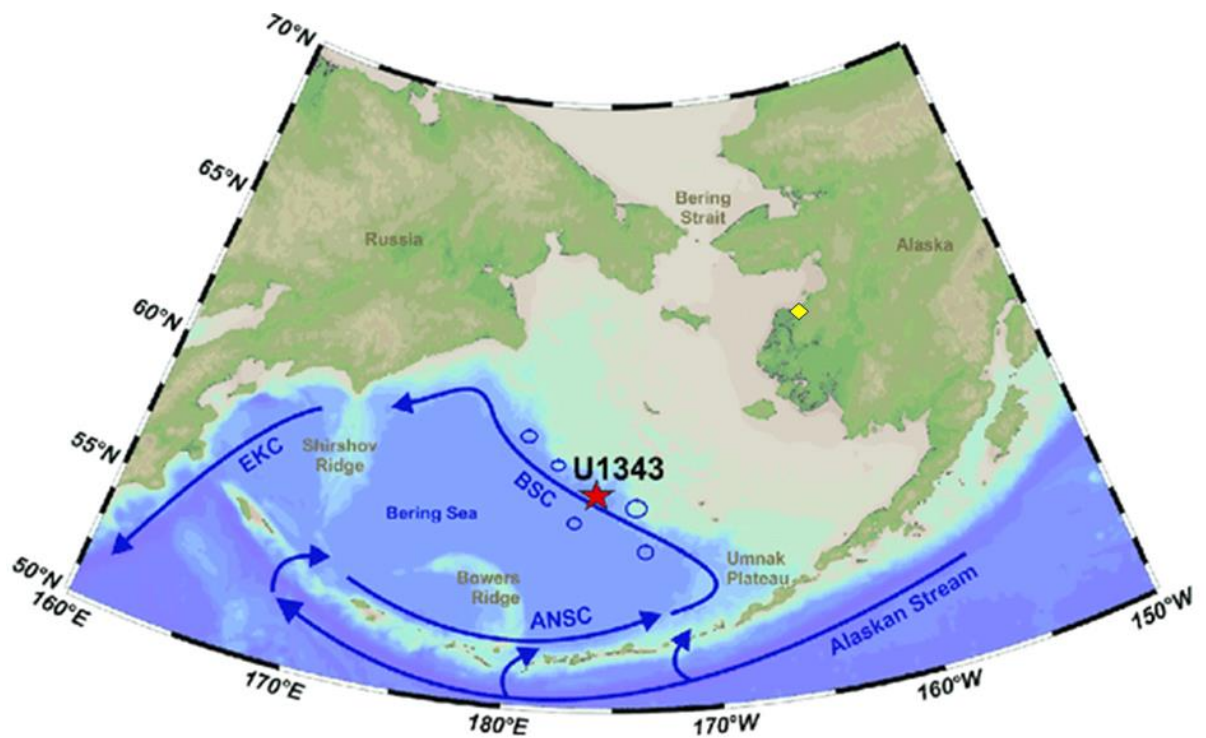
Figure 2.1. Map of the Bering Sea, showing the core location of IODP Site U1343 (54°33.4′N, 176°49.0′E; red star), the mouth of the Yukon river (yellow diamond), the surface cyclonic anti-clockwise water circulation in the basin is shown (blue arrows). Figure adapted from Detlef *et al.* (2020).

Sedimentation rates were found to be high at Site U1343, ranging between 21 – 58 cm kyr $^{-1}$ (Takahashi *et al.*, 2011). Such high sedimentation rates are attributed to the deposition of silt and clay transported from the rivers, including the Yukon, as well as high terrigenous contributions from the continental shelf. Biotic proxies including benthic foraminifera have been found to be well preserved (Takahashi *et al.*, 2011), and the large terrigenous contribution may allow for the reconstruction of terrestrially-derived proxies, as well as those of a marine origin.

2.2   Foraminiferal Oxygen Isotopes and Age Model

The preservation of foraminifera is notably good at Site U1343 (Worne *et al.*, 2019), as opposed to other subarctic sites, where calcareous planktonic

43

microfossils are sparse owing to the North Pacific lysocline, which limits

carbonate preservation (Takahahi *et al.*, 2011; Chen *et al.*, 2014; Worne *et al.*,

2019). Few high-resolution δ¹⁸O age models have therefore been produced in

the Bering Sea. Previous benthic foraminiferal δ¹⁸O analyses of Site U1343

show the G-IG cycling of MIS stages (Figure 2.2; Asahi *et al.*, 2016; Worne *et*

al., 2019) spanning 500 kya.
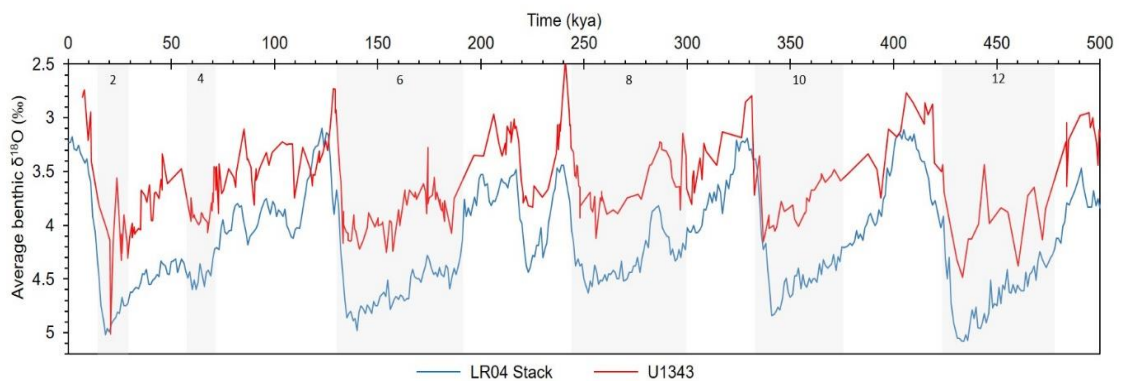
Figure 2.2. Combined benthic foraminiferal δ¹⁸O results for IODP Site U1343

(from Asahi *et al.*, 2016 and Worne *et al.*, 2019) compared to those produced by

the combined LR04 Stack of Liseicki & Raymo (2005) spanning 500 thousand

years.

The U1343 sediments contained large amounts of clay and diatoms, with little

input of shelf-transported materials (Takahashi *et al.*, 2011; Worne *et al.*, 2021).

Small proportions of ash, sand, foraminifers, calcerous nannofossils and

sponge spicules also feature (Expedition 323 Scientists, 2010).

Previous palaeoceanographic reconstructions at IODP Site U1343 have

demonstrated its potential to provide an archived marine sediment worthy of

biogeochemical investigation. Surface-water productivity (Kim *et al.*, 2014), sea-

ice dynamics (Detlef *et al.*, 2018; Worne *et al.*, 2021) and benthic foraminiferal

oxygen isotope stratigraphy studies (Asahi *et al.*, 2016; Kender *et al.*, 2018)

have been conducted for Site U1343, but climate reconstructions have not been conducted for the site using organic biogeochemical proxies to date.

2.3   Age Model and Sample Selection

IODP sediment cores were collected by workers on the programme in the Bering Sea, during Expedition 323 for palaeoceanographic study (5th July – 4th September 2009). Sediment was collected across 7 locations, from the Umnak Plateau, Bowers Ridge and the Bering Sea shelf (Expedition 323 Scientists, 2010). Five samples were cored at Site U1343, reaching a total depth of 744 metres below the seafloor (mbsf). Sediments collected from U1343E have been used to produce an age-depth model (Asahi *et al.*, 2016).

This was considered a key site as sediments spanned the last full G-IG cycle and was located close to the sea-ice boundary of the present day, where sea ice cover would likely have expanded and retracted through stadial and interstadial cycling, encompassing the last ca. 160 kya (MIS 1 to 6), on the lead up to, and throughout the last G-IG cycle.

An age model produced by Asahi *et al.* (2016; 2020, personal communication, 12 May) allowed the identification of MIS transitions and aided the sediment selection process. Sediment samples were ordered from the Kochi Core Centre in Japan, where IODP Expedition 323 sediments are stored. Samples were taken at approximately 2 kya intervals (or 75 cm in depth), with increased resolution across the MIS boundaries of approximately 0.5 kya (or 25 cm in depth).

The sediment samples had a core sample identification code (Table 2.1), simplified identification codes for the purpose of this study are also included,

alongside lithology and age approximations based on the calibration of Asahi *et al.* (2016; 2020, personal communication, 12 May).

Table 2.1. Sediment samples as identified by IODP and the simplified code used in this project, alongside approximate ages as determined by Asahi *et al.* (2020, personal communication) and lithology (Takahashi *et al.*, 2011).

Core Sample Identification	Simplified Identification Code	Approx. Age / kya	Primary Lithology
323 - U1343E – 1H – 1W – 99 – 101 cm	MIS_1A (2)	10.23	Clayey silt
323 - U1343E – 1H – 2W – 75 – 77 cm	MIS_1B (5)	13.56	Clayey silt
323 - U1343E – 1H – 2W – 99 – 101 cm	MIS_2A (8)	14.19	Clayey silt
323 - U1343E – 1H – 3W – 20 – 21 cm	MIS_2B (9)	16.05	Clayey silt
323 - U1343E – 1H – 3W – 101 – 103 cm	MIS_2C (12)	18.27	Clayey silt
323 - U1343E – 1H – 5W – 26 – 28 cm	MIS_2D (15)	27.08	Clayey silt
323 - U1343E – 1H – 5W – 99 – 101 cm	MIS_3A (16)	30.09	Clayey silt
323 - U1343E – 2H – 1W – 104 – 106 cm	MIS_3B (19)	39.37	Clayey silt
323 - U1343E – 2H – 3W – 26 – 28 cm	MIS_3C (22)	48.07	Clayey silt
323 - U1343E – 2H – 4W – 102 – 104 cm	MIS_3D (25)	55.45	Clayey silt
323 - U1343E – 2H – 5W – 30 – 32 cm	MIS_4A (26)	57.99	Clayey silt
323 - U1343E – 2H – 6W – 104 – 106 cm	MIS_4B (29)	65.38	Clayey silt
323 - U1343E – 3H – 1W – 36 – 38 cm	MIS_4C (32)	69.51	Clayey silt
323 - U1343E – 3H – 1W – 79 – 81 cm	MIS_4D (34)	70.64	Clayey silt
323 - U1343E – 3H – 1W – 101 – 103 cm	MIS_5A (35)	71.22	Clayey silt
323 - U1343E – 3H – 2W – 49 – 51 cm	MIS_5B (38)	73.81	Clayey silt
323 - U1343E – 3H – 3W – 125.5 – 127.5 cm	MIS_5C (41)	79.80	Clayey silt
323 - U1343E – 3H – 5W – 49 – 51 cm	MIS_5D (44)	85.68	Clayey silt
323 - U1343E – 3H – 6W – 94 – 96 cm	MIS_5E (47)	90.83	Clayey silt
323 - U1343E – 4H – 1W – 79 – 81 cm	MIS_5F (49)	95.71	Clayey silt
323 - U1343E – 4H – 2W – 79 – 81 cm	MIS_5G (51)	99.67	Clayey silt

323 - U1343E –4H – 4W – 19 – 21 cm	MIS_5H (54)	106.0	Clayey silt
323 - U1343E –4H – 5W – 79 – 81 cm	MIS_5I (57)	112.3	Clayey silt
323 - U1343E – 4H – 6W – 109 – 111 cm	MIS_5J (60)	122.4	Clayey silt
323 - U1343E – 4H – 7W – 31 – 33 cm	MIS_5K (63)	128.2	Clayey silt
323 - U1343E – 4H – 7W – 52 – 54 cm	MIS_6A (64)	130.3	Clayey silt
323 - U1343E – 5H – 1W – 133 – 135 cm	MIS_6B (67)	134.4	Clayey silt
323 - U1343E – 5H – 1W – 54 – 56 cm	MIS_6C (69)	141.0	Clayey silt
323 - U1343E – 5H – 2W – 104 – 106 cm	MIS_6D (72)	149.7	Clayey silt
323 - U1343E – 5H – 4W – 31 – 33 cm	MIS_6E (75)	160.5	Clayey silt

The increase in resolution across boundaries clearly define abrupt atmospheric temperature shifts, whereas sea temperatures generally change over a greater timescale. Figure 2.3 depicts the age-depth points of Site U1343 sediments by Asahi *et al.* (2016), with the samples ordered from IODP for climatic investigation (red crosses), and the samples that underwent LC-MS analysis for GDGT ratio determination in this study (yellow diamonds). $\delta^{18}O$ records from both the LR04 stack produced by Lisiecki & Raymo (2005; dark blue; secondary axis) and Site U1343 (Asahi *et al.*, 2016; Worne *et al.*, 2019; light blue; secondary axis) are also plotted.

Sediments throughout MIS 1 through 6 were deposited during the Holocene and late Pleistocene, encompassing stadials and interstadials, as well as the most recent full G-IG cycle, with climatic changes most like those projected in the present.
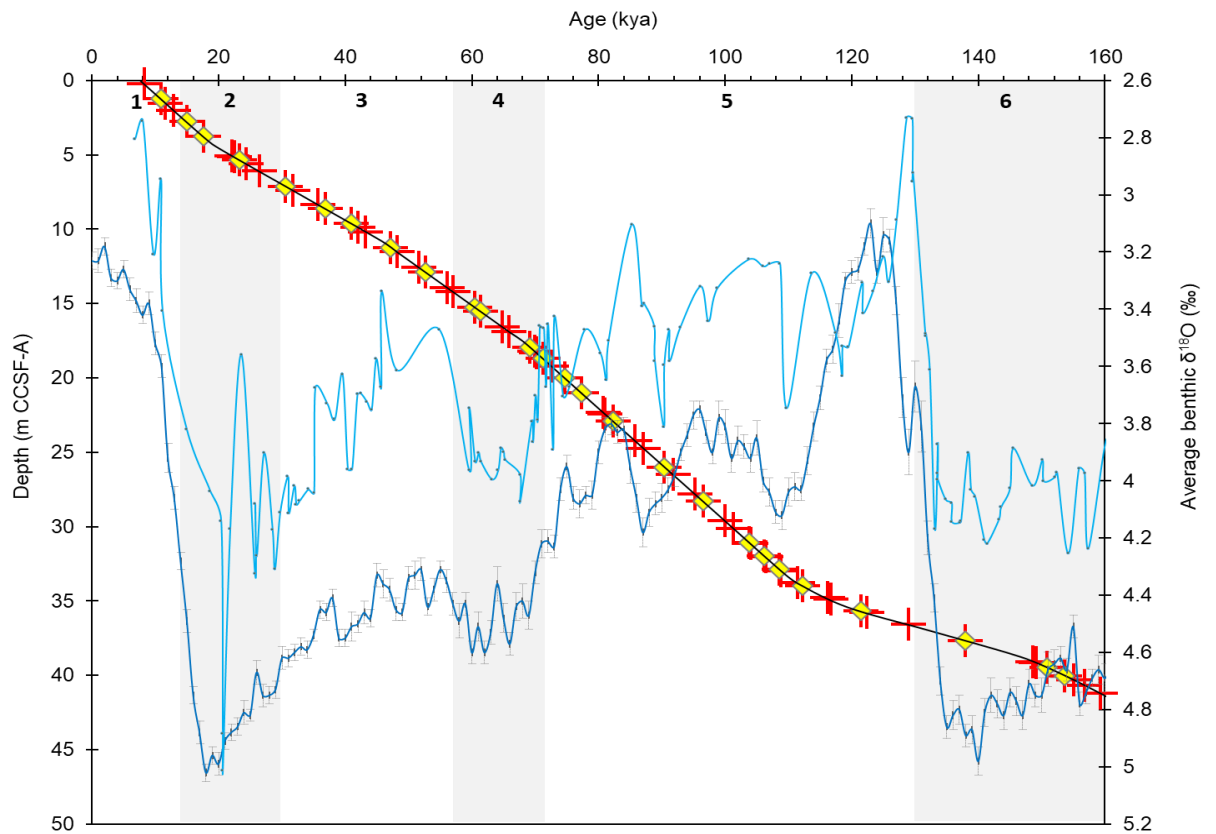
Figure 2.3. Age-depth time tie points by Asahi (2020; black) plotted alongside benthic δ¹⁸O data for U1343 (Asahi *et al.*, 2016; Worne *et al.*, 2019; light blue), and the global average LR04 stack (Lisiecki & Raymo, 2005; dark blue). The age-depth tie points of the sediments ordered are plotted (red crosses), with the sediments that underwent GDGT analysis (yellow diamonds) also plotted.

2.4   Laboratory Procedures

All further preparation and analyses were conducted within laboratories in the Davy Building at the University of Plymouth. Solvents (LC-MS grade) were purchased from Rathburn Chemicals (hexane) and Fisher Scientific (hexane and propan-2-ol; IPA) for LC-MS analysis. Vials and caps for GC and LC-MS analysis, and Decon-90, were also purchased from Fisher, while the vials used throughout the procedure were ordered from Merck, along with 0.45 µm PTFE syringe filters.

2.4.1 Cleaning Procedure for Sediment Molecular Analysis

Glassware was heated in a muffle furnace at 450 °C for 4 hours, removing any organic material present on the glass that may lead to contamination. Glass wool, sodium sulfate and alumina were also cleaned in the furnace. Glass wool was sealed and stored at room temperature, whereas the alumina and sodium sulfate were stored in a drying oven at ca. 40 °C prior to use. Measuring cylinders and micro-syringes were not furnaced and were instead rinsed with solvent prior to use. All glassware received three washings of MeOH, followed by three washings of DCM, and a minimum of two washes with the solvent used.

Prior to use, Teflon microwave extraction vessels were placed in a solution of Decon 90 and deionised water for a minimum of 12 hours, then rinsed with Milli-Q water and a soft sponge, before being placed in a 3% nitric acid bath overnight. Acid residue that may have diffused onto the Teflon was washed off with 3 Milli-Q water (18.2 MΩ cm) rinses before the vessels were transferred to a drying oven for 2 h at 130 °C. Finally, vessels were rinsed with Milli-Q water, acetone, MeOH and DCM.

2.4.2 Preparation of Sediments

The seventy-five sediment samples used in this research were stored in the freezer (-20 °C). Approximately 2.5 g of wet sediment was weighed out prior to undergoing freeze-drying, at -53 °C and 91 µbar, for 48 hours. Dried sediments were reweighed to determine percentage water content. Masses and percentage water content values are shown in SM1. Freeze-dried sediments were homogenised using an ashed pestle and mortar and ca. 1 g subsamples

were placed into pre-cleaned Teflon microwave extraction vessels to undergo MAE.

2.4.3 Extraction of GDGTs and other Organic Biomarkers

The schematic for the extraction method is in Figure 2.4. The sediment subsamples, along with six procedural blanks, were combined with 12 mL of DCM:MeOH (2:1, v/v); the reaction vessels were sealed and placed in a microwave extractor (MARS 5 microwave assisted solvent extraction system). The extraction programme increased in temperature for five minutes, up to 70 °C. After an isothermal hold at 70 °C for 10 minutes, the heating element was removed, and the vessels left to cool for 25 minutes (eg. Hou *et al*., 2023; Letellier & Budzinski, 1999).

Following 5 minutes of centrifugation, at 1700 revolutions per minute (rpm), the supernatant containing the total organic extract (TOE) was collected. A further two centrifuge cycles were conducted, following the addition of 10 mL DCM:MeOH (2:1, v/v) to the sediment each time, and the collected supernatants were combined for each sample. After, the combined TOE was filtered through a glass Pasteur pipette plugged with glass wool, dried over a sodium sulfate column, spiked with 5α-Androstane as an internal standard, dried under nitrogen, then TOE weighed (masses shown in SM1) and separated into three fractions based on polarity by small-scale chromatography using silica chromatography columns, yielding apolar, ketone and polar fractions respectively (Müller *et al*., 1998; Schouten *et al*., 1998; Sicre *et al*., 2002). The first, apolar fraction, was extracted with 3 mL hexane:DCM (9:1, v/v); the second used 3 mL hexane:DCM (1:1, v/v), and the third, GDGT containing fraction, was eluted with 4 mL DCM:MeOH (1:1, v/v; Castañeda *et al*., 2009;

Lopes dos Santos *et al.*, 2010). All fractions were dried under nitrogen at 25 °C.

Extracts were reweighed and stored in the freezer (-20 °C) prior to analysis. The

weights are displayed in SM1.
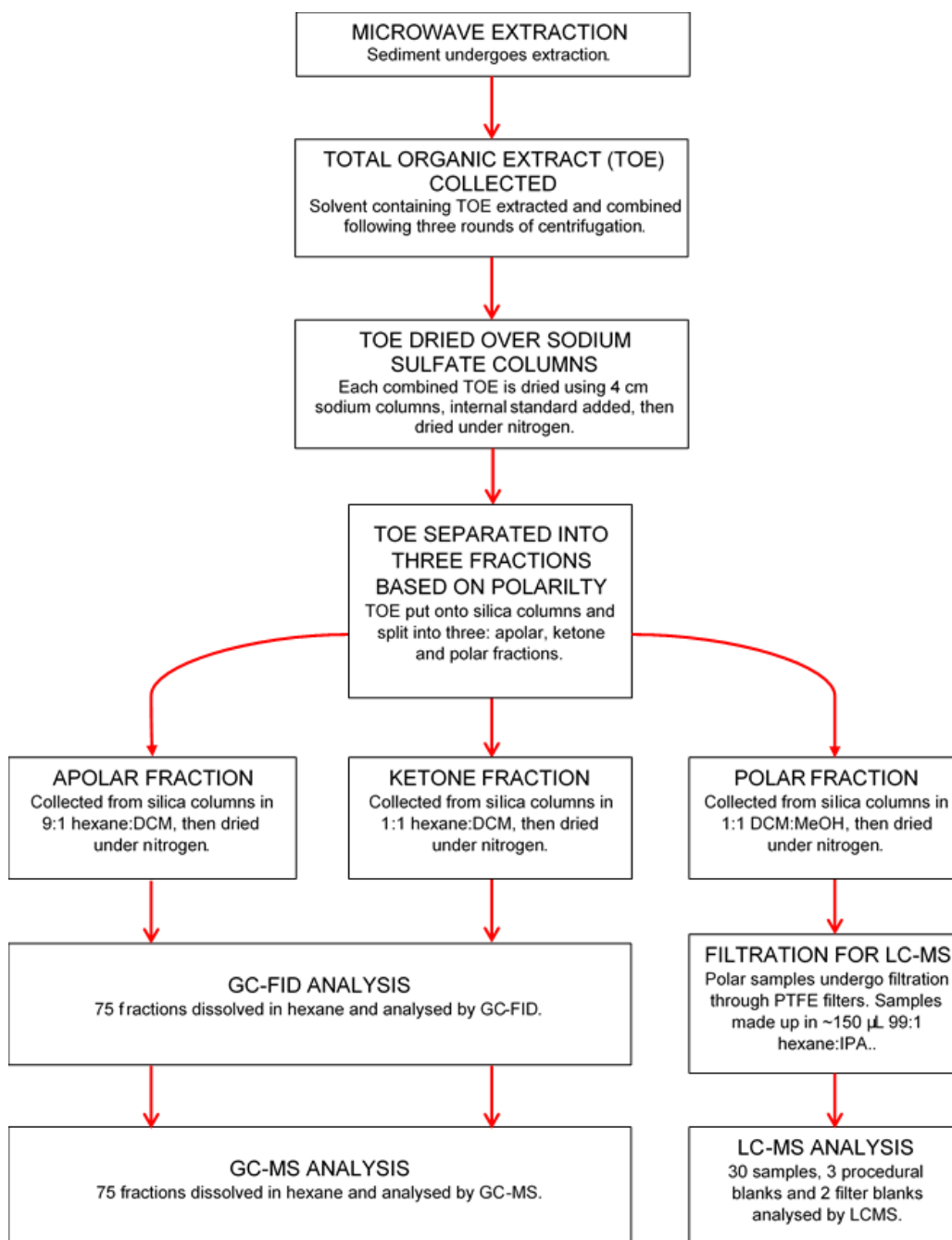
Figure 2.4. Schematic of the laboratory process followed for organic biomarker

extraction and analysis.

2.4.4 Analysis by Gas Chromatography – Flame Ionisation Detection

Apolar and ketone fractions were transferred into chromatography insert vials (Fisher Scientific: Chromacol crimp top fixed insert borosilicate 0.3 mL) with ca. 150 µL LCMS grade hexane, prior to preliminary analysis by gas chromatography flame ionisation detection (GC-FID). All vials were vortexed within 6 h of the analysis time.

An Agilent Technologies 7683B series injector and an Agilent Technologies 7890A GC system was coupled to a flame ionisation detector held at 300 °C. The split-splitless inlet was used in splitless mode at 300 °C, with 1 µL injected onto a DB-1 (30 m × 0.32 mm i.d. × 0.25 µm) column. Hydrogen was used as a carrier gas with a flow rate of 3 mL min^{-1}. The FID had 350 mL min^{-1} air, 35 mL min^{-1} hydrogen and 40 mL min^{-1} helium gas held at 320 °C. The oven temperature programme was held at 70 °C for 60 s, increased from 70 to 130 °C at 20 °C min^{-1}, then to 320 °C at 5 °C min^{-1}, and held isothermal for 10 min. The total runtime was 52 min.

2.4.5 Analysis by Gas Chromatography – Mass Spectrometry

Following analysis by GC-FID, selected samples underwent dilution with hexane prior to analysis by gas chromatography mass spectrometry (GC-MS). Most samples were diluted by a factor of 4 or 5, to ensure an appropriate response height that would form Gaussian shaped peaks while not overloading the column. An Agilent 7890A GC coupled with a 5975 series mass selective detector (MSD) was used with an Agilent DB-5MS UI (30 m × 0.32 mm i.d. × 0.25 µm film thickness) column and a 6783B series autoinjector. A split/splitless injector was used in splitless mode, injecting 1 µL at 300 °C with helium carrier

gas (1 mL min^{-1} constant flow). Total ion current (TIC) chromatograms were produced to identify compounds, with an electron voltage of -70 eV. The GC oven was heated to 70 °C and held for 1 minute before temperatures increased to 130 °C at 20 °C min^{-1}, then 130 to 320 °C at 5 °C min^{-1}, then held isothermal at 320 °C for 10 minutes; the same as the GC-FID method, shown in Figure 2.5.

2.4.6 Analysis by Liquid Chromatography – Mass Spectrometry

Once dried under nitrogen, polar fractions were diluted in hexane:IPA (99:1, v/v) and sonicated for 2 minutes, prior to being filtered through 0.45 µm PTFE syringe filters that had been pre-conditioned with both IPA and a hexane:IPA (99:1, v/v) mix. Samples were made up in 150 µL hexane:IPA (99:1, v/v) for analysis.

Thirty of the polar extracts were analysed by HPLC-APCI-MS as by Vickers *et al.* (2020) alongside 6 reference materials, 3 procedural blanks and 2 filter blanks. A Dionex low pressure gradient pump (LPG-U3400) with a normal phase piston seal pump (SDN) ultra-HPLC system was coupled with a Thermo Scientific Q Exactive Focus mass spectrometer used with Atmospheric Pressure Chemical Ionisation (APCI). The method originally proposed by Hopmans *et al.* (2000) was adapted for use on the high-performance instrument. A single Waters Acquity, ethylene bridged hybrid (BEH) hydrophilic interaction liquid chromatography (HILIC) column, of dimensions 150 mm × 2.1 mm × 1.7 µm was used, alongside a precolumn held at 40 °C. The solvent flow rate remained at 600 µL min^{-1} throughout the 20 min runtime. Solvent gradients changed throughout, decreasing hexane and increasing the hexane:IPA (9:1, v/v) mix. The percentage of hexane/IPA was increased throughout the runtime, held isocratic at 5% between 0 and 3 min, increasing to 18% at 5 min and held

isocratic to 10 min, before increasing again to 35% at 15 min, and 100% at 17.4 min, followed by 2.6 min of re-equilibrium time.

2.5   Data Interpretation

Chromatograms produced by GC-FID were used for qualitative identification in some cases but were predominantly used to determine whether the concentration of extracts were suitable for identification on the GC-MS, where the largest peak height should be about 100 Au. Most samples were diluted by a factor of 4. Analysis through GC-MS led to the identification of limited groups of molecules using the MSD ChemStation Data Analysis software, such as alkanes, that can act as proxies for paleoenvironmental reconstruction. Single ion chromatograms were extracted to determine alkane presence, with a mass-to-charge (*m/z*) value of 57 (Shinozaki, 2023).

The presence of GDGTs in polar extracts was determined through HPLC-APCI-MS by single-ion filtration using m/z ratios. The *m/z* values targeted the $[M+H]^+$ ions. The targeted *m/z* values for isoGDGTs and brGDGTs are in Table 2.2. This was completed using the Xcalibur 4.2 using QuanBrowser integration and data management software. An example chromatogram (ID: MIS_6B (67), Age: ~134.4 kya) is shown in Figure 2.5, where GDGTs have been identified following extraction of their respective m/z values.

Table 2.2. isoGDGTs and brGDGTs mass-to-charge values from LC-MS analysis alongside approximate LC-MS elution times.

Molecule	Mass-to-charge (*m/z*) value	Approximate elution time / min
GDGT-0	1302.32267	7 – 9
GDGT-1	1300.30702	
GDGT-2	1298.29137	
GDGT-3	1296.27572	
Crenarchaeol / Crenarchaeol'	1292.24442	
brGDGT Ia	1022.00967	13.5 - 15
brGDGT Ib	1019.99402	
brGDGT Ic	1017.97837	
brGDGT IIa and brGDGT IIa'	1036.02532	12.5 – 13.7
brGDGT IIb and brGDGT IIb'	1034.00967	
brGDGT IIc and brGDGT IIc'	1031.99402	
brGDGT IIIa and brGDGT IIIa'	1050.04097	11.4 – 12.8
brGDGT IIIb and brGDGT IIIb'	1048.02532	
brGDGT IIIc and brGDGT IIIc'	1046.00967	
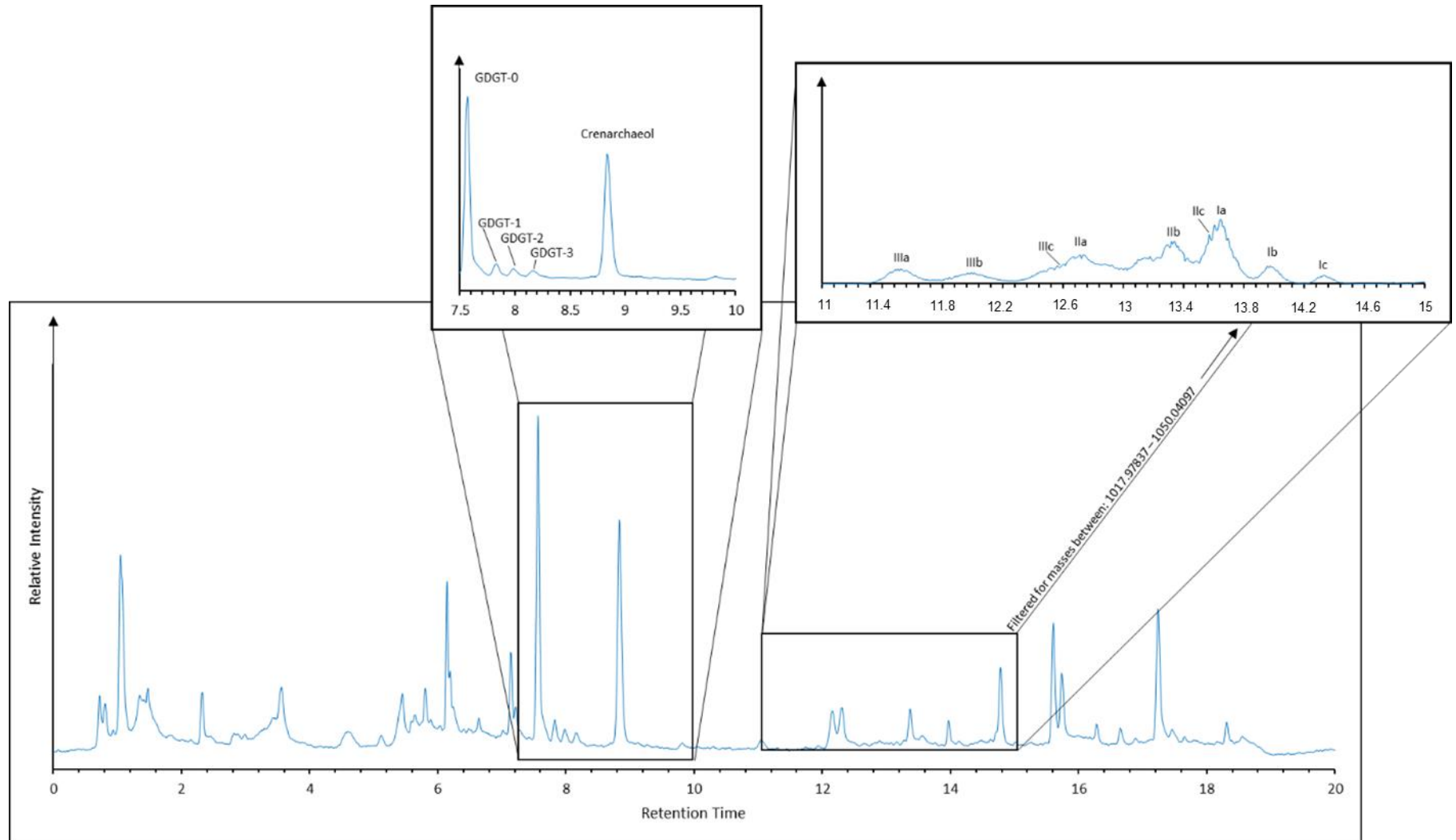
Figure 2.5. An example chromatogram (ID: MIS_6B (67), Age: ~134 kya) from LC-MS analysis, with identified isoGDGTs labelled, with approximate elution times identified (Table 2.2).

The equations that are to be used throughout the GDGT study of U1343 are listed in

Table 2.3, where abundance and ratios of differing GDGT molecules allow.

Table 2.3. Formulae used for the GDGT derived calculations in this study

Index	Formula	Reference	Eq. Number
TEX_{86} TEX_{86}^{L}	$= \dfrac{[GDGT\text{-}2]+[GDGT\text{-}3]+[cren']}{[GDGT\text{-}1]+[GDGT\text{-}2]+[GDGT\text{-}3]+[cren']}$ $= \log \dfrac{([GDGT\text{-}2])}{([GDGT\text{-}1])+([GDGT\text{-}2])+([GDGT\text{-}3])}$	Schouten *et al.* (2002) Kim *et al.* (2015)	Eq. 1.4 Eq. 1.7
TEX_{86} SSTs	$= (TEX_{86}\text{-}0.28)/0.015$ $= 67.5 \times TEX_{86}^{L} + 46.9$ $= \text{-}16.332 \times (1/TEX_{86}) + 50.475$ $= \text{-}19.1 \times (1/TEX_{86}) + 54.5$	Schouten *et al.* (2002) Kim *et al.* (2015) Lui *et al.* (2009) Kim *et al.* (2010)	Eq. 1.5 Eq. 1.8 Eq. 2.1 Eq. 2.2
BIT	$= \dfrac{Ia+IIa+IIa'+IIIa+IIIa'}{Ia+IIa+IIa'+IIIa+IIIa'+crenarchaeol}$	Hopmans *et al.* (2004) De Jong *et al.* (2015)	Eq. 1.11
$MBT'5_{Me}$	$= \dfrac{Ia+Ib+Ic}{Ia+Ib+Ic+IIa+IIb+IIc+IIIa}$	De Jonge *et al.* (2014)	Eq. 1.19
CBT'	$= \log \left(\dfrac{Ic + IIa' + IIb'+IIc' +IIIa' +IIIb' + IIIc'}{Ia + IIa + IIIa} \right)$	De Jonge *et al.* (2014)	Eq. 1.20
Methane Index	$= \dfrac{[GDGT\text{-}1]+[GDGT\text{-}2]+[GDGT\text{-}3]}{[GDGT\text{-}1]+[GDGT\text{-}2]+[GDGT\text{-}3]+[cren]+[cren']}$	Zhang *et al.* (2011)	Eq. 1.21
GDGT-0 / Cren	$= \dfrac{GDGT\text{-}0}{crenarchaeol}$	Blaga *et al.* (2009)	Eq. 1.22
%GDGT-0	$= \dfrac{[GDGT\text{-}0]}{[GDGT\text{-}0] + [crenarchaeol]} \times 100$	Sinninghe Damsté *et al.* (2012)	Eq. 1.23
GDGT-2 / GDGT-3	$= \dfrac{[GDGT\text{-}2]}{[GDGT\text{-}3]}$	Blaga *et al.* (2009)	Eq. 1.24
Ring Index	$= 0 \times [\%GDGT\text{-}0] + 1\times[\%GDGT\text{-}1] + 2\times[\%GDGT\text{-}2] + 3\times[\%GDGT\text{-}3] + 4\times[\%crenarchaeol + \%cren']$	Zhang *et al.* (2016)	Eq. 1.25
RI_{TEX}	$= \text{-}0.77\times TEX_{86} + 3.32\times (TEX_{86})^{2} + 1.59$	Zhang *et al.* (2016)	Eq. 1.26
MAT_{Peat}	$= (52.18\times MBT'5_{Me}) - 23.05$	Naafs *et al.* (2017b)	Eq. 2.3
MAT_{Soil}	$= (40.01\times MBT'5_{Me}) - 15.25$ $= (31.45\times MBT'5_{Me}) - 8.57$	Naafs *et al.* (2017a) De Jong *et al.* (2014)	Eq. 2.4 Eq. 2.5
CBTPeat	$= \log \left(\dfrac{Ib + IIa' + IIb+IIb' +IIIa}{Ia + IIa + IIIa} \right)$	Naafs *et al.* (2017a)	Eq. 2.6
pH	$= (1.59 \times CBT') + 7.15$ $= (2.49 \times CBT') + 8.07$	De Jong *et al.* (2014) Naafs *et al.* (2017b)	Eq. 2.7 Eq. 2.8

2.6 Method development study

Both Soxhlet extraction (SE) and microwave extraction (MW) were used on sediments in a small method development study to determine whether a method showed greater efficiency, allowing the signals to be reliably integrated for peak areas or extracted a greater number of compounds. Ratios of the GDGT molecules found in each sample were used to determine different environmental parameters that occurred at the time of sedimentation, including sea and atmospheric temperatures, through proxy calculations. Two distinct analytical methods were also tested, termed 'short method' with a 20-minute runtime and the 'long method', with a run time of 110 minutes, used to determine whether a longer runtime led to the better separation of individual compounds.

2.6.1 Laboratory extraction methods used in the pilot study

Five sediments from U1343 were used for a method development study, testing out two different methods of extraction: SE and MW. The use of SE for sediment extraction had previously been used to extract GDGTs and other organic biomarkers (Sinninghe Damsté *et al.*, 2002; Powers *et al.*, 2004; Vickers *et al.*, 2020), requiring a larger amount of sediment (ca. 4 g) compared to MW methods that used ca. 1 g and required less solvent. The samples termed: 1H-02, 1H-04, 2H-05, 4H-07 and 5H-02, were first freeze-dried as outlined in Section 2.4.2, then divided into two, with ca. 4.00 g being used for SE and ca. 1.00 g used for MW.

The MAE method for the pilot samples was the same as detailed in Sections 2.4.1 to 2.4.3. For SE, 6 Soxhlet apparatus were set up with 200 mL DCM:MeOH (2:1, v/v), with thimbles empty and 3 anti-bumping granules added.

Soxhlet extractors were then turned on at 40 °C for 4 hours to clean the glassware. Then, the solvent was replaced, approximately, 4 g of sediment, reweighed after the freeze-dry process, was placed in each thimble. One was left empty to act as a procedural blank and Soxhlet extractors were then left for 24 hours, at 40 °C.

Following the initial extraction method, SE or MW, the eluent was then dried over sodium sulfate and separated into three fractions relating to polarity: apolar, ketone and polar, as described in section 2.4.3. Polar fractions were filtered through 0.45 µm PTFE filters and made up in 150 µL 99:1 hexane:IPA solvent prior to HPLC-APCI-MS analysis.

2.6.2 Analytical methodology in the pilot study

Polar lipid extracts from SE and MW were both analysed by LC-MS, using two methods, termed the *'short method'*, with a 20-minute runtime (detailed in Section 2.4.6; Vickers *et al.*, 2020) and the *'long method'*, with a run-time of 90 minutes followed by 20 minutes equilibration time (Hopmans *et al.*, 2016). Both methods are routinely used for in-house analysis.

The use of HPLC-MS enables the separation of branched and isoprenoid structures, and independent molecules due to different numbers of cyclopentane moieties. Increasing the runtime can separate compounds that often co-elute, such as crenarchaeol and GDGT-4. Individual, or groups of compounds, were isolated from the TIC (total ion chromatograph) by filtering out mass numbers, or ranges using SIM.

Representative chromatograms produced following MW and SE in the pilot study, from both the short and long analytical methods are displayed in Figures 3.1. Total ion current chromatograms were filtered for the individual m/z values

stated in Table 2.2, and the peak area for each molecule recorded and inputted into TEX_{86}^L (Equations 1.7 and 1.8) and the BIT Index (Equation 1.11), which allowed comparisons to be made between both extraction and analytical methods (Tables 3.1 and 3.2).

2.7   Quality control

The method development study emphasised the need to check the validity of the data produced from the full study, as temperature reconstructions have been found to deviate up to 5 °C between methods, outside the expected deviations from the round-robin study (1 – 3 °C; Schouten *et al.*, 2013b). Therefore, to evidence the validity of the data produced, four reference materials (including EH-8 as described in Lengger *et al.* 2018 and RCW-26 from O'Connor *et al.*, 2023) were analysed by LC-MS alongside the polar extracts of U1343 sediments, as well as two in-house reference standards reflecting the marine and peat environments (Vickers *et al.*, 2020). The four reference materials, alongside the marine and peat standards, were analysed by LC-MS in duplicate to check for consistency throughout the sequence. This also allowed for comparison with other studies to validate the analytical methodology through use of the BIT index and TEX_{86}.

Six procedural blanks were analysed throughout the analytical sequence, as well as two filter blanks. This was to ensure there was no interfering contamination present between samples, and to make sure no sample was carried over between analytical injections and used to calculate limits of detection (LOD) for GDGT evaluation.

Chapter 3: Results and Discussion

3.1   Method development study

The method development study was completed as outlined in Section 2.5. Comparisons were made between SE, MAE and the 'long' and 'short' analytical LC-MS runtimes. Example chromatograms are shown in Figure 3.1.
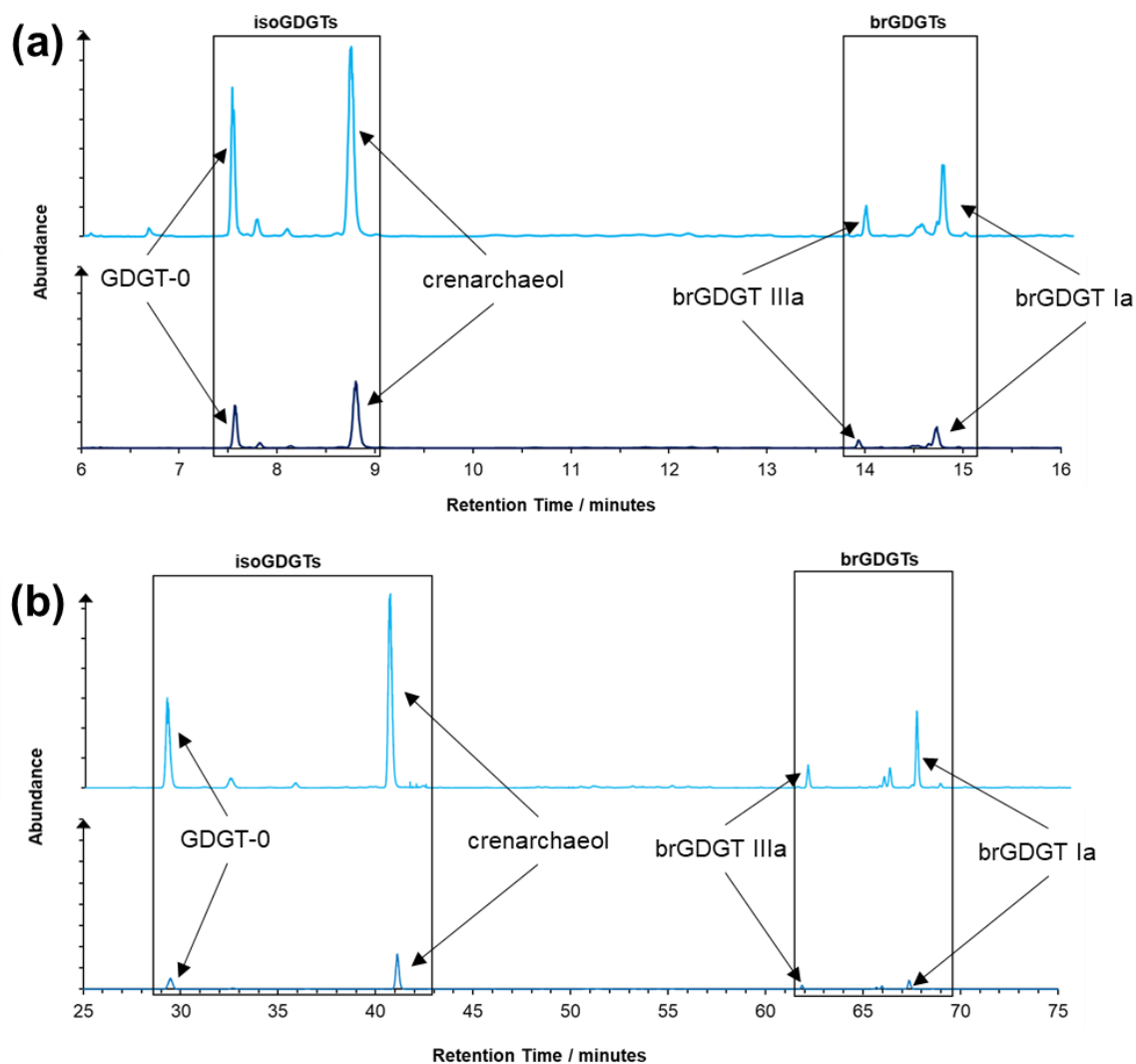
Figure 3.1. Representative chromatograms produced using (a) the short method on the HPLC-MS following both Soxhlet (light blue) and microwave (dark blue) extraction methods and (b) representative chromatograms from the long method on the HPLC-MS following both Soxhlet (light blue) and microwave (dark blue) extraction. Some key GDGT molecules are labelled.

Figure 3.1(a) depicts a 20-minute analytical runtime where isoGDGTs elute between 7 and 10 minutes, and brGDGTs elute between 13 and 16 minutes. The SE and MAE methods both displayed reasonable responses for the analytes of interest. Relative abundances show very little difference between chromatograms with ratios between analytes almost identical, but absolute abundances show a decreased signal for the MAE methods though signals were more than sufficient to determine peak area which are inputted into equations that give rise to environmental data at sedimentation.

An increased runtime allows for greater separation between the eluting molecules and therefore molecules that typically co-elute in shorter runtimes can be distinguished. Figure 3.1(b) shows increased separation, with isoGDGTs eluting between 29 and 43 minutes and brGDGTs eluting between 61 and 69 minutes

As with the short run time, MAE showed a decreased absolute abundance when compared to SE. The peak areas of each GDGT molecule were readily determined using either analytical method, either following single-ion filtration, or by viewing the chromatograms with their relative abundances rather than with absolute abundances.

Calculations stemming from the peak area of each molecule during the method development study show little difference between extraction methods and analytical methodology. Chromatograms produced were filtered for m/z values ranging between 1017.97837 and 1302.32267, as per Table 2.2 allowing the peak area to be reliably determined, to calculate the BIT index (Table 3.1) and TEX$_{86}$ ratios and resultant SSTs (Table 3.2).

Table 3.1. A comparison of the BIT index values produced using the Soxhlet and microwave extraction methods, while comparing the short and long analytical methods. Those labelled as N/A were not analysed by LC-MS.

Sample Name	BIT Index			
	Soxhlet Extraction		Microwave Extraction	
	Short Method	Long Method	Short Method	Long Method
1H-02-A	0.102	0.100	0.100	0.098
1H-02-B	N/A	N/A	N/A	0.100
1H-04	0.095	N/A	0.089	0.086
2H-05	0.104	0.102	0.106	0.101
4H-07	0.106	0.094	0.102	0.094
5H-02	0.089	0.086	0.105	0.103

Table 3.2. A comparison of the TEX_{86}^{L} and SST values produced using the Soxhlet and microwave extraction methods and comparing the short and long analytical methods. Those marked with N/A were not extracted/analysed.

Sample Name	Soxhlet Extraction				Microwave Extraction			
	Short Method		Long Method		Short Method		Long Method	
	TEX_{86}^{L}	SST / °C	TEX_{86}^{L}	SST / °C	TEX_{86}^{L}	SST / °C	TEX_{86}^{L}	SST / °C
1H-02A	0.276	9.2	0.259	7.3	0.285	10.1	0.258	7.2
1H-02B	N/A	N/A	0.249	6.1	N/A	N/A	0.265	8.0
1H-04	0.283	9.9	N/A	N/A	0.280	9.6	0.251	6.4
2H-05	0.290	10.6	0.267	8.2	0.285	10.1	0.262	7.6
4H-07	0.290	10.6	N/A	N/A	0.283	9.9	N/A	N/A
5H-02	0.292	10.8	0.269	8.5	0.281	9.7	0.253	6.6

Each sample had a slightly decreased BIT ratio when the long analytical method was used. Percentage decreases for the analytical methods ranged from 1.92% for 5H-02 and 12.0% for 4H-07, though most were below 3%. Differences in extraction method provided less deviation than the analytical method, with the longer analytical method producing identical BIT index ratios for 4H-07. All values trended near 0, representing an open ocean environment with little terrestrial input which accurately depict the results expected from the full study.

The extraction methodology did not show a unanimous trend, values in general decreased marginally between SE and MAE, though both the short and long analytical method values showed an increase for 5H-02 (16.5%), the sediment with the greatest age of sedimentation. Lithology shifted at this depth to become more clay dominant and was found to have a notable gas presence (Takahashi *et al.*, 2011).

The isoGDGTs stood apart from the baseline and a complete series was found in all method development sediments used. Therefore, it was concluded there would be no issue with extracting GDGTs from sediments in the full study, regardless of the extraction method chosen.

Identified isoGDGTs were then used to calculate TEX_{86}^{L} (Equation 1.7) and resultant SSTs (Equation 1.8; Table 3.2). Differences were once again seen between extraction methods, and analytical methods used. The TEX_{86}^{L} values along with the subsequent SSTs show greater variation between the long and short methods, and extraction techniques. Small deviations in TEX_{86}^{L} led to greater differences in associated SSTs. Interlaboratory comparisons of BIT, and TEX_{86}-derived SSTs have been completed (Schouten *et al.*, 2009; 2013b), with

reproducibility reducing in variability from 3–4 to 1–3°C. The results obtained within this method development study showed deviation greater than the upper limit of Schouten *et al.* (2013b), and therefore the robustness and consistency of the temperature proxy measurements ought to be considered.

Schouten *et al.* (2013b) compiled replicate results from 35 laboratories, where both the extraction and analytical procedures are replicated, with differences across all methodology found to not have a large impact on GDGT distributions (Lengger *et al.*, 2012; Schouten *et al.*, 2007). The similarities between the BIT indices, provided evidence that the extraction method and analytical method had little impact on the ratio of GDGTs eluting. Yet, differences in SST cannot be overlooked, therefore reference materials shall be used in the full study, with results compared to previous analysis where true values were known.

MW extraction was chosen as the extraction method used for the full-scale study as greater numbers of samples could be extracted simultaneously, using less solvent. Compounds of interest were found to have eluted clearly from the baseline, with both extraction and analytical methods, particularly when used in SIM. Therefore, the short analytical method was combined with microwave extraction for the full study.

3.2   Quality control and data validity of full study

3.2.1 Reference Materials

The four reference materials (FV19, RCW26, EH8 and EH26) analysed alongside a marine standard and peat standard were subject to GDGT-based calculations. Two reference materials had been utilised in other studies (O'Connor *et al.*, 2023; Vickers *et al.*, 2020). The BIT index is listed (Table 3.3;

Hopmans *et al.*, 2004), and the percentage abundance of the three brGDGTs typically found to be most abundant, Ia, IIa and IIa, are shown in Figure 3.2.

Table 3.3. Relative abundances of three dominant brGDGTs for replicate standard runs. The BIT index, calculated according to Hopmans *et al.* (2004).

Standard ID	BIT Index		
	Run 1	Run 2	Average
FV19	0.993	0.993	0.993
RCW26	0.999	0.999	0.999
EH8	0.994	0.994	0.994
EH26	0.992	0.991	0.992
Marine Standard	0.115	0.140	0.127
Peat Standard	0.993	0.993	0.993

All six reference materials were analysed in duplicate by LC-MS, allowing for comment on consistency of the analytical method and manual integration methods adopted using Xcalibur software.
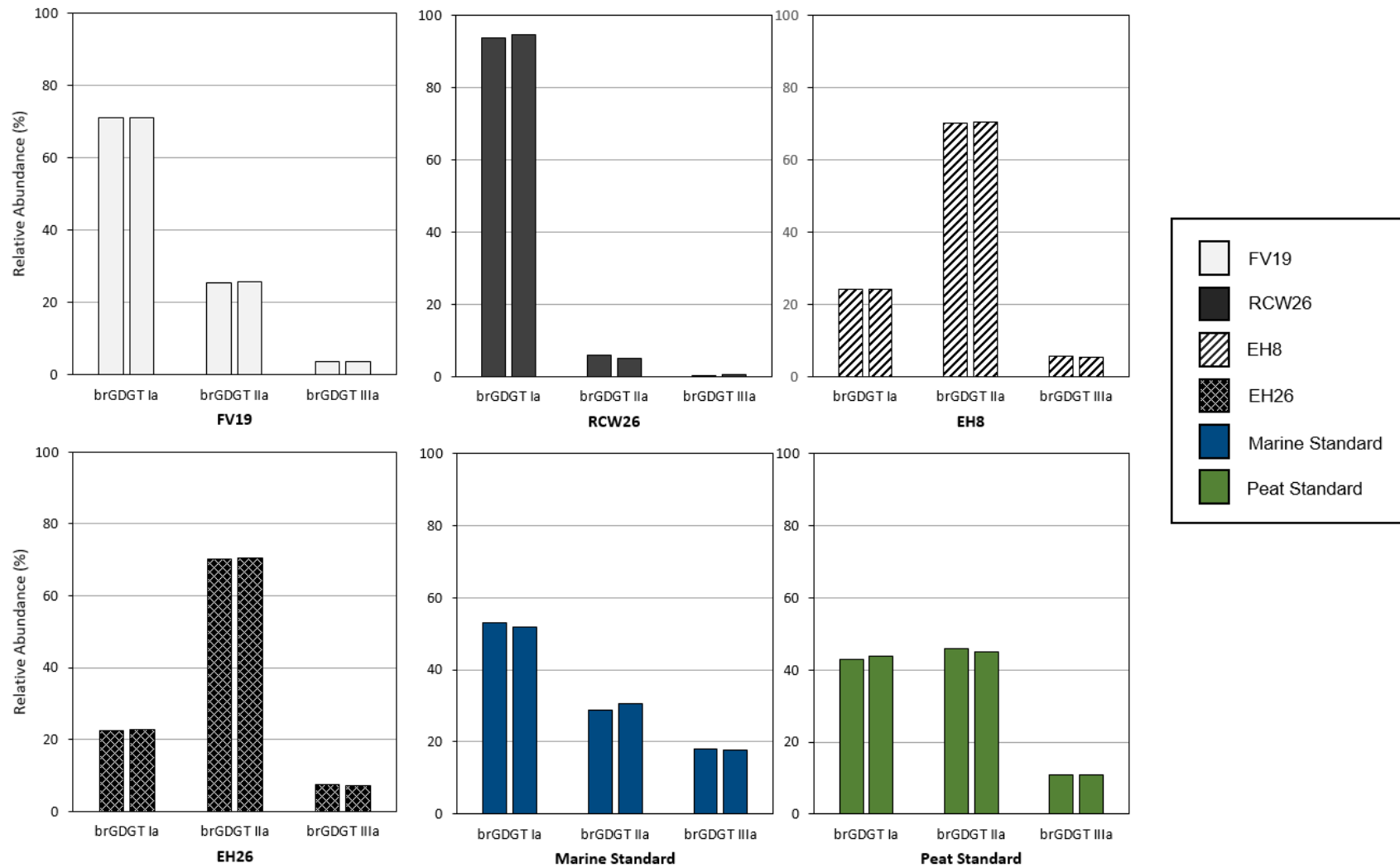
Figure 3.2. Relative abundance of three brGDGTs (Ia, IIa and IIIa) following duplicate analysis of six standards: FV19, RCW26, EH8, EH26, Marine Standard and Peat Standard.

Calculated BIT indices from the full study reference materials were compared to those in literature (RCW26, marine and peat standard; Table 3.4; O'Connor *et al.*, 2023; Vickers at al., 2020).

Table 3.4. Comparison of the in-house BIT and TEX$_{86}$ data for reference materials in literature.

Reference ID	BIT Index	Literature BIT Values	TEX$_{86}$	SST (°C)	Literature TEX$_{86}$ Values	SST (°C)	Comparison Reference
RCW26	0.999	0.999	0.706	28.4	*0.704	28.7	(O'Connor *et al.*, 2023)
	0.999	0.999	0.713	28.9	*0.710	28.3	
Marine Standard	0.115	0.106	0.528	16.6	0.554	18.2	(Vickers *et al.*, 2020)
	0.140	0.099	0.540	17.3	0.513	15.6	
Peat Standard	0.993	0.992	0.682	22.1	0.546	17.7	(Vickers *et al.*, 2020)
	0.993	0.990	0.520	16.0	0.547	17.8	

*Value calculated from raw data

Duplicate analysis for each reference material were conducted, with percentage abundances for each isoGDGT displayed in Table 3.5.

Table 3.5. Relative abundances (%) of isoGDGTs in reference materials.

Sample ID	GDGT-0	GDGT-1	GDGT-2	GDGT-3	Cren	Cren'
FV19_1	72.0	10.7	12.8	3.2	1.3	0.1
FV19_2	82.9	5.9	6.5	3.3	1.3	0.1
RCW26_1	61.7	11.1	13.6	13.1	0.5	<LOD
RCW26_2	64.9	9.9	13.1	11.5	0.6	<LOD
EH8_1	92.7	1.0	4.5	<LOD	1.8	<LOD
EH8_2	96.3	1.3	0.3	<LOD	2.1	<LOD
EH26_1	83.7	2.2	3.0	<LOD	3.0	<LOD
EH26_2	94.2	2.0	0.4	<LOD	3.3	<LOD
MarineSTD_1	36.0	2.5	2.1	0.4	58.7	0.3
MarineSTD_2	39.8	2.9	2.4	0.5	54.0	0.5
PeatSTD_1	71.8	7.1	14.0	1.1	6.0	0.1
PeatSTD_2	75.3	8.6	7.6	1.7	6.6	<LOD

<LOD signifies the molecule was below the limit of detection (LOD) during SIM

BIT indices (Table 3.3) were calculated as within 0.001 BIT units in all but one case, the marine standard. The chromatograms produced from LC-MS analysis of the marine standard displayed clear signs of degradation or contamination, with broad asymmetric compound peaks and a high background baseline. Variation of this standard was also seen in the BIT indices produced within the literature (0.106 and 0.099; Vickers *et al.*, 2020; Table 3.4). Comparisons of RCW26 and the peat standard, were also able to be made with published works (Table 3.4; O'Connor *et al.*, 2023; Vickers *et al.*, 2020), finding a maximum difference in BIT value of 0.003, well within the general reproducibility limits, of 0.410 (Schouten *et al.*, 2009) and 0.150 BIT units (Schouten *et al.*, 2013), found in the round-robin studies. The other reference materials used are omitted from Table 3.4 as they were compared to other analyses conducted internally, rather than published data.

The TEX_{86} values showed greater variation than the BIT indices. BIT values that are close to 0 or 1 are found to have better artificial reproducibility between laboratories (Schouten *et al.*, 2013), therefore an additional check using TEX_{86} values was explored. The round-robin study found TEX_{86} values to vary between 1.3 and 3.0 °C, when translated to temperature, in line with other palaeoceanographic temperature proxies (Schouten *et al.*, 2013). TEX_{86}-derived temperatures of the three comparable reference materials show deviations in line with the round-robin study, except for one analysis of the peat standard (Schouten *et al.*, 2013), producing the maximum deviation stated (>6 °C), though TEX_{86}-derived SSTs are not appropriate for peat settings.

By conducting duplicate analysis of all reference materials, it allowed repeatability to be briefly assessed. Relative abundances of the reference material isoGDGTs (Table 3.5) showed variances between duplicate runs for individual compounds.

The LODs were determined through the analysis (mean + 2 SD) of three hexane:IPA blanks in SIM. The marine standard is theorised to be the most relevant reference material when assessing isoGDGTs, as it is the only reference material that derives from a marine setting and overall abundances of isoGDGTs were much greater in the marine standard, opposed to all other reference materials. The resultant abundance ratios, when inputted into TEX_{86}^{L} and SST equations produce temperatures that differ by only 0.7 °C (16.6 and 17.3 °C; Table 3.4).

3.2.2 Replicate sample analysis

Differences were seen in isoGDGTs distributions from the relative abundances in reference materials. The three dominant brGDGTs, Ia, IIa and IIIa, were also seen to vary in relative abundance in U1343 sediment extracts, though to a lesser extent, yet the overall BIT index varies little with 0.069, 0.069 and 0.070 found respectively (Table 3.6).

Table 3.6. Relative abundances, BIT index, and relative standard deviation (RSD) of the three abundant brGDGTs, Ia, IIa and IIIa, for the triplicate analysis of a MIS3 sample, aged 48.1 kya.

Sample ID	Relative abundance (%)			BIT Index
	brGDGT-Ia	brGDGT-IIa	brGDGT-IIIa	
MIS 3	38.1	37.5	24.4	0.069
ID: 22	38.6	36.2	25.2	0.069
~ 48.1 kya	39.6	35.1	25.3	0.070
RSD (%)	1.97	3.42	1.98	0.32

The repeatability of the analytical method was assessed through calculation of the relative standard deviation (RSD) of triplicate analyses of three samples from MIS 1, 3 and 5, according to the age model of Asahi *et al.* (2016; Table 3.7).

Table 3.7. Relative abundances and relative standard deviations (%) of isoGDGTs in replicate sample data. Age determined from an existing age model (Asahi *et al.*, 2016).

Sample ID	Age / kya	GDGT-0	GDGT-1	GDGT-2	GDGT-3	Cren	Cren'
2		44	3.3	1.6	0.3	50.4	0.7
2A		45.0	3.2	1.5	0.3	49.3	0.7
2B	10.23	45.4	3.2	1.5	0.3	49.0	0.7
Average		44.7	3.2	1.5	0.3	49.6	0.7
RSD (%)		1.58	1.78	3.84	0.04	1.50	0.02
22		47.9	3.4	1.5	0.3	46.3	0.6
22A		49.2	3.2	1.4	0.2	45.4	0.6
22B	48.07	48.8	3.3	1.6	0.2	45.5	0.6
Average		48.6	3.3	1.5	0.2	45.7	0.6
RSD (%)		1.37	3.02	6.66	11.95	1.13	0.68
49		51.2	4.2	2.1	0.2	41.5	0.7
49A		51.7	4.4	1.7	0.2	41.4	0.7
49B	95.71	51.6	4.4	1.7	0.2	41.4	0.7
Average		51.5	4.3	1.8	0.2	41.4	0.7
RSD (%)		0.46	2.29	12.7	15.0	0.16	5.64

Peak areas taken from chromatograms were used for other paleoenvironmental reconstruction calculations, with TEX_{86}^{L} ratios (Table 3.8) and resultant SSTs (Table 3.9) calculated for those extracts analysed in triplicate.

Table 3.8. The TEX_{86}^{L} ratio produced using GDGT ratios for replicate sample analyses, showing good repeatability.

Sample ID	Replicate 1	Replicate 2	Replicate 3	Average	Standard Deviation	RSD (%)
2	0.30	0.30	0.31	0.30	0.0034	1.1
22	0.29	0.29	0.31	0.30	0.0083	2.8
49	0.32	0.27	0.27	0.29	0.025	8.6

Table 3.9. Sea surface temperatures produced for replicate sample analysis using the TEX^L_{86} ratios listed in Table 3.8.

Sample ID	Replicate 1	Replicate 2	Replicate 3	Average	Standard Deviation	RSD
	°C	°C	°C	°C	°C	%
2	12.0	11.4	12.2	11.9	0.333	2.80
22	10.6	10.9	12.4	11.3	0.812	7.18
49	13.7	8.53	8.51	10.3	2.46	23.9

Three U1343 sediment polar extracts, aged approximately 10.2, 48.1 and 95.7 kya, were run in triplicate on the LC-MS to further check the repeatability of the analytical procedure. The three most abundant brGDGTs, Ia, IIa and IIIa were used to assess repeatability. The MIS 3 extract, aged at approximately 48.1 kya, had the greatest variation with relative standard deviations of 1.97%, 3.42% and 1.98%, for Ia, IIa and IIIa, respectively (Table 3.6).

The BIT index values were also indicative of good replication, with replicate values of 0.069, 0.069 and 0.070 (ID No: 22, aged ~48.1 kya; Table 3.6). The BIT indices for the two other samples were also consistent, with the sample from MIS 1 (ID No: 2; aged ~10.2 kya) ranging between 0.079 and 0.082. The replicate from MIS 5 (ID No: 49; aged ~95.7 kya), had BIT index values ranging between 0.246 and 0.252, also showing good repeatability as per the repeatability limit of 0.046 of the round-robin study (Schouten *et al.*, 2013).

Two filter blanks and three procedural blanks were also analysed alongside the samples to check for contamination throughout the extraction and filtration processes. Only one procedural blank contained peaks visible above the baseline, prior to SIM, once isolated a low response was shown for brGDGT-Ia and GDGT-0, but no other GDGTs were detected.

Replicate sample analysis, Table 3.7, showed greater repeatability than the reference materials. RSD values were typically found to be low and therefore, the SSTs produced from the ratios were also concordant. The TEX_{86}^L ratio and resultant SSTs are shown in Table 3.8 and Table 3.9. The calculated RSD values showed a correlation between sample age/depth and variation that ought to be explored.

Confidence in the analytical technique used for the GDGT analysis can be taken due to the good replication of results when analysed multiple times, combined with the reproducibility of the reference materials used across multiple studies (O'Connor *et al.*, 2023; Vickers *et al.*, 2020).

3.3   Full Study Results

The full GDGT exploration study at Site U1343 used relative abundances of both isoGDGT and brGDGT molecules to give an overall impression as to the paleoclimate and paleoenvironment at the time of deposition within MIS 1 to 6.

3.3.1 GDGT distributions across MIS 1 through 6

The relative abundance of isoGDGTs were assessed across MIS 1 to 6 (Figure 3.3), with average values showing the greatest proportion of GDGT-0 found in MIS 3, and largest crenarchaeol abundances in MIS 5. These abundances for each time-point were also plotted in a ternary diagram (Figure 3.4), against total brGDGT abundance. This ratio, in most cases, were reflective of a marine environment, though were not strongly indicative of either an open marine, or coastal marine setting and therefore this alone cannot be used to conclusively suggest what the environment was like across any of the six MIS assessed.
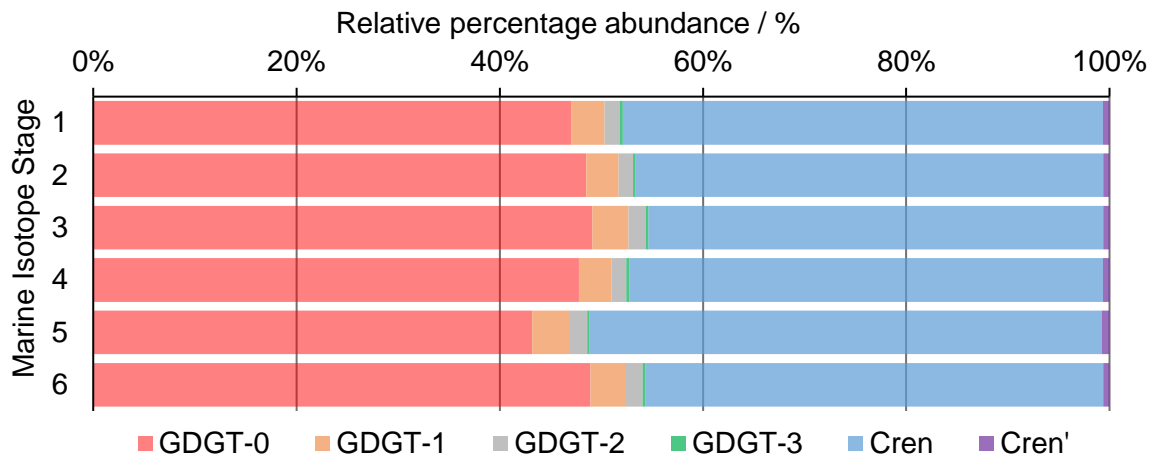
Figure 3.3. Relative percentage abundance of each isoGDGTs averaged for each marine isotope stage.
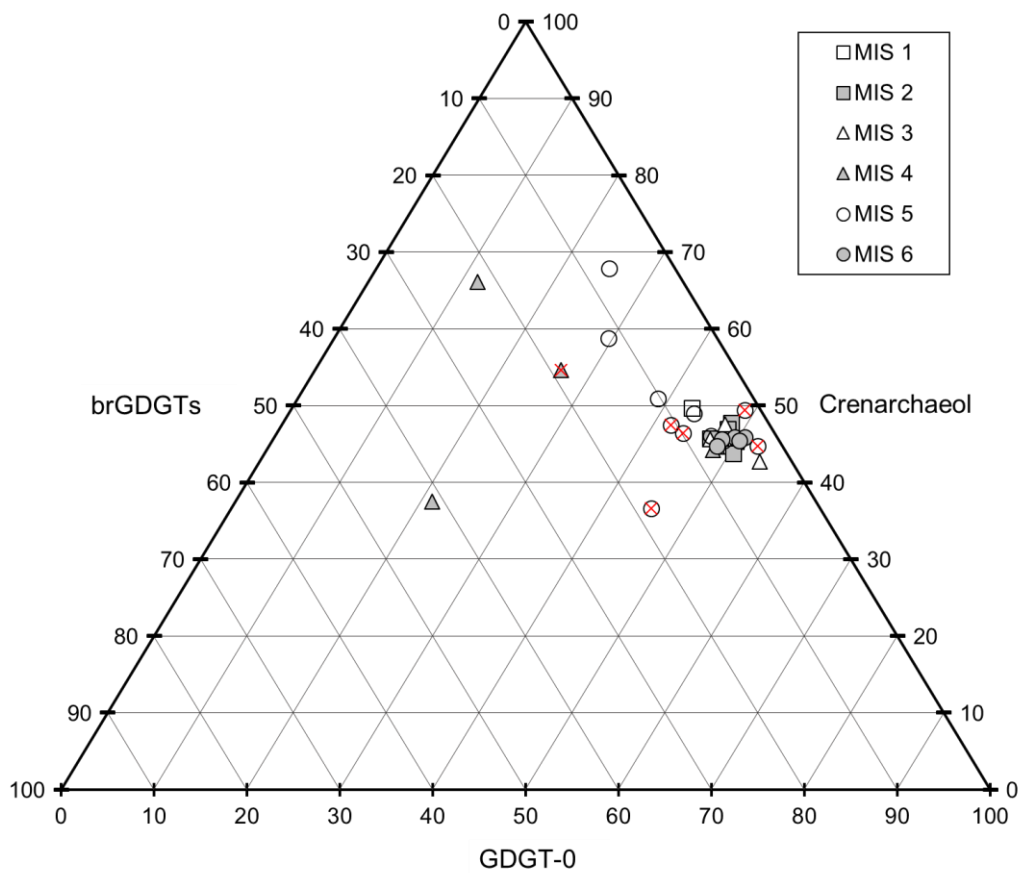
Figure 3.4. Ternary diagram revealing distribution of GDGT-0, crenarchaeol and the sum of branched GDGTs extracted from U1343 sediments used within this study across marine isotope stages 1 to 6. Symbols containing a red cross were not found to contain all pentamethylated (IIa, IIb and IIc) and hexamethylated brGDGT (IIIa, IIIb and IIIc).

The abundances of brGDGTs, GDGT-0 and crenarchaeol were not the only structures to vary in abundance through time. Figure 3.5 depicts example chromatograms from each MIS, showing the elution of the isoGDGTs and brGDGTs. The relative abundances show variation in peak height, and the associated peak areas used for calculations, including TEX$_{86}$ and the BIT index, were also affected.
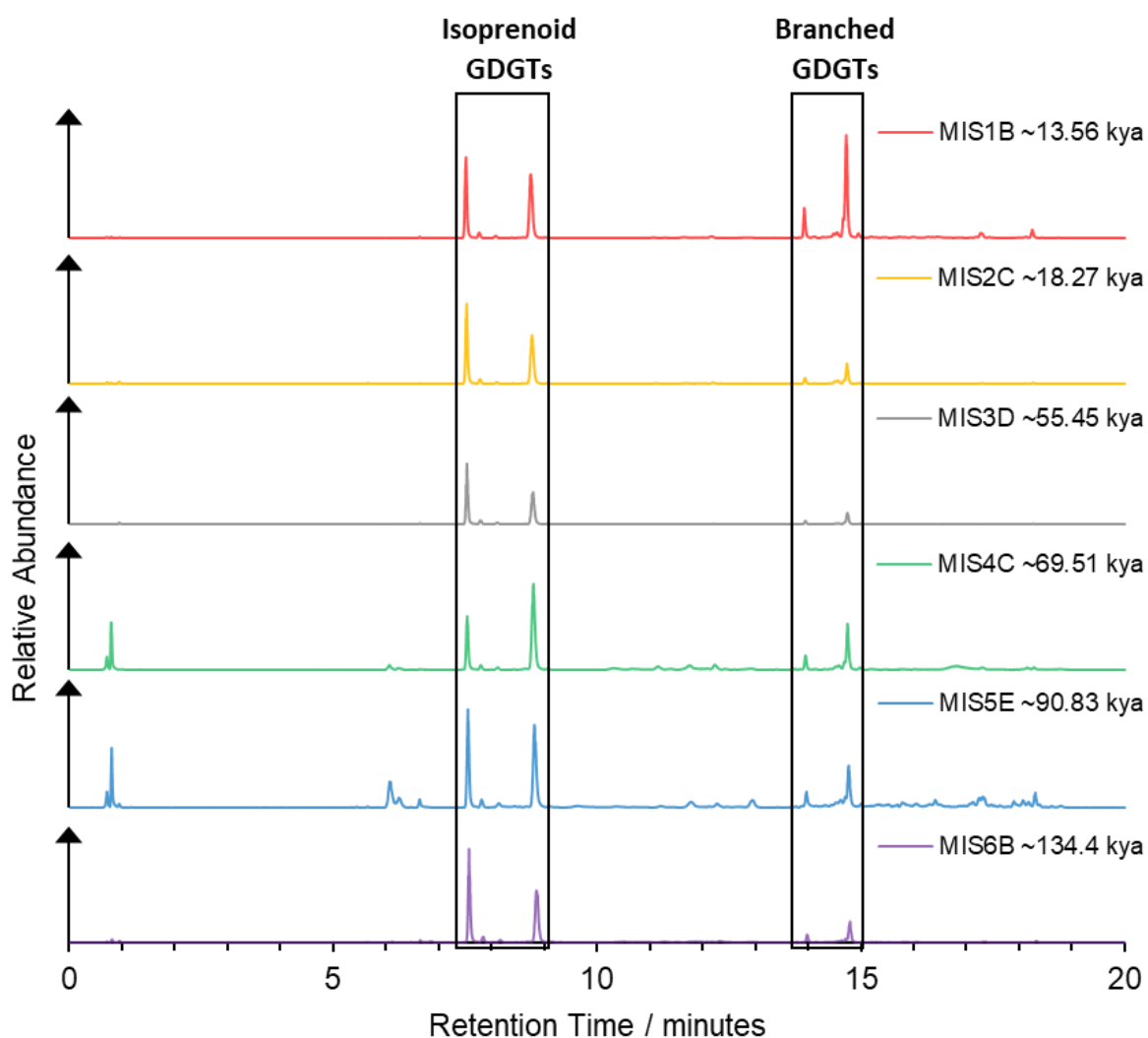
Figure 3.5. Chromatograms representing each marine isotope stage, 1 through 6 (red through purple), small deviations in peak height and area can be inferred between stages.

The full study involved the analysis, by LC-MS, of 30 polar extracts of U1343 sediments. Site U1343 is proximal to the boundary of the modern-day sea ice

extent (Stabeno *et al*, 2012), and was a place covered by sea-ice during the LGM (Takahashi *et al.*, 2007). Sediments across 160 kya are therefore likely to contain varying contributions of isoGDGTs and brGDGTs, and have different sources, of different origin (e.g. marine or terrestrial). The distributions, and thus origins, ought to be considered. There are differences in isoGDGT abundances across MIS 1 to 6 occur, (Figure 3.3), where GDGT-0 proportions decrease by approximately 5%, alongside a concurrent increase in crenarchaeol (> 7%).

As with Schouten *et al.* (2013; Figure 1.8), the relative distributions of brGDGTs, GDGT-0 and crenarchaeol can be plotted on a ternary diagram to give an indication as to the environment at the time of sedimentation. High proportions of GDGT-0 and crenarchaeol, with approximately 5% brGDGTs are typical of an open marine environment. A slight increase in brGDGTs, between 5-20%, alongside a drop in crenarchaeol indicate a coastal marine environment, while high brGDGT contributions are much more indicative of soils and lacustrine settings.

The brGDGTs, GDGT-0 and crenarchaeol relative abundances of U1343 sediment extracts were found to be largely indicative of a marine setting, due to the high GDGT-0 and crenarchaeol contribution, approximately 45% for each (Figure 3.4). Sediments dominated by crenarchaeol, as is the case with U1343, suggest Thaumarchaeota are a substantial source of the GDGTs (Schouten *et al.*, 2013). Likewise, low brGDGT abundances indicate little allochthonous and in situ production contributions, further evidencing high archaeal contributions.

This typical marine presentation is not reflective of all study data. Figure 3.4 shows several points that present more closely with coastal marine, or lacustrine environment. Sediments surrounding the MIS 5 to 4 transition in particular show deviation from the general trend, as do those with an incomplete

brGDGT sequence, marked with a red cross. However, this did not always decrease the overall brGDGT abundance, conversely it more often presented as an increase in relative abundance. Concurrent decreases in GDGT-0, and increases in crenarchaeol, are seen (Figure 3.3) indicating even greater Thaumarchaeota contribution and abundance but also an increase in methanogenic Euryarchaeota (Blaga *et al.*, 2009).

The abundances of brGDGTs, GDGT-0 and crenarchaeol were not the only GDGT compounds to vary in abundance across MIS. Figure 3.5 depicts example chromatograms from each MIS, showing the elution of the isoGDGTs, between 7 and 9 minutes, and brGDGTs, between 13 and 15 minutes. The relative abundances of all GDGTs show variation across the MIS in peak height, and the associated peak areas used for calculations, including TEX_{86}, were also affected.

The isoGDGT distributions across 160 kya were dominated by GDGT-0 and crenarchaeol (Figure 3.3), where the percentage abundances are averaged for each MIS; there are smaller contributions of GDGT-1, GDGT-2, GDGT-3 and cren'. Crenarchaeol abundance is highest during MIS 5, where a concurrent decrease in GDGT-0 is seen. Ratios of isoGDGTs can give an indication to the origin and were considered at site U1343 in terms of methanogenic and deep-water contributions.

Environmental parameters were also reconstructed through calculation of TEX_{86}, SSTs and combined with brGDGTs to give an indication to the OM contribution from a terrestrial source, via the BIT index.

3.3.2. BIT and TEX$_{86}$-derived temperatures

The BIT index represents the abundance of terrestrial OM, with higher values suggesting a greater terrestrial input. Therefore, high BIT values, greater than 0.3, produce SSTs that are unreliable as a larger proportion of GDGT distribution is from an alternative source. BIT index values (Figure 3.6) were calculated to assess both where terrestrial input was higher, and to suggest reliability of the TEX$_{86}$ temperatures. Two values were greater than 0.3, on the transition between MIS 5 and 4, and once value within MIS 5, aged approximately 95.7 kya.
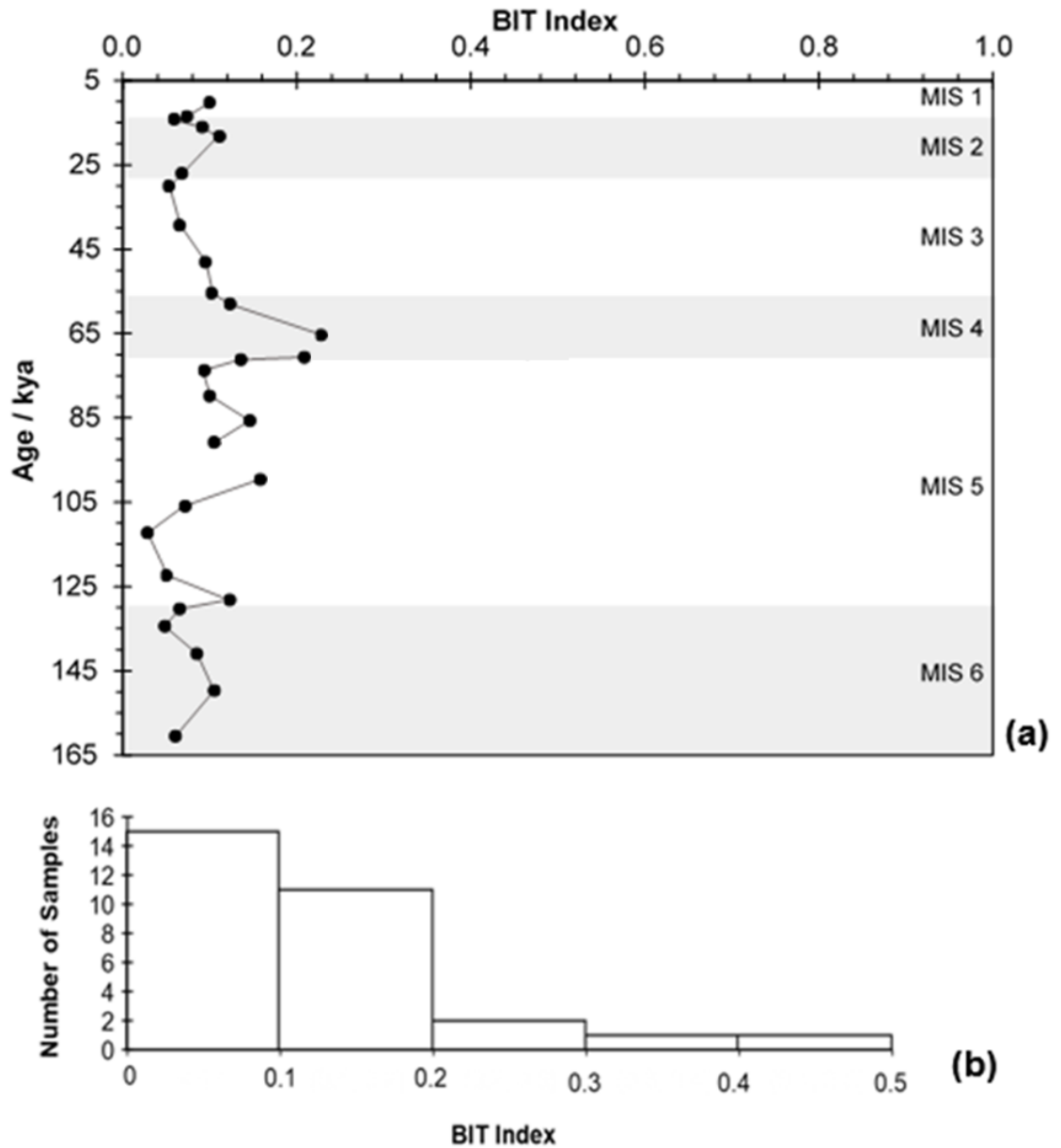
Figure 3.6. BIT values from U1343 as found in this study, across MIS (a).
Those with BIT values above 0.3 BIT units are omitted from graph. The BIT
index distribution across the 160 kya investigated are shown in (b), including
two values above 0.3.

Temperature reconstructions were completed at all age-depth points, including
the two that had high BIT values (Figure 3.7), using four different SST
reconstructions using TEX_{86} and its reciprocal form ($1/TEX_{86}$), and TEX_{86}^{L}. The
reconstructed temperatures appear to peak on the transition between MIS 4

and within MIS 5. These temperatures are offset from the time-points where

high BIT values were produced, as indicated on Figure 3.7.
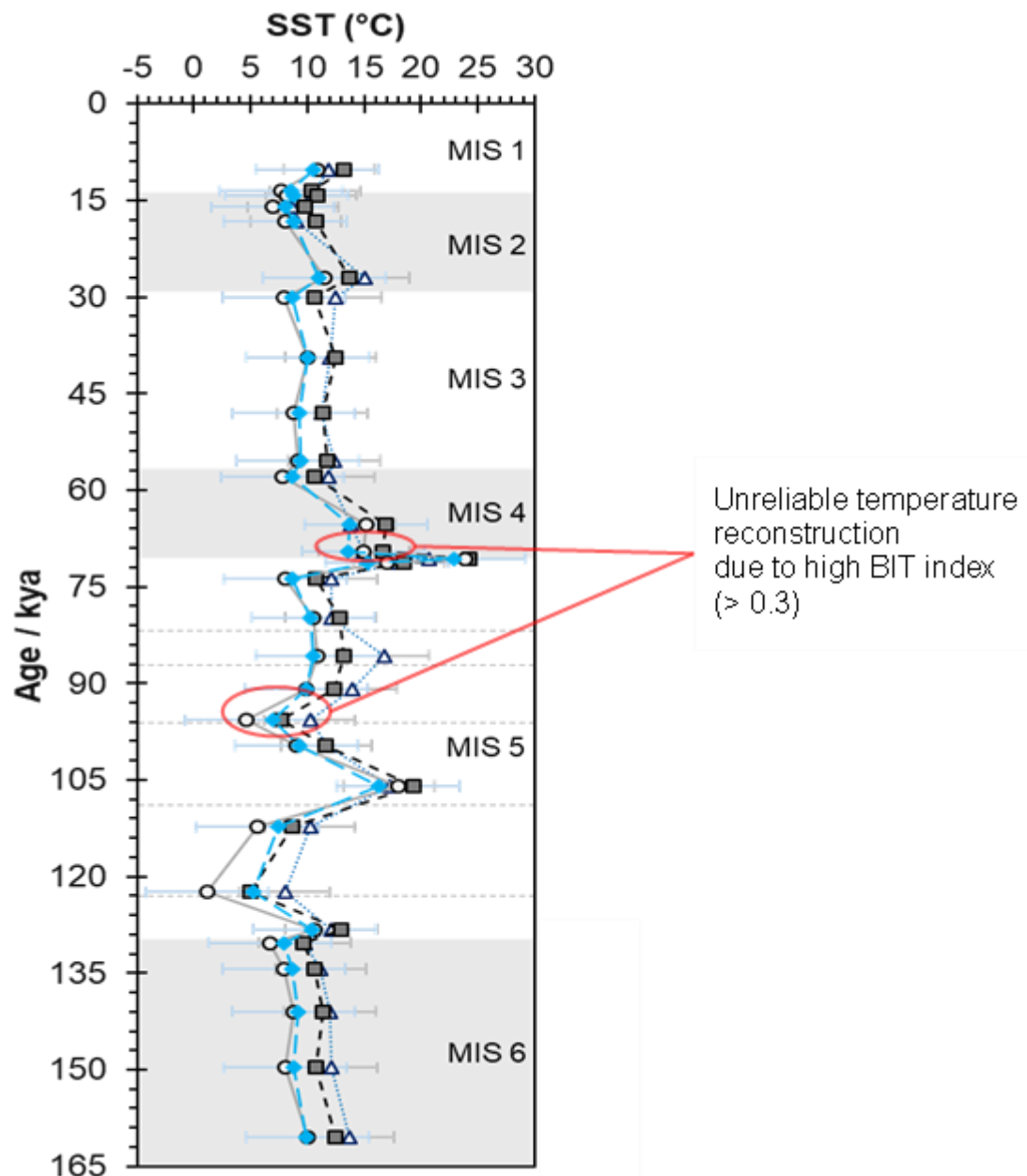
Figure 3.7. Sea surface temperatures produced from this study of site U1343

using four variations of TEX$_{86}$ calibrations. The linear TEX$_{86}^{L}$ sea surface

temperature proposed by Kim *et al.* (2015; blue triangles), the linear TEX$_{86}$

equation by Schouten *et al.* (2002; blue diamonds) and the non-linear

relationships proposed by Liu *et al.* (2009; black squares) and Kim *et al.* (2010;

navy circles).

With isoGDGT ratios being representative of their origin and environment it is important to consider where they were synthesised. High quantities of terrestrially-derived isoGDGTs lead to the production of unreliable TEX_{86}-based SSTs. Two high BIT indices, larger than 0.3, were produced at time points within this study, and therefore produce non-linear temperatures (Weijers *et al.*, 2006; Sluijs *et al.*, 2020). The BIT indices were explored to assess both the origin of isoGDGTs and to assess the validity of the TEX_{86}-derived SSTs produced at U1343.

During interglacial periods U1343 was likely characterised as an open marine environment, which was indicated by BIT values closer to zero. Input from glacial landmasses during a glacial MIS could have caused an increase in BIT value. All BIT values from U1343 sediments were found to be below 0.5 (Figure 3.6), but two points were above 0.3, making any sea temperatures produced from the GDGT abundances unreliable. The U1343 BIT values were calculated using the De Jong *et al.* (2015) calibration, values across MIS 1 through 6, as well as the overall distribution across the 160 kya (Figure 3.6).

There were minor differences in BIT indices across the MIS, with the largest values being found during MIS 4 indicating either a greater terrestrial contribution or an increase in the in-situ production in the water column. MIS 4 was a time of extensive glaciation, with the northern ice sheers playing a dominant role in global ice volume (Doughty *et al.*, 2021). All other MIS have averages below 0.1 BIT units, reaffirming the belief of a more open marine environment.

The BIT indices produced from this study, support the production of SSTs using TEX_{86} as the majority are below 0.3 BIT units.

The concentrations of GDGT-1, GDGT-2 and GDGT-3 were found in much lower abundances than GDGT-0 and crenarchaeol, which was to be expected due to U1343 being situated in a low temperature, high latitude marine environment.

Four TEX_{86} calibrations were used within this study to reconstruct SSTs as TEX_{86} calibrations have been found to spatially vary across different oceanic basins and environments (Tierney & Tingley, 2015; Ho *et al.*, 2014). Furthermore, at the low temperature end of TEX_{86} calibrations, additional non-temperature related factors have been found to influence distributions (Kim *et al.*, 2010; Ho *et al.*, 2014).

The original calibration (Schouten *et al.*, 2002; Equations 1.4 and 1.5), the TEX_{86}^{L} index (Equations 1.7 and 1.8; Kim *et al.*, 2015), and two non-linear relationships, using the reciprocal form of TEX_{86} (1/TEX_{86}), from Liu *et al.* (2009; Equation 2.1) and Kim *et al.* (2010; Equation 2.2), although the latter has a weaker correlation with temperature. The SSTs produced using the four SST calibrations are shown in Figure 3.7. The TEX_{86}-derived SSTs across MIS 1 to 6 varied between 1.24 and 24.3 °C, depending on the proxy used, with both temperatures having been reconstructed within MIS 5, one on the transition into MIS 4.

The residual standard error associated with TEX_{86} calibrations is large. For example, the non-linear calibration from Kim *et al.* (2010) has an error of ±5.4 °C and the TEX_{86}^{L} calibration has an uncertainty of ±4 °C (error bars present in Figure 3.7). The round-robin studies show less variation, between 1 – 3 °C (Schouten *et al.*, 2013b).

Temperatures were found to be highest on the transition of MIS 5 to 4 and at ~109 kya, during MIS 5. MIS 5 appears to demonstrate the stadial-interstadial cycling characteristic of the MIS (Table 3.10). Whereby temperatures are expected to peak at approximately 87 kya and 109 kya, and be lowest at 82, 96 and 123 kya (Asahi *et al.*, 2016; Lisiecki & Raymo, 2005).

Table 3.10. Age of sediments at which the sub-stages within marine isotope stage 5 peaked according to Asahi *et al.* (2016).

MIS 5 sub-stage	Age (at peak; kya)	Stadial/Interstadial
5a	82	Stadial
5b	87	Interstadial
5c	96	Stadial
5d	109	Interstadial
5e	123	Stadial

Two time points were found to have increased BIT values, above the 0.3 threshold, suggesting the data is unreliable and therefore should not be considered accurate.

SSTs are likely to not map the stadial-interstadial cycle exactly, owing to the lag between atmospheric temperature changes and oceanic ones. Additional paleotemperature proxies could be used to further evidence SSTs at U1343 across the 160 kya time period studied. Sub-surface and deeper water temperatures can also influence TEX_{86}-derived SSTs, creating additional deviation from true values.

The trends seen in the SSTs produced do align with the trends expected to see, particularly within MIS 5, which contains smaller cycling between colder and warmer climates.

3.3.3. Origin indicators for GDGTs at Site U1343

3.3.3.1 Methanogens and methanotrophic contributions

The isoGDGTs did not originate from methanogens or anaerobic methanotrophic sources (Figure 3.8), as methane index values were all found to be below 0.5. Other indicators of methanogenic archaeal contributions, the GDGT-0/creanarchaeol ratio and %GDGT-0, were found to be below the relevant thresholds of 2 and 67% respectively.
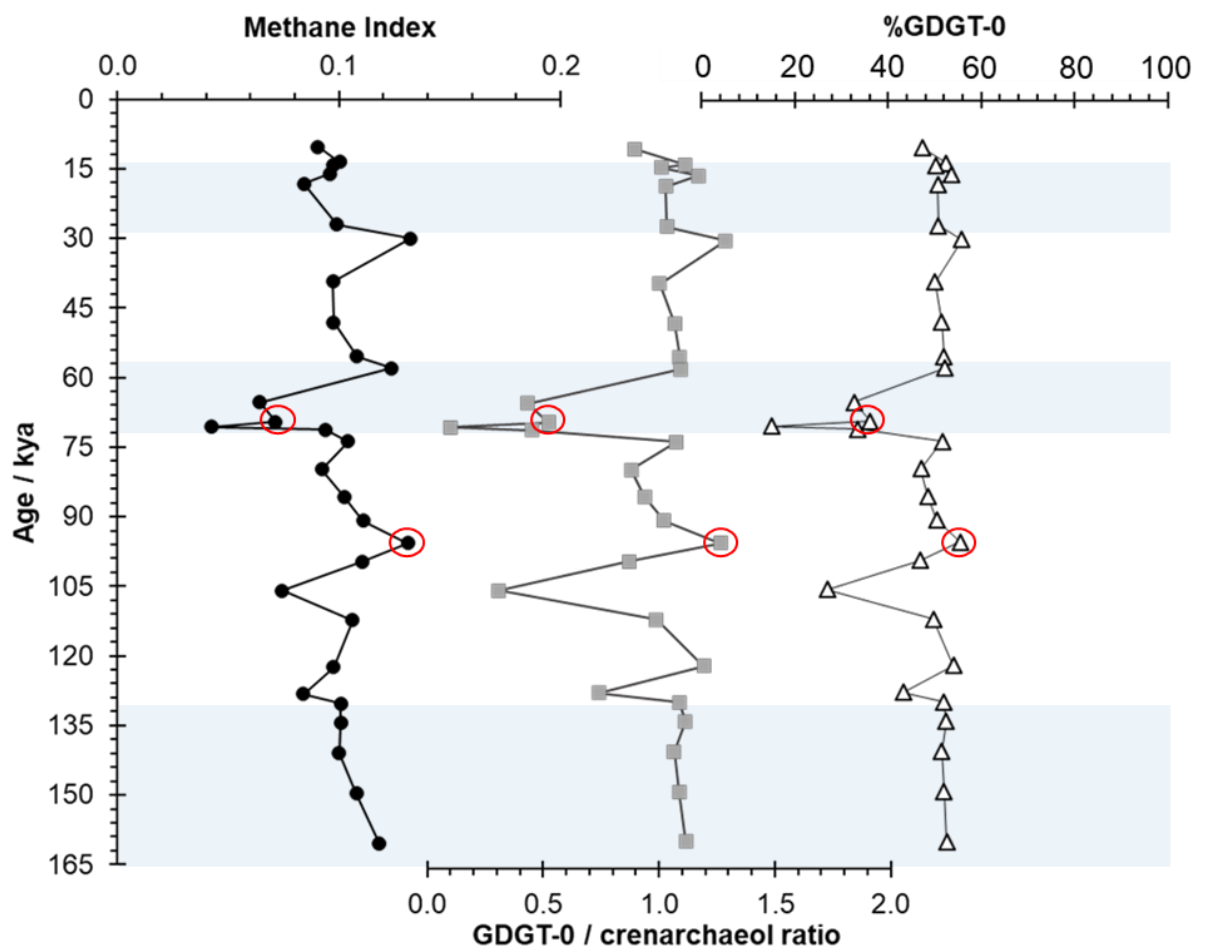
Figure 3.8. Visual representation of the anaerobic methanotrophic contribution to isoGDGTs (methane index; black filled circles; Pancost *et al.*, 2001), the methanogenic contribution of isoGDGTs (grey squares; Blaga *et al.*, 2009) and

the %GDGT-0 (Sinninghe Damsté *et al.*, 2012) at each test location (black lined triangles). Data points with high BIT indices circled in red.

There is no indication of high methanogenic archaea contributions across the time series analysed (Figure 3.8). No MI values evaluated were found to have values approaching or over 2. Likewise, no %GDGT-0 values were found to be greater than 67% indicating no methanogenic archaea, as values for U1343 span 15% to 54%. The GDGT-0/crenarchaeol ratio and the MI are both strongly influenced by the cren contribution; this deviation in relative crenarchaeol abundance was also seen in SST reconstructions in the BIT indices (Figure 3.6) and SSTs (Figure 3.7).

3.3.3.2 Deep water contribution

Instead, the deep-water contribution was considered owing to the difference of water depth profiles within the Bering Sea. The main source of isoGDGTs was found to be from the ammonium oxidising Thaumarcheota, which produce GDGTs within the water column at U1343, as GDGT-2/GDGT-3 ratio values were found to be predominantly greater than 5 across the six MIS studied (Figure 3.9).
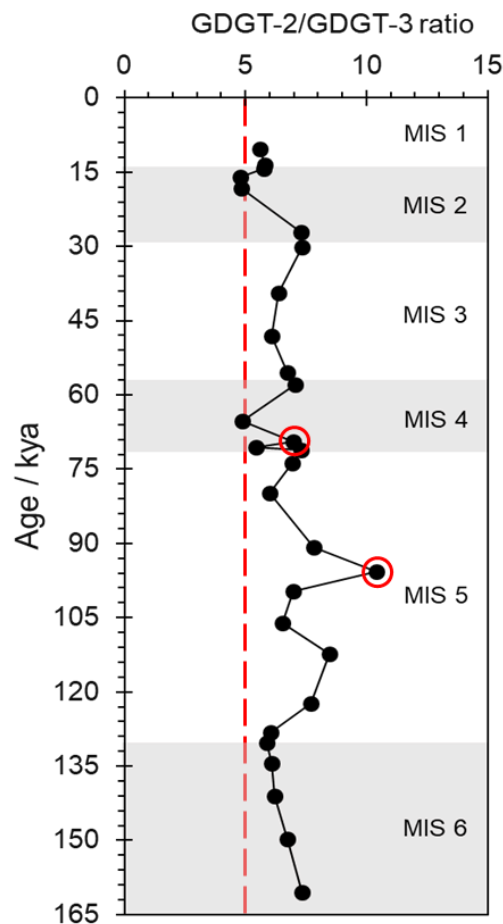
Figure 3.9. GDGT-2/GDGT-3 ratio across marine isotope stages 1 through 6, indicating high isoGDGTs contributions from deep water archaea. The points in red circles correspond to high BIT value data points. Values greater than 5 are indicative of high deep-water GDGT production.

This study found GDGT-2/GDGT-3 ratios between 4.81 and 10.4 suggesting high isoGDGT contributions from deep water archaea. The data point with the highest GDGT-2/GDGT-3 ratio was also found to produce an inaccurate SST due to a high BIT value. Generally, increases in GDGT-2/GDGT-3 ratios would be expected to create a cold bias within TEX$_{86}$ calibrations (Sluijs *et al.*, 2020), yet this is not fully visible in the SSTs obtained. Some of the lowest reconstructed temperatures (Figure 3.7), were seen in MIS 5, at the same time GDGT-2/GDGT-3 ratios increased. Yet this pattern was not seen throughout all the time-points. Therefore, it is not possible to definitively conclude whether

there was a large input of isoGDGTs from deep water archaea, even with such high productivity in the region.

The BIT index suggested there is little terrestrial OM contribution; the MI, %GDGT-0 and GDGT-0/crenarchaeol calculations imply little methanotrophic and methanogenic archaeal contribution. As the GDGT-2/GDGT-3 ratio implies high *in situ* deep-water production of GDGTs. Therefore, the reconstructed SSTs (Figure 3.7) are likely to reflect the temperature below the surface, or at a greater depth within the water column.

3.3.3.3   Ring Index

The trends between the ring index (Equation 1.25) and other parameters from this study are graphically displayed in Figure 3.10, with GDGT-0/crenarchaeol showing the strongest correlation (r^2 = 0.999, n = 30). Lower RI values correspond to high GDGT-0/crenarchaeol ratios. The RI also correlates strongly with other parameters, including TEX_{86}, SST and RI_{TEX}, the quadratic regression formed from Zhang *et al.* (2016; Equation 1.26). Where correlations were found to be r^2 = 0.854, r^2 = 0.915, r^2 = 0.942, respectively.
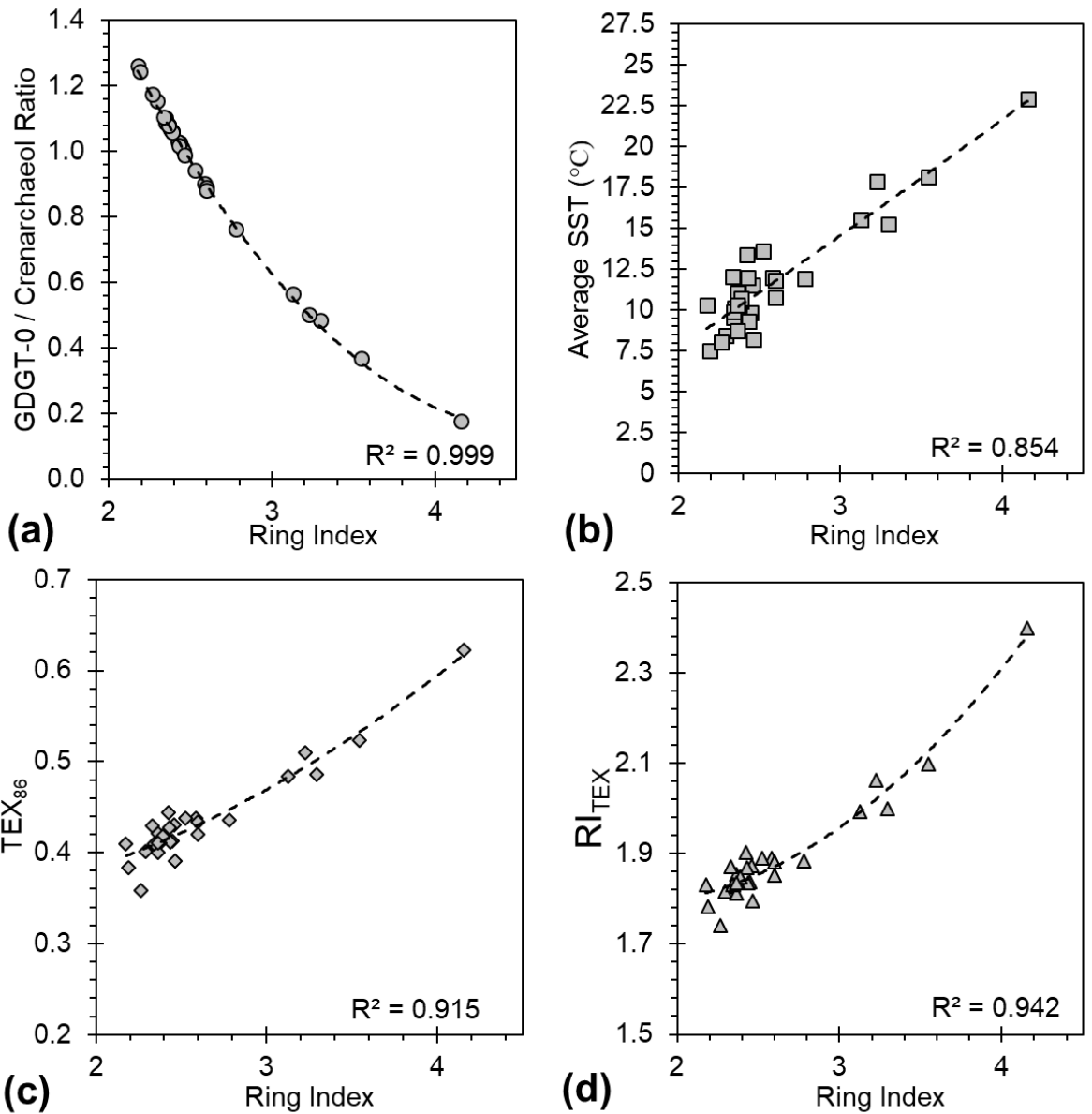
Figure 3.10. Correlations within this study between (a) ring index and GDGT/crenarchaeol ratio, (b) ring index and average SST, (c) between ring index and TEX_{86}, and (d) the RI_{TEX}-RI relationship.

All residual ring index ($|\Delta RI|$) values were found to be above 0.3 (Figure 3.11), indicating non-temperature factors influenced the GDGT populations within the water column at Site U1343. These values were found to be most extreme within MIS 4.
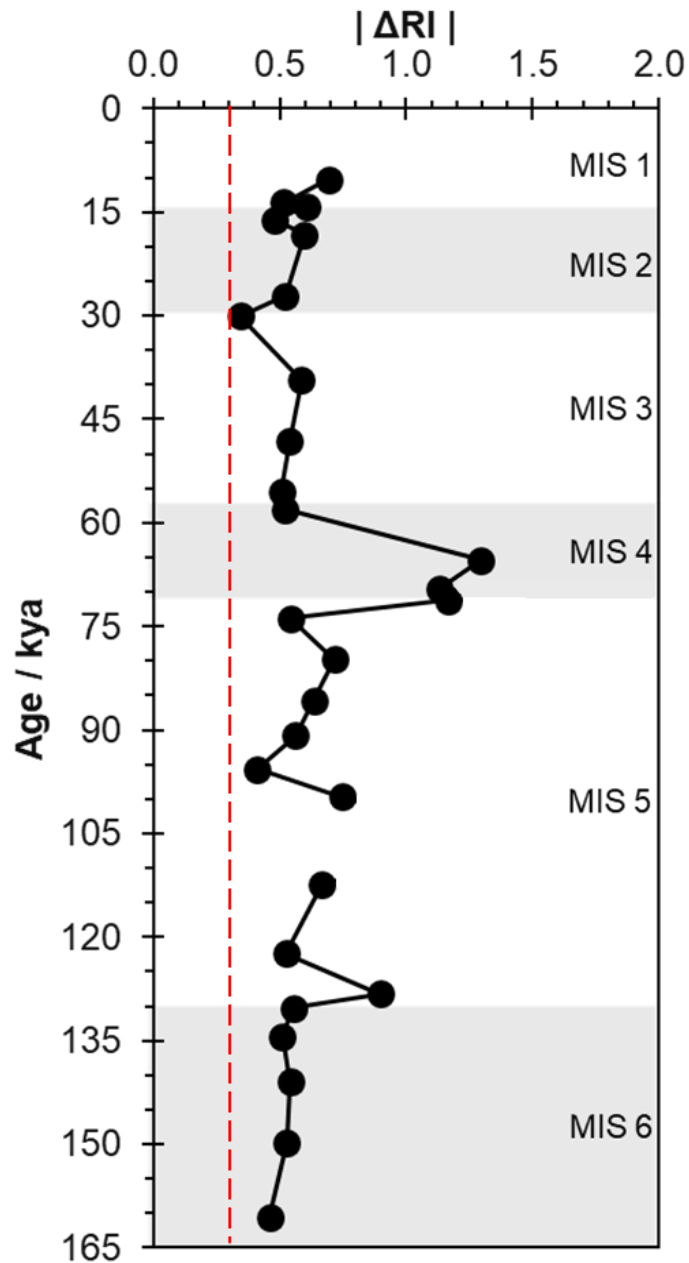
Figure 3.11. |ΔRI| values for U1343 extracts spanning MIS 1 through 6.

Importantly, the RI-TEX$_{86}$ relationships were not found to be sensitive to changes in archaeal community structure, seasonality, transportation or depth profile and therefore can be appropriately used in most settings, if the GDGTs are still dominated by temperature variations (Zhang *et al.*, 2016).

3.3.4 MBT and CBT calculations from U1343 sediments

The MBT'5$_{Me}$ ratios are plotted alongside resultant MATs (Figure 3.12) calculated using the peat calibration of Naafs *et al.* (2017b; Equation 2.3) and the soil calibrations of Naafs *et al.* (2017a; Equation 2.4; grey) and De Jonge *et al.* (2014; Equation 2.5; blue). Sediments with an incomplete GDGT set were omitted from Figure 3.12. CBT-derived pH values of U1343 from this study using calibrations from Naafs *et al.* (2017a; 2017b) and De Jonge *et al.* (2014) are in Figure 3.13.
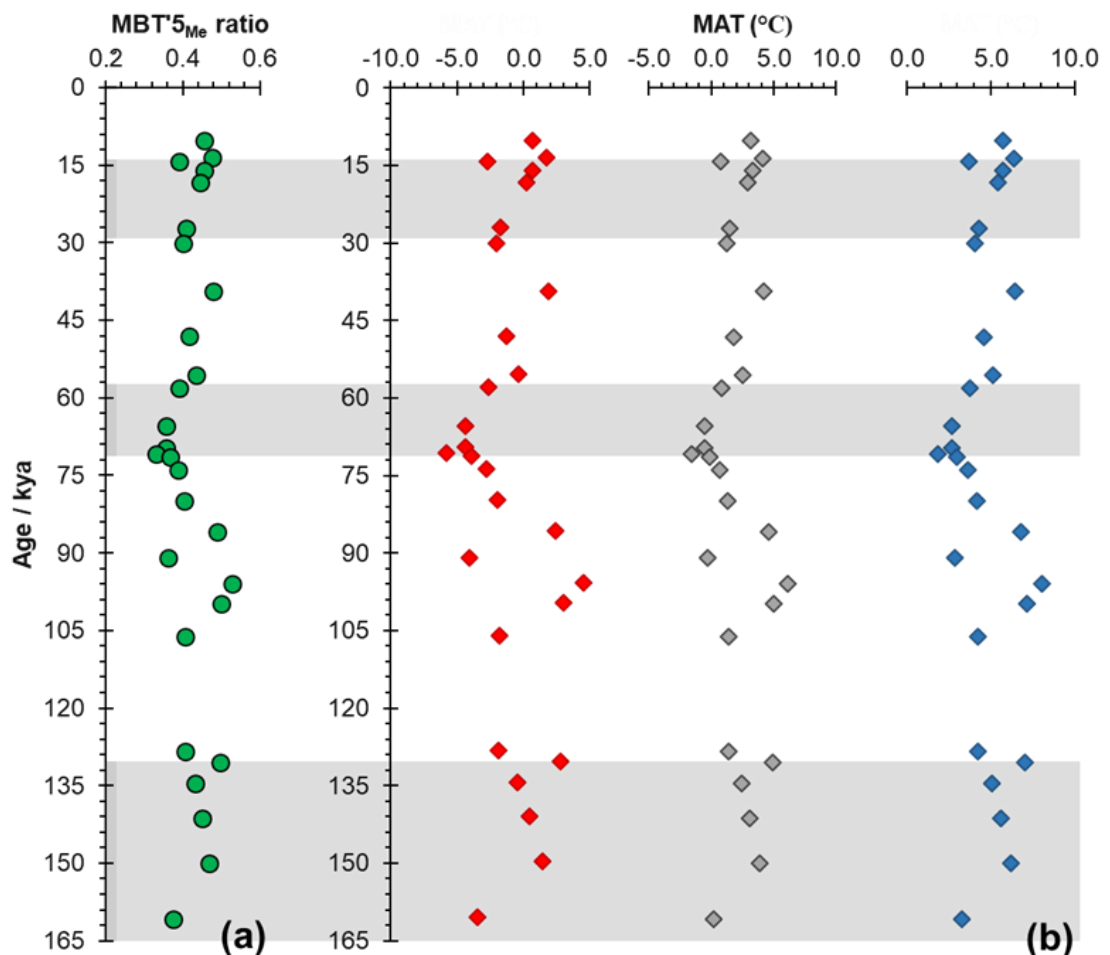
Figure 3.12. (a) MBT ratios produced using MBT'5$_{Me}$, for site U1343 (b) resultant MATs using the peat calibration from Naafs *et al.* (2017b; red), MAT using the soil calibrations from Naafs *et al.* (2017a; grey) and from De Jonge *et al.* (2014; blue).
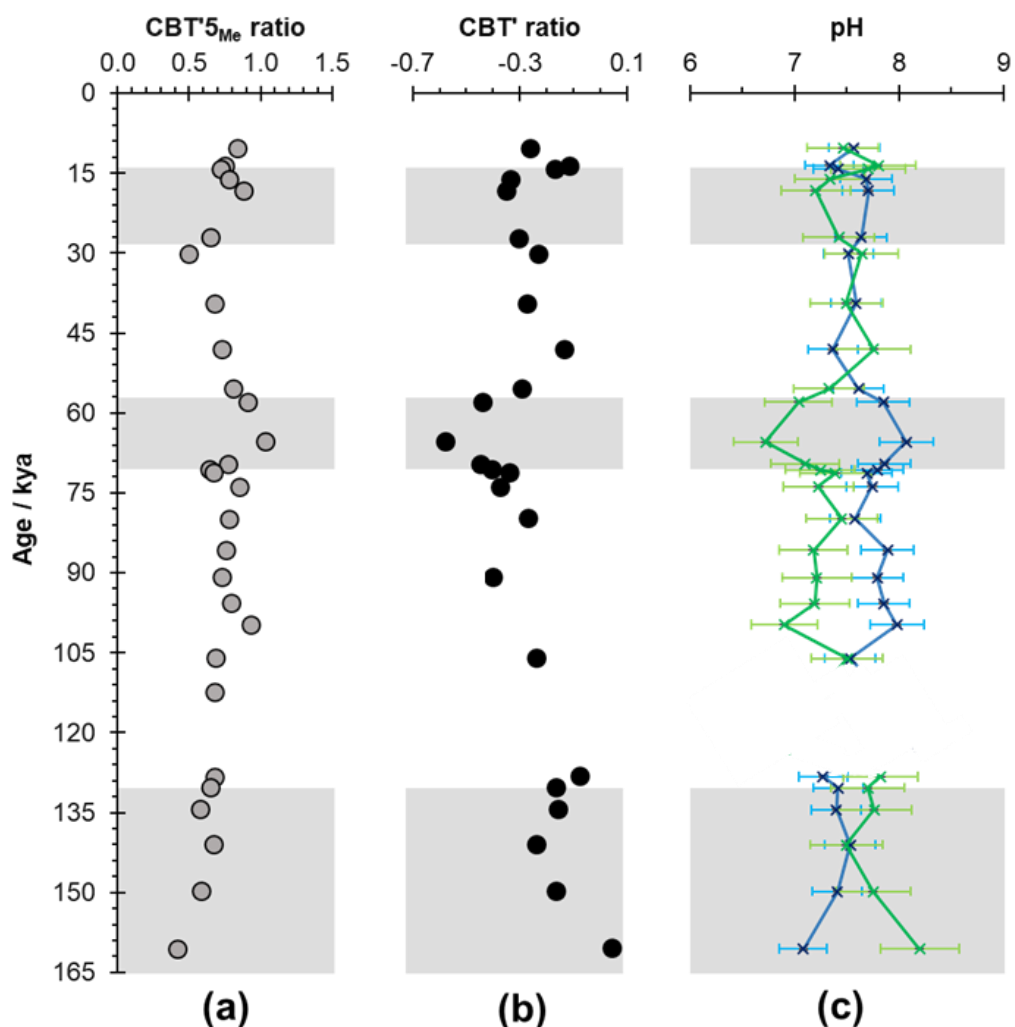
Figure 3.13. CBT values for site U1343 using (a) CBT'5$_{Me}$ and (b) CBT'. The resultant pH using CBT' calibration from De Jonge *et al.* (2014; blue) and CBT$_{Peat}$ calibration from Naafs *et al.* (2017b; green).

GDGT-based indices using brGDGTs include the BIT index (Hopmans *et al.*, 2004), the cyclisation ratio, and the MBT (Figure 3.13) and CBT indices (Figure 3.14) used as paleotemperature proxies (Weijers *et al.*, 2007). Mean air temperature records have been produced for a variety of marine environments, including those from high-latitudes (Weijers *et al.* 2007b; Sangiorgi *et al.*, 2018; Dearing Crampton-Flood *et al.*, 2021). The MBT, CBT, cyclisation ratio and MBT/CBT indices were calculated using brGDGT ratios at U1343.

Two sediments from MIS 5 (approximate sediment ages 112.3 and 122.4 kya) were found to have an incomplete GDGT series for the brGDGT-based calculations, therefore they have been omitted from the MBT and CBT data analysis (Figures 3.12 and 3.13). The methylation index, MBT'5$_{Me}$ (Equation 1.19), was used (De Jonge *et al.*, 2014), producing ratio ranges of 0.32 and 0.51. MIS 4 produced the lowest average ratio. Each MBT'5$_{Me}$ value is plotted against age of sediments in Figure 3.12 alongside MAT calculations using calibrations that use MBT'5$_{Me}$ ratios (Naafs *et al.*, 2017b; 2017a; De Jonge *et al.*, 2014), Equations 2.3, 3.4 and 2.5, respectively.

The brGDGTs distributions have produced varied MATs, with the lowest temperatures being present on the transition between MIS 5 and MIS 4. The warmest reconstructed temperatures were found in MIS 5. There is a loose trend across the MIS, with odd MIS depicting warmer temperatures than the even MIS. This trend is to be expected, given the G-IG cycling present across MIS 1 to 6. The MAT$_{Peat}$ calibration (Naafs *et al.*, 2017b) produced the coolest temperatures, with temperatures commonly being less than 0 °C. The MAT$_{soil}$ equations produced temperatures typically greater than 0 °C, with the calibration from De Jonge *et al.* (2014) consistently showing temperatures greater than 2 °C warmer. Given both the location of U1343, and Beringia being an ecoregion mostly covered in wetlands (Bartlein *et al.*, 2015), the calibration of Naafs *et al.* (2017b) is likely to map most closely to atmospheric temperatures on the land masses at time of production.

The pH of U1343 sediments was determined through analysis of the GDGT molecule ratios owing to the relationship between cyclisation of brGDGTs and pH (Figure 3.13).

Ratios of brGDGTs were used to calculate CBT' and thus pH using the calibrations of De Jonge *et al.* (2014; Equations 1.20 and 2.7), and additionally using the CBTPeat calibration proposed by Naafs *et al.* (2017a; Equation 2.6) and successive pH calculation of Naafs *et al.* (2017b; Equation 2.8). Values across both calibrations were generally found to be near neutral, trending to a slightly more basic pH, with values produced being between 6.7 and 8.2. The CBT' values ranged between -0.60 and 0.042, resulting in a CBT'-based pH estimate ranging between 7.1 and 8.1, with an average across the six MIS of 7.6 ± 0.2 (or 3.2% RSD). CBT_{Peat}-based pH estimates had slightly increased variation, spanning 6.7 to 8.2, with an average across the six MIS of 7.4 ± 0.3 (4.6% RSD).

3.4 Overall reconstruction of Site U1343

A compilation of the GDGT-derived reconstructions is displayed in Figure 3.14 and are plotted alongside the benthic $\delta^{18}O$ data of U1343 (Asahi *et al.*, 2016; Worne *et al.*, 2019) and global $\delta^{13}C$ CH_4 isotope data (Möller *et al.*, 2013; Fischer *et al.*, 2008).
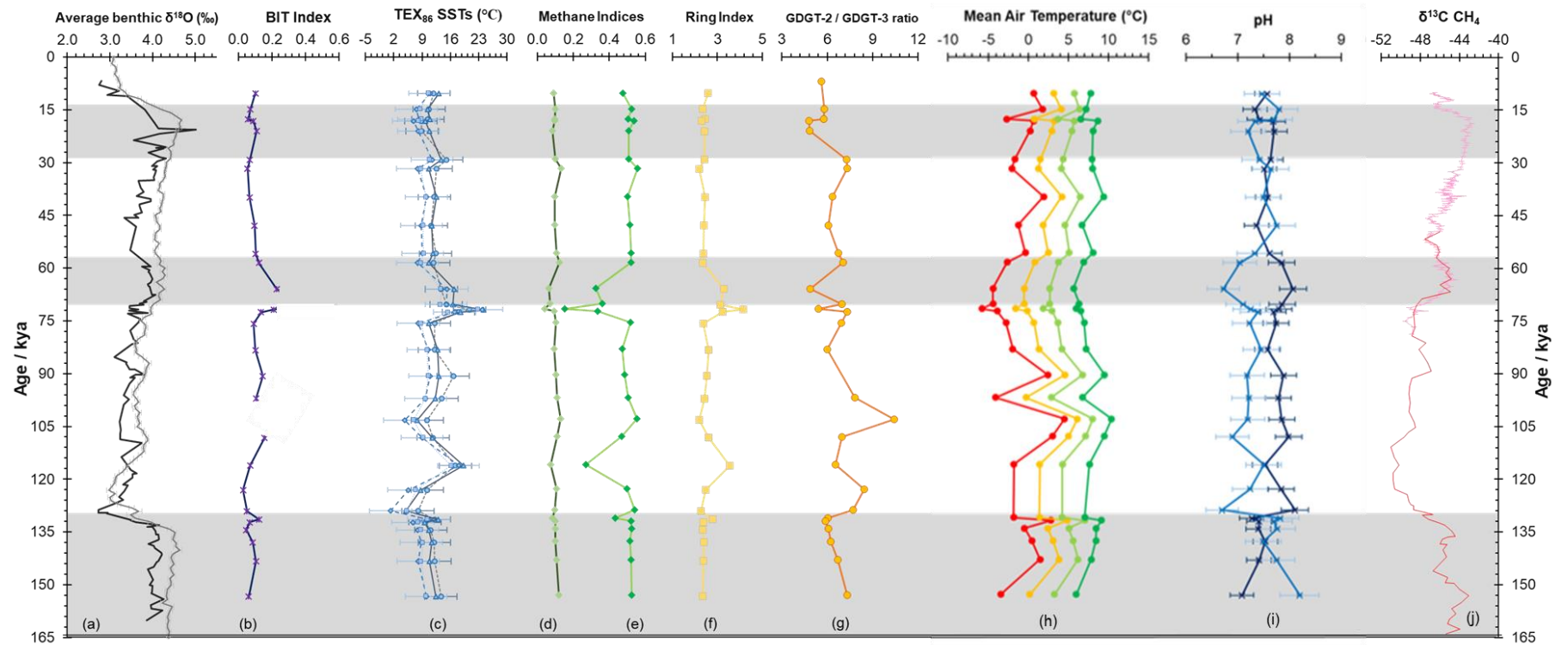
Figure 3.14. Compilation ofGDGTs-derived results from study of U1343. Benthic δ^{18}O data (a) from Worne *et al.* (2019) and Asahi *et al.* (2016) and Lisiecki & Raymo (2005). The BIT index (b), TEX[86]-derived SSTs (c), MI (d), %GDGT-0 (e), RI (f) and GDGT-2/GDGT-3 ratio (g) from U1343 data obtained in this study; MAT reconstructions (h) of U1343 were performed using the calibrations of Naafs *et al.* (2017b; red), Naafs *et al.* (2017a; orange), De Jonge *et al.* (2014; light green) and Peterse *et al.* (2012; dark green). The pH reconstructions (i) from Naafs *et al.* (2017b; light blue) and De Jonge *et al.* (2014; dark blue); the δ^{13}C CH[4] isotope data (j) from Möller *et al.* (2013; red) and Fischer *et al.* (2008; pink) are also shown.

The benthic $\delta^{18}O$ data for site U1343 (Asahi *et al.*, 2016; Worne *et al.*, 2019), shows highest values during the glacial MIS 2, and the minimum values within MIS 5, close to the transition from MIS 6. The benthic $\delta^{18}O$ value, and LGM, peaked in MIS 2 at ca. 20 kya ago. Reconstructions from this study show MATs decrease following the benthic $\delta^{18}O$ peak having remained relatively steady through MIS 4 and 3; the BIT index reconstructions at Site U1343 were seen to concurrently decrease toward very low values. The $\delta^{13}C$ CH_4 data by Fisher *et al.* (2008) show a negative CIE trend occurring from the LGM toward present day.

The $\delta^{13}C$ CH_4 trends of Fischer *et al.* (2008) and Möller *et al.* (2013) became less negative, suggesting atmospheric carbon was being successfully locked up. Temperatures within MIS 5 were found to be the most varied; there are substages within MIS 5, where stadials alternate with interstadial periods, wherein the benthic $\delta^{18}O$ averages peaked within the Lisiecki & Raymo (2005) model (Table 3.10).

The cooler MATs within MIS 5 track well with the sub-stages, particularly within MIS 5c, 5d and 5e. The greatest increase in BIT index within MIS 5 coincided with the warmest reconstructed MATs. This trend, however, was not seen in the reconstructed SSTs, instead a slight decrease occurred (Figure 3.14). In future, it would be of benefit to age the sediments used. At present, sediments were aged based on low resolution studies (Asahi *et al.*, 2016; Worne *et al.* 2019), using linear sedimentation rates between aged depth points.

Generally, the variations in SSTs did not coincide with the changes in MAT. There were two 'warm' periods within the SST reconstruction, found within MIS 5, and on the cusp of the transition into MIS 4. At ca. 115.6 and 71.4 kya, SSTs were highest, but the methane indicators showed decreases (Figure 3.14). The

RI ratios across the MIS followed the same trends as SSTs, with peaks occurring simultaneously with the highest SSTs. Two data points analysed, at ca. 95.71 kya and ca. 69.59 kya are largely discounted from discussion as these points produced BIT indices exceeding the threshold of 0.3, which led to unreliable calculation of other proxies including SSTs owing to the likely increase of terrestrial OM.

All origin indicators from this study imply that isoGDGTs were primarily produced deep in the water column, but additional factors other than temperature had an impact on the distribution of isoGDGTs produced, such as ammonium and oxygen concentrations during the growth phase (Elling *et al.*, 2014; Qin *et al.*, 2014) or salinity. The BIT indices were generally found to be below 0.3, suggesting that any fluvial input of terrestrially derived isoGDGTs is negligible (Dauner *et al.*, 2021), and instead GDGT distributions are characteristic of marine settings. Indicators of methanogenic or methanotrophic contributions all proved to be insignificant in magnitude, with MI, GDGT-0/crenarchaeol and %GDGT-0 all found to be below the relevant thresholds for these sources. The RI shows strong correlation with several other parameters, Figure 3.10, indicating no obvious outliers, suggesting the interpretation of the GDGT ratios was successful, and errors lie with the calibrations themselves rather than any interpretation errors. Quality control also corroborated this, as replicate analysis and reference materials produced concordant results.

The |ΔRI| values were found to be greater than 0.3 in all cases, which suggests a large contribution of archaeal groups outside of the Thaumarchaeota contributions (Dauner *et al.*, 2021), increasing the unreliability of SSTs produced. Instead, reconstructed temperatures are more likely to be

representative of the sub-surface, or deep water in the region, yet may not be linearly calibrated owing to impact of the non-temperature related influences.

High GDGT-2/GDGT-3 ratios were found across MIS 1 to 6, with the larger ratio values found in MIS 5, suggesting the production of isoGDGTs occurred substantially in deep waters (Taylor *et al.*, 2013), over 1000 m in depth, a possibility given the location of U1343, as the Bering Sea contains several water depth profiles and substantial water circulation within the gyre (Stabeno *et al.*, 1999). Caution should be taken to the validity of the SSTs produced, due to the high-latitude location where isoGDGT distributions often produce TEX_{86} values that do not fit linearly with the global averages (Kim *et al.*, 2010). The temperatures reconstructed, if linear with any of the four global calibrations used, are still likely to have produced unreliable SSTs, due to the origin of the GDGTs being primarily from either the sub-surface or deep waters within the water column. The general trends, however, are more reliable as multiple core-top reconstructions show the same trends. This is also true of the reconstructed MATs.

Chapter 4: Conclusions and Future Work

4.1 Conclusions

GDGTs were successfully extracted from IODP Expedition 323 site U1343 sediments and the distributions analysed by LC-MS, in order to reconstruct a palaeo SST record of the Bering Sea across a time period of approximately 160 kya, which includes the lead up to the LGM. Other environmental parameters were also reconstructed, including MAT and pH, where GDGT distributions allowed.

A small method development study was conducted to compare the SE and MAE methods, as well as two LC-MS analytical methods (Figure 3.1). Signals produced from MAE were lower than that of SE but were still found to be above the detection limit. Each GDGT was identified through isolation of each mass-to-charge ratio, SIM, from Table 2.2, and the peak areas were used to determine the BIT index (Table 3.1) and TEX_{86}-based SSTs (Table 3.2) for all methods. The BIT indices showed little deviation across different analytical and extraction methods, the long LC-MS method produced BIT values slightly below those of the short method. The TEX_{86} values had greater variation, though the difference between extraction methods was not significant. The similarities between the BIT indices indicated little difference between the ratios of molecules obtained and therefore MAE was chosen for the full study as multiple samples could be extracted simultaneously while utilising less solvent. Time constraints on the instrumentation, also limited the analytical time, therefore the short method was chosen.

To ensure results from the full study were acceptable, four reference materials alongside a marine standard and peat standard, were analysed in duplicate.

Percentage abundances of the three most abundant brGDGTs were determined, alongside the BIT index, for the reference materials, with all results found to be concordant. The greatest variation was seen in the marine standard, which appeared to have degraded as replicate values showed large variation. This had also been seen in the analysis by Vickers *et al.* (202). Three samples were analysed in triplicate, across MIS 2, MIS 4 and MIS 6 where relative standard deviations varied between 0.16% and 15.0% and appeared to increase with sediment age.

The isoGDGT distributions across approximately 160 kya were dominated by GDGT-0 and crenarchaeol, with a much smaller contribution of brGDGTs, which is typical of an open marine environment. A couple of extracts from MIS 4, had GDGT distributions more typical of a coastal marine or lacustrine system, but these sediments were also found to have an incomplete set of brGDGTs, often missing IIIb and IIIc, skewing calculations.

Four calibrations derived from TEX_{86} ratios were used to reconstruct SSTs (Figure 3.7; Schouten *et al.*, 2002; Liu *et al.*, 2009; Kim *et al.*, 2010; 2015). The $1/TEX_{86}$ calibration from Kim *et al.* (2010) produced the lowest SST of 1.24 °C on the transition between MIS 6 and 5. The highest reconstructed temperature of 24.3 °C was found using the calibration of Liu *et al.* (2009) on the transition to MIS 4. During glacial periods (MIS 2, 4 and 6), SSTs gradually got cooler over time. The interglacial periods appeared more variable, though this does display as expected within MIS 5. Uncertainties associated with the reconstructed temperatures could be up to 5.4 °C (Kim et al., 2010), therefore additional proxy investigations should be conducted to increase reliability of the data.

Consideration was given to the origins of the GDGTs that had been retained at Site U1343. The BIT index was calculated to determine terrestrial OM

contribution; values were found to be low (below 0.3) in all but two cases. Therefore, generally, the terrestrial contribution was seen to be negligible, as was the methanotrophic and methanogenic archaeal contribution. All methane indicators, the MI, GDGT-0/crenarchaeol ratio and %GDGT-0, were found to be below their relevant thresholds (Figure 3.8). Deep water contributions are indicated by GDGT-2/GDGT-3 ratios and were found to be extensive in almost all cases (Figure 3.9). The RI values were also extremely high, greater than 2, and indicate non-thermal influences of the GDGT distributions, although a specific source is not well defined (Dauner *et al.*, 2021).

The brGDGTs not only considered the terrestrial input, but were used to reconstruct atmospheric MAT, through MBT'5$_{Me}$ and CBT' using multiple calibrations (De Jonge *et al.*, 2014; Naafs *et al.*, 2017a; 2017b). The MATs tracked well with the G-IG periods across the MIS, including the stadial-interstadial cycling within MIS 5. Three calibrations were used to reconstruct MAT (De Jonge *et al.*, 2014; Naafs *et al.*, 2017a; 2017b). Reconstructed MATs appeared to vary less than the SSTs. Temperatures varied from -5.8 to 4.5 °C using the peat calibration (Naafs *et al.*, 2017b; Equation 2.3). CBT ratios were used for pH determination, with reconstructions producing pH values between 6.7 and 8.2 (Figure 3.13; De Jonge *et al.*,2014; Naafs *et al.*, 2017).

Additional proxies could be used to verify the validity of the data produced within this study, including palynology, or other biomarkers such as alkenones.

4.2 Future Work

The sediments from site U1343 were not accurately dated within this study. A more accurate age-model would allow the MIS boundaries to be reliably and accurately inferred. Instead, age approximations were based on analysis

undertaken by Asahi *et al.* (2016) and Worne *et al.* (2019), wherein low-resolution studies of ages were assumed based on linear sedimentation rates between data points. This would provide benefit for determining the MIS transitions more accurately.

Forty-five other polar lipid extracts were produced within this study, but are yet to be analysed by LC-MS, owing to instrumentation time-limitations. An increased resolution record would be created from the analysis of the extracts.

The reconstructed temperatures could be used alongside numerous other proxies, including alkenones, to increase reliability of the SSTs, by creating a multi-proxy approach, an alkenone standard would need to be analysed by GC-MS, and previously analysed GC-MS data interpreted. The calibration $U_{37}^{K'}$ has limitations at high-latitudes, due to low abundances (Schlung *et al*, 2013), and anomalously high abundances of the C_{37} tetra-unsaturated methyl alkenone (%$C_{37:4}$), making SST values produced unreliable (Wang *et al*., 2021). However, used in combination with TEX_{86} could reinforce trends, or temperatures, that have been reconstructed from Site U1343 within this study.

Alternatively, other proxies could be utilised to create a more detailed overview of the environment going into and coming out of the LGM. Few paleoclimate investigations fully consider the impact of methane on climate, particularly the fractions locked up in permafrost or peatlands. It is crucial to assess the impact of CH_4 on climate change, as it has 25 times the global warming potential of CO_2 (Bridgham *et al*., 2013). Atmospheric CH_4 has been documented in ice cores across large timescales, yet major uncertainties remain on how much methane is emitted from natural wetlands (Korrensalo *et al*., 2018; Melton *et al*., 2013; Riley *et al*., 2011). Vegetation reconstructions, by palynology, would be a

benefit to determine whether peat bogs likely changed in abundance across G-IG timescales (Bock *et al.*, 2017; Delmotte *et al.*, 2004). Palynological studies have been conducted at U1343 by Westbrook (2014) and Morris (2018) with success, though neither considered paleoclimates. Previous studies have captured the lateral expansion of peatlands and related the expansions to methane emissions across the Holocene (Jones & Yu, 2010; Smith, 2004), with Loisel *et al.* (2017) terming Beringia as a region with 'lost' wetlands.

Future works would consider whether concurrent increases in methane concentration and $\delta^{13}C$(methane) decreases occurring during global warming periods are driven by an increase in wetland fraction, through palynology and climatic ties.

References

Agustí, S., Sejr, M.K. and Duarte, C.M. 2010. Impacts of climate warming on polar marine and freshwater ecosystems. *Polar Biology*, **33**, 1595–1598, https://doi.org/10.1007/s00300-010-0955-0.

Ahn, S., Khider, D., Lisiecki, L.E. and Lawrence, C.E. 2017. A probabilistic Pliocene–Pleistocene stack of benthic $\delta^{18}O$ using a profile hidden Markov model. *Dynamics and Statistics of the Climate System*, **2**, https://doi.org/10.1093/climsys/dzx002.

Asahi, H. 2020. Updated age-depth ties for U1343. Email to Lauren Pankhurst, 12 May.

Asahi, H., Kender, S., *et al*. 2016. Orbital-scale benthic foraminiferal oxygen isotope stratigraphy at the northern Bering Sea Slope Site U1343 (IODP Expedition 323) and its Pleistocene paleoceanographic significance. *Deep Sea Research Part II: Topical Studies in Oceanography*, **125–126**, 66–83, https://doi.org/10.1016/j.dsr2.2014.01.004.

Atwood, T.B., Witt, A., Mayorga, J., Hammill, E. and Sala, E. 2020. Global patterns in marine sediment carbon stocks. *Frontiers in Marine Science*, **7**, https://doi.org/10.3389/fmars.2020.00165.

Barber, A., Brandes, J., *et al*. 2017. Preservation of organic matter in marine sediments by inner-sphere interactions with reactive iron. *Scientific Reports*, **7**, 366, https://doi.org/10.1038/s41598-017-00494-0.

Bartlein, P. J., Edwards, M. E., Hostetler, S. W., Shafer, S. L., Anderson, P. M., Brubaker, L. B., & Lozhkin, A. V. 2015. Early-Holocene warming in Beringia and its mediation by sea-level and vegetation changes. *Climate of the Past*, **11**, 1197–1222. https://doi.org/10.5194/cp-11-1197-2015.

Bechtel, A., Smittenberg, R.H., Bernasconi, S.M. and Schubert, C.J. 2010. Distribution of branched and isoprenoid tetraether lipids in an oligotrophic and a eutrophic Swiss lake: Insights into sources and GDGT-based proxies. *Organic Geochemistry*, **41**, 822–832, https://doi.org/10.1016/j.orggeochem.2010.04.022.

Bernardi, M., Petti, F.M. and Benton, M.J. 2018. Tetrapod distribution and temperature rise during the Permian–Triassic mass extinction. *Proceedings of the Royal Society B: Biological Sciences*, **285**, https://doi.org/10.1098/rspb.2017.2331.

Besseling, M.A., Hopmans, E.C., Bale, N.J., Schouten, S., Damsté, J.S.S. and Villanueva, L. 2020. The absence of intact polar lipid-derived GDGTs in marine waters dominated by Marine Group II: Implications for lipid biosynthesis in Archaea. *Scientific Reports*, **10**, 294, https://doi.org/10.1038/s41598-019-57035-0.

Blaga, C.I., Reichart, G.-J., Heiri, O. and Sinninghe Damsté, J.S. 2009. Tetraether membrane lipid distributions in water-column particulate matter and sediments: a study of 47 European lakes along a north–south transect. *Journal of Paleolimnology*, **41**, 523–540, https://doi.org/10.1007/s10933-008-9242-2.

Blaga, C.I., Reichart, G.-J., *et al.* 2010. Branched glycerol dialkyl glycerol tetraethers in lake sediments: Can they be used as temperature and pH proxies? *Organic Geochemistry*, **41**, 1225–1234, https://doi.org/10.1016/j.orggeochem.2010.07.002.

Bock, M., Schmitt, J., Beck, J., Seth, B., Chappellaz, J. and Fischer, H. 2017. Glacial/interglacial wetland, biomass burning, and geologic methane emissions constrained by dual stable isotopic CH_4 ice core records. *Proceedings of the National Academy of Sciences*, **114**, E5778–E5786, https://doi.org/10.1073/pnas.1613883114.

Bosin, A., Gorbarenko, S., Xuefa, S., Liu, Y. and Zou, J. 2015. Regionalized primary paleoproduction variability in the sea of Okhotsk during late Pleistocene and Holocene. *Journal of Asian Earth Sciences*, **114**, 534–540, https://doi.org/10.1016/j.jseaes.2015.07.019.

Brand, U., Posenato, R., Came, R., Affek, H., Angiolini, L., Azmy, K. and Farabegoli, E. 2012. The end-Permian mass extinction: A rapid volcanic CO_2 and CH_4 - climatic catastrophe. *Chemical Geology*, **322–323**, 121–144, https://doi.org/10.1016/j.chemgeo.2012.06.015.

Brand, U., Blamey, N., *et al.* 2016. Methane Hydrate: Killer cause of Earth's greatest mass extinction. *Palaeoworld*, **25**, 496–507, https://doi.org/10.1016/j.palwor.2016.06.002.

Brassell, S.C., Eglinton, G., Marlowe, I.T., Pflaumann, U. and Sarnthein, M. 1986. Molecular stratigraphy: a new tool for climatic assessment. *Nature*, **320**, 129-133, https://doi.org/10.1038/320129a0.

Bridgham, S.D., Cadillo-Quiroz, H., Keller, J.K. and Zhuang, Q. 2013. Methane emissions from wetlands: biogeochemical, microbial, and modelling perspectives from local to global scales. *Global Change Biology*, **19**, 1325–1346, https://doi.org/10.1111/gcb.12131.

Brock, T.D. 1978. The Genus Thermoplasma. *In*: *Thermophilic Microorganisms and Life at High Temperatures*. Springer Series in Microbiology, 92–116., https://doi.org/10.1007/978-1-4612-6284-8_5.

Burgess, S.D., Bowring, S. and Shen, S. 2014. High-precision timeline for Earth's most severe extinction. *Proceedings of the National Academy of Sciences*, **111**, 3316–3321, https://doi.org/10.1073/pnas.1317692111.

Canadell, J.G., Monterio, P.M.S., Costa, M.H., Cotrim de Cunha, L. and Cox, P.M. 2021. Chapter 5: Global Carbon and Other Biogeochemical Cycles and Feedbacks. *In*: *Climate Change 2021: The Physical Science Basis. Contribution of Working Group I to the Sixth Assessment Report of the Intergovernmental Panel on Climate Change*. 673–816.

Casagrande, F., Nobre, P., *et al.* 2021. Climate sensitivity in the northern high latitudes using the Brazilian Earth System Model. *Conjecturas*, **21**, 192–211, https://doi.org/10.53660/CONJ-260-107.

Castañeda, I.S., Mulitza, S., Schefuß, E., Santos, R.A.L. dos, Damsté, J.S.S. and Schouten, S. 2009. Wet phases in the Sahara/Sahel region and human migration patterns in North Africa. *Proceedings of the National Academy of Sciences*, **106**, 20159–20163, https://doi.org/10.1073/pnas.0905771106.

Castellani, G., Veyssière, G., *et al.* 2022. Shine a light: Under-ice light and its ecological implications in a changing Arctic Ocean. *Ambio*, **51**, 307–317, https://doi.org/10.1007/s13280-021-01662-3.

Castro, H.F., Classen, A.T., Austin, E.E., Norby, R.J. and Schadt, C.W. 2010. Soil microbial community responses to multiple experimental climate change drivers. *Applied and Environmental Microbiology*, **76**, 999–1007, https://doi.org/10.1128/AEM.02874-09.

Ceccopieri, M., Carreira, R.S., Wagener, A.L.R., Hefter, J. and Mollenhauer, G. 2019. Branched GDGTs as proxies in surface sediments from the south-eastern Brazilian continental margin. *Frontiers in Earth Science*, **7**, 1–14, https://doi.org/10.3389/feart.2019.00291.

Chen, M.-H., Zhang, Q., Zhang, L.-L., Zarikian, C.A. and Wang, R.-J. 2014. Stratigraphic distribution of the radiolarian Spongodiscus biconcavus Haeckel at IODP Site U1340 in the Bering Sea and its paleoceanographic significance. *Palaeoworld*, **23**, 90–104, https://doi.org/10.1016/j.palwor.2013.11.001.

Christiansen, B. and Ljungqvist, F.C. 2017. Challenges and perspectives for large-scale temperature reconstructions of the past two millennia. *Reviews of Geophysics*, **55**, 40–96, https://doi.org/10.1002/2016RG000521.

Clark, P.U., Dyke, A.S., *et al.* 2009. The Last Glacial Maximum. *Science*, **325**, 710–714, https://doi.org/10.1126/science.1172873.

Conte, M.H., Sicre, M.-A., Rühlemann, C., Weber, J.C., Schulte, S., Schulz-Bull, D. and Blanz, T. 2006. Global temperature calibration of the alkenone unsaturation index ($U_{37}^{K'}$) in surface waters and comparison with surface sediments: Alkenone Unsaturation Index. *Geochemistry, Geophysics, Geosystems*, **7**, https://doi.org/10.1029/2005GC001054.

Cooper, A., Turney, C., Hughen, K.A., Brook, B.W., McDonald, H.G. and Bradshaw, C.J.A. 2015. Abrupt warming events drove Late Pleistocene Holarctic megafaunal turnover. *Science*, **349**, 602–606, https://doi.org/10.1126/science.aac4315.

Corell, R.W. 2006. Challenges of climate change: An Arctic perspective. *Ambio*, **35**, 148–152.

Cox, P.M., Betts, R.A., Jones, C.D., Spall, S.A. and Totterdell, I.J. 2000. Acceleration of global warming due to carbon-cycle feedbacks in a coupled climate model. *Nature*, **408**, 184–187, https://doi.org/10.1038/35041539.

Cui, Y., Li, M., van Soelen, E.E., Peterse, F. and Kürschner, W.M. 2021. Massive and rapid predominantly volcanic CO_2 emission during the end-Permian mass extinction. *Proceedings of the National Academy of Sciences*, **118**, e2014701118, https://doi.org/10.1073/pnas.2014701118.

Dawson, K.S., Freeman, K.H. and Macalady, J.L. 2012. Molecular characterization of core lipids from halophilic archaea grown under different salinity conditions. *Organic Geochemistry*, **48**, 1–8, https://doi.org/10.1016/j.orggeochem.2012.04.003.

De Boer, A.M. and Nof, D. 2004. The Bering Strait's grip on the northern hemisphere climate. *Deep Sea Research Part I: Oceanographic Research Papers*, **51**, 1347–1366, https://doi.org/10.1016/j.dsr.2004.05.003.

De Jonge, C., Hopmans, E.C., Stadnitskaia, A., Rijpstra, W.I.C., Hofland, R., Tegelaar, E. and Sinninghe Damsté, J.S. 2013. Identification of novel penta- and hexamethylated branched glycerol dialkyl glycerol tetraethers in peat using HPLC–MS[2], GC–MS and GC–SMB-MS. *Organic Geochemistry*, **54**, 78–82, https://doi.org/10.1016/j.orggeochem.2012.10.004.

De Jonge, C., Hopmans, E.C., Zell, C.I., Kim, J.-H., Schouten, S. and Sinninghe Damsté, J.S. 2014. Occurrence and abundance of 6-methyl branched glycerol dialkyl glycerol tetraethers in soils: Implications for palaeoclimate reconstruction. *Geochimica et Cosmochimica Acta*, **141**, 97–112, https://doi.org/10.1016/j.gca.2014.06.013.

De Jonge, C., Stadnitskaia, A., *et al.* 2015. Drastic changes in the distribution of branched tetraether lipids in suspended matter and sediments from the Yenisei River and Kara Sea (Siberia): Implications for the use of brGDGT-based proxies in coastal marine sediments. *Geochimica et Cosmochimica Acta*, **165**, 200–225, https://doi.org/10.1016/j.gca.2015.05.044.

de la Torre, J.R., Walker, C.B., Ingalls, A.E., Könneke, M. and Stahl, D.A. 2008. Cultivation of a thermophilic ammonia oxidizing archaeon synthesizing crenarchaeol. *Environmental Microbiology*, **10**, 810–818, https://doi.org/10.1111/j.1462-2920.2007.01506.x.

Dearing Crampton-Flood, E., van der Weijst, C.M.H., *et al.* 2021. Identifying marine and freshwater overprints on soil-derived branched GDGT temperature signals in Pliocene Mississippi and Amazon River fan sediments. *Organic Geochemistry*, **154.** https://doi.org/10.1016/j.orggeochem.2021.104200.

Dearing Crampton-Flood, E., Tierney, J.E., Peterse, F., Kirkels, F.M.S.A. and Sinninghe Damsté, J.S. 2020. BayMBT: A Bayesian calibration model for branched glycerol dialkyl glycerol tetraethers in soils and peats. *Geochimica et Cosmochimica Acta*, **268**, 142–159, https://doi.org/10.1016/j.gca.2019.09.043.

Delmotte, M., Chappellaz, J., *et al.* 2004. Atmospheric methane during the last four glacial-interglacial cycles: Rapid changes and their link with Antarctic temperature. *Journal of Geophysical Research: Atmospheres*, **109**, https://doi.org/10.1029/2003JD004417.

DeLong, E.F. 2021. Exploring Marine Planktonic Archaea: Then and Now. *Frontiers in Microbiology*, **11**. https://doi.org/10.3389/fmicb.2020.616086.

Detlef, H. 2018. *Paleoceanography of the Bering Sea across the Mid- to Late Pleistocene.* Cardiff University.

Detlef, H., Belt, S.T., *et al.* 2018. Sea ice dynamics across the Mid-Pleistocene transition in the Bering Sea. *Nature Communications*, **9**, 941, https://doi.org/10.1038/s41467-018-02845-5.

Detlef, H., Sosdian, S.M., Kender, S., Lear, C.H. and Hall, I.R. 2020. Multi-elemental composition of authigenic carbonates in benthic foraminifera from the eastern Bering Sea continental margin (International Ocean Discovery Program Site U1343). *Geochimica et Cosmochimica Acta*, **268**, 1–21, https://doi.org/10.1016/j.gca.2019.09.025.

Doughty, A. M., Kaplan, M. R., Peltier, C., & Barker, S. 2021. A maximum in global glacier extent during MIS 4. *Quaternary Science Reviews*, *261*. https://doi.org/10.1016/j.quascirev.2021.106948.

Douglas, T.A., Jones, M.C., Hiemstra, C.A. and Arnold, J.R. 2014. Sources and sinks of carbon in boreal ecosystems of interior Alaska: A review. *Elementa: Science of the Anthropocene*, **2**. https://doi.org/10.12952/journal.elementa.000032.

Dugerdil, L., Joannin, S., *et al.* 2020. Climate reconstructions based on GDGT and pollen surface datasets from Mongolia and Siberia: calibrations and applicability to extremely cold-dry environments over the Late Holocene. *In*: EGU. 1–39., https://doi.org/10.5194/cp-2020-154.

Elling, F.J., Könneke, M., Mußmann, M., Greve, A. and Hinrichs, K.-U. 2015. Influence of temperature, pH, and salinity on membrane lipid composition and TEX_{86} of marine planktonic thaumarchaeal isolates. *Geochimica et Cosmochimica Acta*, **171**, 238–255, https://doi.org/10.1016/j.gca.2015.09.004.

Expedition 323 Scientists. 2010. *Integrated Ocean Drilling Program Expedition 323 Preliminary Report*. IODP Preliminary Report, **323**, https://doi.org/10.2204/iodp.pr.323.2010.

Fischer, H., Behrens, M., *et al.* 2008. Changing boreal methane sources and constant biomass burning during the last termination. *Nature*, **452**, 864–867, https://doi.org/10.1038/nature06825.

Foster, L.C. 2015. *Reconstructing Mid-Late Holocene Climate and Environmental Change in Antarctica Using Glycerol Dialkyl Glycerol Tetraethers (GDGTs) and Pigments in Lake Sediments*. Degree of Doctor of Philosophy, Newcastle University.

Friedlingstein, P. 2015. Carbon cycle feedbacks and future climate change. *Philosophical Transactions of the Royal Society A: Mathematical, Physical and Engineering Sciences*, **373**. https://doi.org/10.1098/rsta.2014.0421.

Friedlingstein, P., O'Sullivan, M., *et al.* 2020. Global Carbon Budget 2020. *Earth System Science Data*, **12**, 3269–3340, https://doi.org/10.5194/essd-12-3269-2020.

Gautier, D.L., Bird, K.J., *et al.* 2009. Assessment of Undiscovered Oil and Gas in the Arctic. *Science*, **324**, 1175–1179, https://doi.org/10.1126/science.1169467.

Gehler, A., Gingerich, P.D. and Pack, A. 2016. Temperature and atmospheric CO_2 concentration estimates through the PETM using triple oxygen isotope analysis of mammalian bioapatite. *Proceedings of the National Academy of Sciences*, **113**, 7739–7744, https://doi.org/10.1073/pnas.1518116113.

Gies, H., Hagedorn, F., Lupker, M., Montluçon, D., Haghipour, N., van der Voort, T.S. and Eglinton, T.I. 2021. Millennial-age glycerol dialkyl glycerol tetraethers (GDGTs) in forested mineral soils: ^{14}C-based evidence for stabilization of microbial necromass. *Biogeosciences*, **18**, 189–205, https://doi.org/10.5194/bg-18-189-2021.

Gliozzi, A., Paoli, G., De Rosa, M. and Gambacorta, A. 1983. Effect of isoprenoid cyclization on the transition temperature of lipids in thermophilic archaebacteria. *Biochimica et Biophysica Acta (BBA) - Biomembranes*, **735**, 234–242, https://doi.org/10.1016/0005-2736(83)90298-5.

Gorham, E. 1991. Northern Peatlands: Role in the carbon cycle and probable responses to climatic warming. *Ecological Applications*, **1**, 182–195, https://doi.org/10.2307/1941811.

Gruber, N., Friedlingstein, P., *et al.* 2004. The vulnerability of the carbon cycle in the 21st century: An assessment of carbon-climate-human interactions. *In*: *The Global Carbon Cycle,* 45–76.

Guo, J., Yuan, H., *et al.* 2021. Variation of Isoprenoid GDGTs in the Stratified Marine Water Column: Implications for GDGT-Based TEX_{86} Paleothermometry. *Frontiers in Marine Science*, **8**.

Harrison, S.P., Bartlein, P.J., *et al.* 2015. Evaluation of CMIP5 palaeo-simulations to improve climate projections. *Nature Climate Change*, **5**, 735–743, https://doi.org/10.1038/nclimate2649.

Haynes, L.L. and Hönisch, B. 2020. The seawater carbon inventory at the Paleocene–Eocene Thermal Maximum. *Proceedings of the National Academy of Sciences*, **117**, 24088–24095, https://doi.org/10.1073/pnas.2003197117.

Hebting, Y. 2006. Biomarker Evidence for a Major Preservation Pathway of Sedimentary Organic Carbon. *Science*, **312**, 1627–1631, https://doi.org/10.1126/science.1126372.

Herfort, L., Schouten, S., *et al.* 2007. Variations in spatial and temporal distribution of Archaea in the North Sea in relation to environmental variables: Marine Archaea in the North Sea. *FEMS Microbiology Ecology*, **62**, 242–257, https://doi.org/10.1111/j.1574-6941.2007.00397.x.

Hjort, J., Karjalainen, O., *et al.* 2018. Degrading permafrost puts Arctic infrastructure at risk by mid-century. *Nature Communications*, **9**, 5147, https://doi.org/10.1038/s41467-018-07557-4.

Ho, S.L., Yamamoto, M., Mollenhauer, G. and Minagawa, M. 2011. Core top TEX_{86} values in the south and equatorial Pacific. *Organic Geochemistry*, **42**, 94–99, https://doi.org/10.1016/j.orggeochem.2010.10.012.

Ho, S.L., Mollenhauer, G., *et al.* 2014. Appraisal of TEX_{86} and TEX_{86}^{L} thermometries in subpolar and polar regions. *Geochimica et Cosmochimica Acta*, **131**, 213–226, https://doi.org/10.1016/j.gca.2014.01.001.

Hou, S., Lamprou, F., Hoem, F. S., Hadju, M. R. N., Sangiorgi, F., Peterse, F., & Bijl, P. K.. 2023. Lipid-biomarker-based sea surface temperature record offshore Tasmania over the last 23 million years. *Climate of the Past*, **19**, 787–802. https://doi.org/10.5194/cp-19-787-2023

Hopmans, E.C., Schouten, S., Pancost, R.D., van der Meer, M.T.J. and Sinninghe Damsté, J.S. 2000. Analysis of intact tetraether lipids in archaeal cell material and sediments by high performance liquid chromatography/atmospheric pressure chemical ionization mass spectrometry. *Rapid Communications in Mass Spectrometry*, **14**, 585–589, https://doi.org/10.1002/(SICI)1097-0231(20000415)14:7<585::AID-RCM913>3.0.CO;2-N.

Hopmans, E.C., Weijers, J.W.H., Schefuß, E., Herfort, L., Sinninghe Damsté, J.S. and Schouten, S. 2004. A novel proxy for terrestrial organic matter in sediments based on branched and isoprenoid tetraether lipids. *Earth and Planetary Science Letters*, **224**, 107–116, https://doi.org/10.1016/j.epsl.2004.05.012.

Hopmans, E.C., Schouten, S. and Sinninghe Damsté, J.S. 2016. The effect of improved chromatography on GDGT-based palaeoproxies. *Organic Geochemistry*, **93**, 1–6, https://doi.org/10.1016/j.orggeochem.2015.12.006.

Hu, A., Meehl, G.A., Han, W., Otto-Bliestner, B., Abe-Ouchi, A. and Rosenbloom, N. 2015. Effects of the Bering Strait closure on AMOC and global climate under different background climates. *Progress in Oceanography*, **132**, 174–196, https://doi.org/10.1016/j.pocean.2014.02.004.

Hugelius, G., Loisel, J., *et al.* 2020. Large stocks of peatland carbon and nitrogen are vulnerable to permafrost thaw. *Proceedings of the National Academy of Sciences*, **117**, 20438–20446, https://doi.org/10.1073/pnas.1916387117.

Huguet, A., Fosse, C., Laggoun-Défarge, F., Delarue, F. and Derenne, S. 2013. Effects of a short-term experimental microclimate warming on the abundance and distribution of branched GDGTs in a French peatland. *Geochimica et Cosmochimica Acta*, **105**, 294–315, https://doi.org/10.1016/j.gca.2012.11.037.

Huguet, C., Hopmans, E.C., Febo-Ayala, W., Thompson, D.H., Sinninghe Damsté, J.S. and Schouten, S. 2006a. An improved method to determine the absolute abundance of glycerol dibiphytanyl glycerol tetraether lipids. *Organic Geochemistry*, **37**, 1036–1041, https://doi.org/10.1016/j.orggeochem.2006.05.008.

Huguet, C., Kim, J.-H., Sinninghe Damsté, J.S. and Schouten, S. 2006b. Reconstruction of sea surface temperature variations in the Arabian Sea over the last 23 kyr using organic proxies (TEX$_{86}$ and U$_{37}^{K'}$). *Paleoceanography*, **21**, https://doi.org/10.1029/2005PA001215.

Huguet, C., Martens-Habbena, W., Urakawa, H., Stahl, D.A. and Ingalls, A.E. 2010. Comparison of extraction methods for quantitative analysis of core and intact polar glycerol dialkyl glycerol tetraethers (GDGTs) in environmental samples. *Limnology and Oceanography: Methods*, **8**, 127–145, https://doi.org/10.4319/lom.2010.8.127.

Inglis, G.N., Farnsworth, A., *et al.* 2015. Descent toward the Icehouse: Eocene sea surface cooling inferred from GDGT distributions. *Paleoceanography*, **30**, 1000–1020, https://doi.org/10.1002/2014PA002723.

IPCC, 2007: Climate Change 2007: The Physical Science Basis. *Contribution of Working Group I to the Fourth Assessment Report of the Intergovernmental Panel on Climate Change* [Solomon, S., D. Qin, M. Manning, Z. Chen, M. Marquis, K.B. Averyt, M. Tignor and H.L. Miller (eds.)]. Cambridge University Press, Cambridge, United Kingdom and New York, NY, USA.

IPCC, 2021: Summary for Policymakers. *In: Climate Change 2021: The Physical Science Basis. Contribution of Working Group I to the Sixth Assessment Report of the Intergovernmental Panel on Climate Change* [MassonDelmotte, V., P. Zhai, A. Pirani, S.L. Connors, C. Péan, S. Berger, N. Caud, Y. Chen, L. Goldfarb, M.I. Gomis, M. Huang, K. Leitzell, E. Lonnoy, J.B.R. Matthews, T.K. Maycock, T. Waterfield, O. Yelekçi, R. Yu, and B. Zhou (eds.)]. Cambridge University Press, Cambridge, United Kingdom and New York, NY, USA, pp. 3−32, doi: 10.1017/9781009157896.001.

Iwasaki, S., Takahashi, K., Kanematsu, Y., Asahi, H., Onodera, J. and Ravelo, A.C. 2016. Paleoproductivity and paleoceanography of the last 4.3 Myrs at IODP Expedition 323 Site U1341 in the Bering Sea based on biogenic opal content. *Deep Sea Research Part II: Topical Studies in Oceanography*, **125–126**, 145–154, https://doi.org/10.1016/j.dsr2.2015.04.005.

Joachimski, M.M., Alekseev, A.S., Grigoryan, A. and Gatovsky, Yu.A. 2020. Siberian Trap volcanism, global warming and the Permian-Triassic mass extinction: New insights from Armenian Permian-Triassic sections. *GSA Bulletin*, **132**, 427–443, https://doi.org/10.1130/B35108.1.

Johnson, G.C. and Stabeno, P.J. 2017. Deep Bering Sea circulation and variability, 2001–2016, From Argo Data. *Journal of Geophysical Research: Oceans*, **122**, 9765–9779, https://doi.org/10.1002/2017JC013425.

Jones, M. and Yu, Z. 2010. Rapid deglacial and early Holocene expansion of peatlands in Alaska. *Proceedings of the National Academy of Sciences of the United States of America*, **107**, 7347–7352, https://doi.org/10.1073/pnas.0911387107.

Kaushik, A., Graham, J., Dorheim, K., Kramer, R., Wang, J. and Byrne, B. 2020. The Future of the Carbon Cycle in a Changing Climate. *Eos* https://doi.org/10.1029/2020EO140276.

Kender, S., Ravelo, A.C., *et al.* 2018. Closure of the Bering Strait caused Mid-Pleistocene transition cooling. *Nature Communications*, **9**, 5386, https://doi.org/10.1038/s41467-018-07828-0.

Kent, D.V., Cramer, B.S., Lanci, L., Wang, D., Wright, J.D. and Van der Voo, R. 2003. A case for a comet impact trigger for the Paleocene/Eocene thermal maximum and carbon isotope excursion. *Earth and Planetary Science Letters*, **211**, 13–26, https://doi.org/10.1016/S0012-821X(03)00188-2.

Kim, J.-H., Schouten, S., Hopmans, E.C., Donner, B. and Sinninghe Damsté, J.S. 2008. Global sediment core-top calibration of the TEX_{86} paleothermometer in the ocean. *Geochimica et Cosmochimica Acta*, **72**, 1154–1173, https://doi.org/10.1016/j.gca.2007.12.010.

Kim, J.-H., van der Meer, J., *et al.* 2010. New indices and calibrations derived from the distribution of crenarchaeal isoprenoid tetraether lipids: Implications for past sea surface temperature reconstructions. *Geochimica et Cosmochimica Acta*, **74**, 4639–4654, https://doi.org/10.1016/j.gca.2010.05.027.

Kim, J.-H., Schouten, S., *et al.* 2015. Influence of deep-water derived isoprenoid tetraether lipids on the TEX_{86}^{H} paleothermometer in the Mediterranean Sea. *Geochimica et Cosmochimica Acta*, **150**, 125–141, https://doi.org/10.1016/j.gca.2014.11.017.

Kim, S., Takahashi, K., Khim, B.-K., Kanematsu, Y., Asahi, H. and Ravelo, A.C. 2014. Biogenic opal production changes during the Mid-Pleistocene Transition in the Bering Sea (IODP Expedition 323 Site U1343). *Quaternary Research*, **81**, 151–157, https://doi.org/10.1016/j.yqres.2013.10.001.

Koga, Y., Kyuragi, T., Nishihara, M. and Sone, N. 1998. Did archaeal and bacterial cells arise independently from noncellular precursors? A hypothesis stating that the advent of membrane phospholipid with enantiomeric glycerophosphate backbones caused the separation of the two lines of descent. *Journal of Molecular Evolution*, **46**, 54–63, https://doi.org/10.1007/pl00006283.

Kornilova, O. and Rosell-Melé, A. 2003. Application of microwave-assisted extraction to the analysis of biomarker climate proxies in marine sediments. *Organic Geochemistry*, **34**, 1517–1523, https://doi.org/10.1016/S0146-6380(03)00155-4.

Korrensalo, A., Männistö, E., Alekseychik, P., Mammarella, I., Rinne, J., Vesala, T. and Tuittila, E.-S. 2018. Small spatial variability in methane emission measured from a wet patterned boreal bog. *Biogeosciences*, **15**, 1749–1761, https://doi.org/10.5194/bg-15-1749-2018.

Larsen, J.N. *et al.* 2014. Polar Regions. *Climate Change 2014: Impacts, Adaptation, and Vulnerability. Part B: Regional Aspects. Contribution of Working Group II to the Fifth Assessment Report of the Intergovernmental Panel on Climate Change*, [VR Barros, *et al.* (eds.)] Cambridge University Press, Cambridge, United Kingdom, 1567–1612.

Lawrence, K.T., Pearson, A., Castañeda, I.S., Ladlow, C., Peterson, L.C. and Lawrence, C.E. 2020. Comparison of Late Neogene $U^{K'}_{37}$ and TEX_{86} paleotemperature records from the Eastern Equatorial Pacific at Orbital Resolution. *Paleoceanography and Paleoclimatology*, **35**, https://doi.org/10.1029/2020PA003858.

Lécuyer, C., Hillaire-Marcel, C., Burke, A., Julien, M.-A. and Hélie, J.-F. 2021. Temperature and precipitation regime in LGM human refugia of southwestern Europe inferred from $\delta^{13}C$ and $\delta^{18}O$ of large mammal remains. *Quaternary Science Reviews*, **255**, 106796, https://doi.org/10.1016/j.quascirev.2021.106796.

Lei, Y., Yang, H., Dang, X., Zhao, S. and Xie, S. 2016. Absence of a significant bias towards summer temperature in branched tetraether-based paleothermometer at two soil sites with contrasting temperature seasonality. *Organic Geochemistry*, **94**, 83–94, https://doi.org/10.1016/j.orggeochem.2016.02.003.

Lengger, S. K., Hopmans, E. C., Sinninghe Damsté, J. S., & Schouten, S. 2012. Comparison of extraction and work up techniques for analysis of core and intact polar tetraether lipids from sedimentary environments. *Organic Geochemistry*, **47,** 34–40. https://doi.org/10.1016/j.orggeochem.2012.02.009

Lengger, S.K., Sutton, P.A., *et al*. 2018. Archaeal and bacterial glycerol dialkyl glycerol tetraether (GDGT) lipids in environmental samples by high temperature-gas chromatography with flame ionisation and time-of-flight mass spectrometry detection. *Organic Geochemistry*, **121**, 10–21, https://doi.org/10.1016/j.orggeochem.2018.03.012.

Letellier, M., & Budzinski, H. 1999. Microwave assisted extraction of organic compounds. **27**. https://doi.org/10.1051/analusis:1999116

Li, Q., Ma, M., Wu, X., & Yang, H. 2018. Snow Cover and Vegetation-Induced Decrease in Global Albedo From 2002 to 2016. *Journal of Geophysical Research: Atmospheres*, **123,** 124–138. https://doi.org/10.1002/2017JD027010

Li, D., Zhao, M., Tian, J. and Li, L. 2013. Comparison and implication of TEX_{86} and $U^{K'}_{37}$ temperature records over the last 356kyr of ODP Site 1147 from the northern South China Sea. *Palaeogeography, Palaeoclimatology, Palaeoecology*, **376**, 213–223, https://doi.org/10.1016/j.palaeo.2013.02.031.

Lisiecki, L.E. and Raymo, M.E. 2005. A Pliocene-Pleistocene stack of 57 globally distributed benthic $\delta^{18}O$ records. *Paleoceanography*, **20**, https://doi.org/10.1029/2004PA001071.

Liu, Z., Pagani, M., *et al*. 2009a. Global cooling during the Eocene-Oligocene climate transition. *Science*, **323**, 1187–1190, https://doi.org/10.1126/science.1166368.

Liu, Z., Otto-Bliesner, B.L., *et al*. 2009b. Transient simulation of last deglaciation with a new mechanism for Bølling-Allerød warming. *Science*, **325**, 310–314, https://doi.org/10.1126/science.1171041.

Loisel, J., van Bellen, S., *et al*. 2017. Insights and issues with estimating northern peatland carbon stocks and fluxes since the Last Glacial Maximum. *Earth-Science Reviews*, **165**, 59–80, https://doi.org/10.1016/j.earscirev.2016.12.001.

Loomis, S.E., Russell, J.M. and Sinninghe Damsté, J.S. 2011. Distributions of branched GDGTs in soils and lake sediments from western Uganda: Implications for a lacustrine paleothermometer. *Organic Geochemistry*, **42**, 739–751, https://doi.org/10.1016/j.orggeochem.2011.06.004.

Loomis, S.E., Russell, J.M., Ladd, B., Street-Perrott, F.A. and Sinninghe Damsté, J.S. 2012. Calibration and application of the branched GDGT temperature proxy on East African lake sediments. *Earth and Planetary Science Letters*, **357–358**, 277–288, https://doi.org/10.1016/j.epsl.2012.09.031.

Lopes dos Santos, R.A., Prange, M., *et al.* 2010. Glacial–interglacial variability in Atlantic meridional overturning circulation and thermocline adjustments in the tropical North Atlantic. *Earth and Planetary Science Letters*, **300**, 407–414, https://doi.org/10.1016/j.epsl.2010.10.030.

Lowe, J.J. and Walker, M.J.C. 2014. *Reconstructing Quaternary Environments*, 3rd Edition. https://doi.org/10.4324/9781315797496.

Marcott, S.A., Shakun, J.D., Clark, P.U. and Mix, A.C. 2013. A reconstruction of regional and global temperature for the past 11,300 years. *Science*, **339**, 1198–1201, https://doi.org/10.1126/science.1228026.

März, C., Schnetger, B. and Brumsack, H.-J. 2013. Nutrient leakage from the North Pacific to the Bering Sea (IODP Site U1341) following the onset of Northern Hemispheric Glaciation? *Paleoceanography*, **28**, 68–78, https://doi.org/10.1002/palo.20011.

Masson-Delmotte, V., *et al.* 2013, Information from paleoclimate archives, in Climate Change 2013: The Physical Science Basis. Contribution of Working Group I to the Fifth Assessment Report of the Intergovernmental Panel on Climate Change, edited by T. F. Stocker *et al.*, Cambridge University Press, Cambridge, United Kingdom and New York, USA.

Mayewski, P.A., Rohling, E.E., *et al.* 2004. Holocene climate variability. *Quaternary Research*, **62**, 243–255, https://doi.org/10.1016/j.yqres.2004.07.001.

McClymont, E. L., Ganeshram, R. S., Pichevin, L. E., Talbot, H. M., van Dongen, B. E., Thunell, R. C., et al. 2012. Sea-surface temperature records of Termination 1 in the Gulf of California: Challenges for seasonal and interannual analogues of tropical Pacific climate change. *Paleoceanography*, **27**. https://doi.org/10.1029/2011PA002226

Melton, J.R., Wania, R., *et al.* 2013. Present state of global wetland extent and wetland methane modelling: conclusions from a model inter-comparison project (WETCHIMP). *Biogeosciences*, **10**, 753–788, https://doi.org/10.5194/bg-10-753-2013.

Melvin, A.M., Larsen, P., *et al.* 2017. Climate change damages to Alaska public infrastructure and the economics of proactive adaptation. *Proceedings of the National Academy of Sciences*, **114**, E122–E131, https://doi.org/10.1073/pnas.1611056113.

Michel, C., Legendre, L., Demers, S. and Therriault, J.-C. 1988. Photoadaptation of sea-ice microalgae in springtime: photosynthesis and carboxylating enzymes. *Marine Ecology Progress Series*, **50**, 177–185, https://doi.org/10.3354/meps050177.

Möller, L., Sowers, T., *et al.* 2013. Independent variations of CH_4 emissions and isotopic composition over the past 160,000 years. *Nature Geoscience*, **6**, 885–890, https://doi.org/10.1038/ngeo1922.

Morcillo-Montalbá, L., Rodrigo-Gámiz, M., Martínez-Ruiz, F., Ortega-Huertas, M., Schouten, S. and Sinninghe Damsté, J.S. 2021. Rapid climate changes in the westernmost Mediterranean (Alboran sea) over the last 35 kyr: new insights from four lipid paleothermometers ($U_{37}^{K'}$, TEX_{86}^{H}, RI-OH', and LDI). *Paleoceanography and Paleoclimatology*, **36**, https://doi.org/10.1029/2020PA004171.

Morris, E.P. 2018. *Evidence for the Presence of Mesic Herbaceous Shrub Tundra with Isolated Stands of Trees in South Central Beringia during Glacial Stages 2 - 16*. Thesis.

Müller, P.J., Kirst, G., Ruhland, G., von Storch, I. and Rosell-Melé, A. 1998. Calibration of the alkenone paleotemperature index $U_{37}^{K'}$ based on core-tops from the eastern South Atlantic and the global ocean (60°N-60°S). *Geochimica et Cosmochimica Acta*, **62**, 1757–1772, https://doi.org/10.1016/S0016-7037(98)00097-0.

Naafs, B.D.A., Gallego-Sala, A.V., Inglis, G.N. and Pancost, R.D. 2017a. Refining the global branched glycerol dialkyl glycerol tetraether (brGDGT) soil temperature calibration. *Organic Geochemistry*, **106**, 48–56, https://doi.org/10.1016/j.orggeochem.2017.01.009.

Naafs, B.D.A., Inglis, G.N., *et al*. 2017b. Introducing global peat-specific temperature and pH calibrations based on brGDGT bacterial lipids. *Geochimica et Cosmochimica Acta*, **208**, 285–301, https://doi.org/10.1016/j.gca.2017.01.038.

Naafs, B.D.A., McCormick, D., Inglis, G.N. and Pancost, R.D. 2018. Archaeal and bacterial H-GDGTs are abundant in peat and their relative abundance is positively correlated with temperature. *Geochimica et Cosmochimica Acta*, **227**, 156–170, https://doi.org/10.1016/j.gca.2018.02.025.

Naafs, B.D.A., Oliveira, A.S.F. and Mulholland, A.J. 2021. Molecular dynamics simulations support the hypothesis that the brGDGT paleothermometer is based on homeoviscous adaptation. *Geochimica et Cosmochimica Acta*, **312**, 44–56, https://doi.org/10.1016/j.gca.2021.07.034.

O'Connor, L. K., Crampton-Flood, E. D., Jerrett, R. M., Price, G. D., Naafs, B. D. A., Pancost, R. D., et al. 2023. Steady decline in mean annual air temperatures in the first 30 k.y. after the Cretaceous-Paleogene boundary. *Geology*, **51**, 486–490. https://doi.org/10.1130/G50588.1

Oppermann, B.I., Michaelis, W., *et al*. 2010. Soil microbial community changes as a result of long-term exposure to a natural CO_2 vent. *Geochimica et Cosmochimica Acta*, **74**, 2697–2716, https://doi.org/10.1016/j.gca.2010.02.006.

Pancost, R.D., van Geel, B., Baas, M. and Damsté, J.S.S. 2000. $\delta^{13}C$ values and radiocarbon dates of microbial biomarkers as tracers for carbon recycling in peat deposits. *Geology*, **28**, 663–666, https://doi.org/10.1130/0091-7613(2000)28<663:CVARDO>2.0.CO;2.

Pancost, R.D., Bouloubassi, I., Aloisi, G., Sinninghe Damsté, J.S. and Scientific Party, the M.S. 2001. Three series of non-isoprenoidal dialkyl glycerol diethers in cold-seep carbonate crusts. *Organic Geochemistry*, **32**, 695–707, https://doi.org/10.1016/S0146-6380(01)00015-8.

Park, E., Hefter, J., Fischer, G., Iversen, M.H., Ramondenc, S., Nöthig, E.-M. and Mollenhauer, G. 2019. Seasonality of archaeal lipid flux and GDGT-based thermometry in sinking particles of high-latitude oceans: Fram Strait (79°N) and Antarctic Polar Front (50°S). *Biogeosciences*, **16**, 2247–2268, https://doi.org/10.5194/bg-16-2247-2019.

Peaple, M.D., Beverly, E.J., *et al.* 2022. Identifying the drivers of GDGT distributions in alkaline soil profiles within the Serengeti ecosystem. *Organic Geochemistry*, **169**, 104433, https://doi.org/10.1016/j.orggeochem.2022.104433.

Pearson, E.J., Juggins, S., *et al.* 2011. A lacustrine GDGT-temperature calibration from the Scandinavian Arctic to Antarctic: Renewed potential for the application of GDGT-paleothermometry in lakes. *Geochimica et Cosmochimica Acta*, **75**, 6225–6238, https://doi.org/10.1016/j.gca.2011.07.042.

Peterse, F., Kim, J.-H., Schouten, S., Kristensen, D., Koc, N. and Sinninghe-Damsté, J. 2009. Constraints on the application of the MBT/CBT palaeothermometer at high latitude environments (Svalbard, Norway). *Organic Geochemistry*, **40**, 692–699, https://doi.org/10.1016/j.orggeochem.2009.03.004.

Peterse, F., van der Meer, J., *et al.* 2012. Revised calibration of the MBT–CBT paleotemperature proxy based on branched tetraether membrane lipids in surface soils. *Geochimica et Cosmochimica Acta*, **96**, 215–229, https://doi.org/10.1016/j.gca.2012.08.011.

Pitcher, A., Rychlik, N., *et al.* 2010. Crenarchaeol dominates the membrane lipids of Candidatus Nitrososphaera gargensis, a thermophilic Group I.1b Archaeon. *The ISME Journal*, **4**, 542–552, https://doi.org/10.1038/ismej.2009.138.

Pitcher, A., Hopmans, E.C., *et al.* 2011. Core and intact polar glycerol dibiphytanyl glycerol tetraether lipids of ammonia-oxidizing archaea enriched from marine and estuarine sediments. *Applied and Environmental Microbiology*, **77**, 3468–3477, https://doi.org/10.1128/AEM.02758-10.

Powers, L., Werne, J.P., Vanderwoude, A.J., Sinninghe Damsté, J.S., Hopmans, E.C. and Schouten, S. 2010. Applicability and calibration of the TEX_{86} paleothermometer in lakes. *Organic Geochemistry*, **41**, 404–413, https://doi.org/10.1016/j.orggeochem.2009.11.009.

Powers, L.A., Werne, J.P., Johnson, T.C., Hopmans, E.C., Damsté, J.S.S. and Schouten, S. 2004. Crenarchaeotal membrane lipids in lake sediments: A new paleotemperature proxy for continental paleoclimate reconstruction? *Geology*, **32**, 613–616, https://doi.org/10.1130/G20434.1.

Powers, L.A., Johnson, T.C., Werne, J.P., Castañeda, I.S., Hopmans, E.C., Sinninghe Damsté, J.S. and Schouten, S. 2005. Large temperature variability in the southern African tropics since the Last Glacial Maximum. *Geophysical Research Letters*, **32**, https://doi.org/10.1029/2004GL022014.

Prahl, F.G. and Wakeham, S.G. 1987. Calibration of unsaturation patterns in long-chain ketone compositions for palaeotemperature assessment. *Nature*, **330**, 367–369, https://doi.org/10.1038/330367a0.

Prahl, F.G., Muehlhausen, L.A. and Zahnle, D.L. 1988. Further evaluation of long-chain alkenones as indicators of paleoceanographic conditions. *Geochimica et Cosmochimica Acta*, **52**, 2303–2310, https://doi.org/10.1016/0016-7037(88)90132-9.

Qin, W., Carlson, L.T., Armbrust, E.V., Devol, A.H., Moffett, J.W., Stahl, D.A. and Ingalls, A.E. 2015. Confounding effects of oxygen and temperature on the TEX$_{86}$ signature of marine Thaumarchaeota. *Proceedings of the National Academy of Sciences*, **112**, 10979–10984, https://doi.org/10.1073/pnas.1501568112.

Railsback, L.B., Gibbard, P.L., Head, M.J., Voarintsoa, N.R.G. and Toucanne, S. 2015. An optimized scheme of lettered marine isotope substages for the last 1.0 million years, and the climatostratigraphic nature of isotope stages and substages. *Quaternary Science Reviews*, **111**, 94–106, https://doi.org/10.1016/j.quascirev.2015.01.012.

Rampen, S. 2009. *Molecular Fossils of Diatoms: Applications in Petroleum Geochemistry and Palaeoenvironmental Studies*. Utrecht University.

Randlett, M.-È. 2014. *Lipid biomarkers as paleolimnological indicators in a 600 kyrs sediment record from Lake Van*. University of Quebec, Canada. Thesis.

Ravelo, A.C., Andreasen, D.H., Lyle, M., Olivarez Lyle, A. and Wara, M.W. 2004. Regional climate shifts caused by gradual global cooling in the Pliocene epoch. *Nature*, **429**, 263–267, https://doi.org/10.1038/nature02567.

Reeburgh, W.S. 2007. Oceanic Methane Biogeochemistry. *Chemical Reviews*, **107**, 486–513, https://doi.org/10.1021/cr050362v.

Riley, W.J., Subin, Z.M., *et al.* 2011. Barriers to predicting changes in global terrestrial methane fluxes: analyses using CLM4Me, a methane biogeochemistry model integrated in CESM. *Biogeosciences*, **8**, 1925–1953, https://doi.org/10.5194/bg-8-1925-2011.

Rohling, E.J., Medina-Elizalde, M., Shepherd, J.G., Siddall, M. and Stanford, J.D. 2012. Sea surface and high-latitude temperature sensitivity to radiative forcing of climate over several glacial cycles. *Journal of Climate*, **25**, 1635–1656, https://doi.org/10.1175/2011JCLI4078.1.

Rosell-Melé, A. 1998. Interhemispheric appraisal of the value of alkenone indices as temperature and salinity proxies in high-latitude locations. *Paleoceanography*, **13**, 694–703, https://doi.org/10.1029/98PA02355.

Ruan, J., Huang, Y., Shi, X., Liu, Y., Xiao, W. and Xu, Y. 2017. Holocene variability in sea surface temperature and sea ice extent in the northern Bering Sea: A multiple biomarker study. *Organic Geochemistry*, **113**, 1–9, https://doi.org/10.1016/j.orggeochem.2017.08.006.

Sangiorgi, F., Bijl, P.K., *et al.* 2018. Southern Ocean warming and Wilkes Land ice sheet retreat during the mid-Miocene. *Nature Communications*, **9**, 317, https://doi.org/10.1038/s41467-017-02609-7.

Schlung, S.A., Ravelo, A.C., *et al.* 2013. Millennial-scale climate change and intermediate water circulation in the Bering Sea from 90 ka: A high-resolution record from IODP Site U1340. *Paleoceanography*, **28**, 54–67, https://doi.org/10.1029/2012PA002365

Schmidt, G.A., Annan, J.D., *et al.* 2014. Using palaeo-climate comparisons to constrain future projections in CMIP5. *Climate of the Past*, **10**, 221–250, https://doi.org/10.5194/cp-10-221-2014.

Schneebeli-Hermann, E., Kürschner, W.M., *et al.* 2013. Evidence for atmospheric carbon injection during the end-Permian extinction. *Geology*, **41**, 579–582, https://doi.org/10.1130/G34047.1.

Schouten, S., Hoefs, M.J.L., Koopmans, M.P., Bosch, H.-J. and Sinninghe Damsté, J.S. 1998. Structural characterization, occurrence and fate of archaeal ether-bound acyclic and cyclic biphytanes and corresponding diols in sediments. *Organic Geochemistry*, **29**, 1305–1319, https://doi.org/10.1016/S0146-6380(98)00131-4.

Schouten, S., Hopmans, E.C., Pancost, R.D. and Damsté, J.S.S. 2000. Widespread occurrence of structurally diverse tetraether membrane lipids: Evidence for the ubiquitous presence of low-temperature relatives of hyperthermophiles. *Proceedings of the National Academy of Sciences*, **97**, 14421–14426, https://doi.org/10.1073/pnas.97.26.14421.

Schouten, S., Hopmans, E.C., Schefuß, E. and Sinninghe Damsté, J.S. 2002. Distributional variations in marine crenarchaeotal membrane lipids: a new tool for reconstructing ancient sea water temperatures? *Earth and Planetary Science Letters*, **204**, 265–274, https://doi.org/10.1016/S0012-821X(02)00979-2.

Schouten, S., van der Meer, M.T.J., Hopmans, E.C., Rijpstra, W.I.C., Reysenbach, A.-L., Ward, D.M. and Sinninghe Damsté, J.S. 2007. Archaeal and Bacterial Glycerol Dialkyl Glycerol Tetraether Lipids in Hot Springs of Yellowstone National Park. *Applied and Environmental Microbiology*, **73**, 6181–6191, https://doi.org/10.1128/AEM.00630-07.

Schouten, S., Hopmans, E. C., Van Der Meer, J., Mets, A., Bard, E., Bianchi, T. S., et al. 2009. An interlaboratory study of TEX_{86} and BIT analysis using high-performance liquid chromatography–mass spectrometry. *Geochemistry, Geophysics, Geosystems*, **10.** https://doi.org/10.1029/2008GC002221

Schouten, S., Hopmans, E. C., Rosell-Melé, A., Pearson, A., Adam, P., Bauersachs, T., et al. 2013. An interlaboratory study of TEX_{86} and BIT analysis of sediments, extracts, and standard mixtures. *Geochemistry, Geophysics, Geosystems*, **14,** 5263–5285. https://doi.org/10.1002/2013GC004904

Schouten, S., Hopmans, E.C. and Sinninghe Damsté, J.S. 2013. The organic geochemistry of glycerol dialkyl glycerol tetraether lipids: A review. *Organic Geochemistry*, **54**, 19–61, https://doi.org/10.1016/j.orggeochem.2012.09.006.

Schuur, E. a. G., McGuire, A.D., *et al.* 2015. Climate change and the permafrost carbon feedback. *Nature*, **520**, 171–179, https://doi.org/10.1038/nature14338.

Shah, S.R., Mollenhauer, G., Ohkouchi, N., Eglinton, T.I. and Pearson, A. 2008. Origins of archaeal tetraether lipids in sediments: Insights from radiocarbon analysis. *Geochimica et Cosmochimica Acta*, **72**, 4577–4594, https://doi.org/10.1016/j.gca.2008.06.021.

Shakun, J.D. and Carlson, A.E. 2010. A global perspective on Last Glacial Maximum to Holocene climate change. *Quaternary Science Reviews*, **29**, 1801–1816, https://doi.org/10.1016/j.quascirev.2010.03.016.

Shanahan, T.M., Hughen, K.A. and Van Mooy, B.A.S. 2013. Temperature sensitivity of branched and isoprenoid GDGTs in Arctic lakes. *Organic Geochemistry*, **64**, 119–128, https://doi.org/10.1016/j.orggeochem.2013.09.010.

Shinozaki, A. 2023. Effect of Pressure on the Thermal Cracking and Polymerization of Pentacosane (*n*-C25), an *n*-Alkane. *ACS Earth and Space Chemistry*, **7**, 69–76. https://doi.org/10.1021/acsearthspacechem.2c00235

Sicre, M.-A., Bard, E., Ezat, U. and Rostek, F. 2002. Alkenone distributions in the North Atlantic and Nordic sea surface waters. *Geochemistry, Geophysics, Geosystems*, **3**, 1 of 13–13 13, https://doi.org/10.1029/2001GC000159.

Sinninghe Damsté, J.S. and De Leeuw, J.W. 1990. Analysis, structure and geochemical significance of organically-bound sulphur in the geosphere: State of the art and future research. *Organic Geochemistry*, **16**, 1077–1101, https://doi.org/10.1016/0146-6380(90)90145-P.

Sinninghe Damsté, J.S., Hopmans, E.C., Pancost, R.D., Schouten, S. and Geenevasen, J.A.J. 2000. Newly discovered non-isoprenoid glycerol dialkyl glycerol tetraether lipids in sediments. *Chemical Communications*, 1683–1684, https://doi.org/10.1039/b004517i.

Sinninghe Damsté, J.S., Schouten, S., Hopmans, E.C., van Duin, A.C.T. and Geenevasen, J.A.J. 2002. Crenarchaeol: the characteristic core glycerol dibiphytanyl glycerol tetraether membrane lipid of cosmopolitan pelagic crenarchaeota. *Journal of Lipid Research*, **43**, 1641–1651, https://doi.org/10.1194/jlr.M200148-JLR200.

Sinninghe Damsté, J.S., Ossebaar, J., Schouten, S. and Verschuren, D. 2012. Distribution of tetraether lipids in the 25-ka sedimentary record of Lake Challa: extracting reliable TEX_{86} and MBT/CBT palaeotemperatures from an equatorial African lake. *Quaternary Science Reviews*, **50**, 43–54, https://doi.org/10.1016/j.quascirev.2012.07.001.

Sluijs, A., Brinkhuis, H., *et al.* 2008. Eustatic variations during the Paleocene-Eocene greenhouse world. *Paleoceanography*, **23**, https://doi.org/10.1029/2008PA001615.

Sluijs, A., Frieling, J., Inglis, G.N., Nierop, K.G.J., Peterse, F., Sangiorgi, F. and Schouten, S. 2020. Late Paleocene–early Eocene Arctic Ocean sea surface temperatures: reassessing biomarker paleothermometry at Lomonosov Ridge. *Climate of the Past*, **16**, 2381–2400, https://doi.org/10.5194/cp-16-2381-2020.

Smith, D.M., Screen, J.A., *et al.* 2019. The Polar Amplification Model Intercomparison Project (PAMIP) contribution to CMIP6: investigating the causes and consequences of polar amplification. *Geoscientific Model Development*, **12**, 1139–1164, https://doi.org/10.5194/gmd-12-1139-2019.

Smith, L.C. 2004. Siberian peatlands a net carbon sink and global methane source since the early Holocene. *Science*, **303**, 353–356, https://doi.org/10.1126/science.1090553.

Sonzogni, C., Bard, E., Rostek, F., Dollfus, D., Rosell-Melé, A. and Eglinton, G. 1997. Temperature and salinity effects on alkenone ratios measured in surface sediments from the Indian Ocean. *Quaternary Research*, **47**, 344–355, https://doi.org/10.1006/qres.1997.1885.

Spang, A., Martijn, J., Saw, J.H., Lind, A.E., Guy, L. and Ettema, T.J.G. 2013. Close Encounters of the Third Domain: The Emerging Genomic View of Archaeal Diversity and Evolution. *Archaea*, **2013**, 202358, https://doi.org/10.1155/2013/202358.

Sparkes, R. B., Doğrul Selver, A., Bischoff, J., Talbot, H. M., Gustafsson, Ö., Semiletov, I. P., et al. 2015. GDGT distributions on the East Siberian Arctic Shelf: implications for organic carbon export, burial and degradation. *Biogeosciences*, **12,** 3753–3768. https://doi.org/10.5194/bg-12-3753-2015

Stabeno, P.J., Schumacher, J.D. and Ohtani, K. 1999. The physical oceanography of the Bering Sea. *In*: *Dynamics of the Bering Sea: A Summary of Physical, Chemical, and Biological Characteristics, and a Synopsis of Research on the Bering Sea*. 1–28.

Stroynowski, Z., Ravelo, A.C. and Andreasen, D. 2015. A Pliocene to recent history of the Bering Sea at Site U1340A, IODP Expedition 323. *Paleoceanography*, **30**, 1641–1656, https://doi.org/10.1002/2015PA002866.

Sun, Q., Chu, G., *et al.* 2011. Distributions and temperature dependence of branched glycerol dialkyl glycerol tetraethers in recent lacustrine sediments from China and Nepal. *Journal of Geophysical Research: Biogeosciences*, **116**, https://doi.org/10.1029/2010JG001365.

Swindles, G.T., Morris, P.J., *et al.* 2015. The long-term fate of permafrost peatlands under rapid climate warming. *Scientific Reports*, **5**, 17951, https://doi.org/10.1038/srep17951.

Takahashi, K., Fujitani, N. and Yanada, M. 2002. Long term monitoring of particle fluxes in the Bering Sea and the central subarctic Pacific Ocean, 1990–2000. *Progress in Oceanography*, **55**, 95–112, https://doi.org/10.1016/S0079-6611(02)00072-1.

Takahashi, K., Ravelo, A.C. and Alvarez Zarikian, C.A. 2009. Pliocene–Pleistocene paleoceanography and climate history of the Bering Sea. *In*: *IODP Scientific Prospectus 323*. IODP Scientific Prospectus**323**., https://doi.org/10.2204/iodp.sp.323.2009.

Takahashi, K., Ravelo, A.C. and Alvarez Zarikian, C. 2011. IODP Expedition 323—Pliocene and Pleistocene Paleoceanographic Changes in the Bering Sea. *Scientific Drilling*, https://doi.org/10.2204/iodp.sd.11.01.2011.

Taylor, K.W.R., Huber, M., Hollis, C.J., Hernandez-Sanchez, M.T. and Pancost, R.D. 2013. Re-evaluating modern and Palaeogene GDGT distributions: Implications for SST reconstructions. *Global and Planetary Change*, **108**, 158–174, https://doi.org/10.1016/j.gloplacha.2013.06.011.

Thomas, D.N., Arévalo-Martínez, D.L., *et al.* 2022. A changing Arctic Ocean. *Ambio*, **51**, 293–297, https://doi.org/10.1007/s13280-021-01677-w.

Thompson, M., Gamage, D., Hirotsu, N., Martin, A., & Seneweera, S. 2017. Effects of Elevated Carbon Dioxide on Photosynthesis and Carbon Partitioning: A Perspective on Root Sugar Sensing and Hormonal Crosstalk. *Frontiers in Physiology*, **8.** https://doi.org/10.3389/fphys.2017.00578.

Tierney, J.E. and Russell, J.M. 2009. Distributions of branched GDGTs in a tropical lake system: Implications for lacustrine application of the MBT/CBT paleoproxy. *Organic Geochemistry*, **40**, 1032–1036, https://doi.org/10.1016/j.orggeochem.2009.04.014.

Tierney, J. E., & Tingley, M. P. 2015. A TEX$_{86}$ surface sediment database and extended Bayesian calibration. *Scientific Data*, **2**. https://doi.org/10.1038/sdata.2015.29

Tierney, J.E., Zhu, J., King, J., Malevich, S.B., Hakim, G.J. and Poulsen, C.J. 2020. Glacial cooling and climate sensitivity revisited. *Nature*, **584**, 569–573, https://doi.org/10.1038/s41586-020-2617-x.

Turich, C., Schouten, S., Thunell, R.C., Varela, R., Astor, Y. and Wakeham, S.G. 2013. Comparison of TEX$_{86}$ and U$_{37}^{K'}$ temperature proxies in sinking particles in the Cariaco Basin. *Deep Sea Research Part I: Oceanographic Research Papers*, **78**, 115–133, https://doi.org/10.1016/j.dsr.2013.02.008.

van Bree, L.G.J., Peterse, F., *et al.* 2020. Seasonal variability and sources of in situ brGDGT production in a permanently stratified African crater lake. *Biogeosciences*, **17**, 5443–5463, https://doi.org/10.5194/bg-17-5443-2020.

Vickers, M.L., Lengger, S.K., *et al.* 2020. Cold spells in the Nordic Seas during the early Eocene Greenhouse. *Nature Communications*, **11**, 4713, https://doi.org/10.1038/s41467-020-18558-7.

Voigt, C., Marushchak, M.E., *et al.* 2019. Ecosystem carbon response of an Arctic peatland to simulated permafrost thaw. *Global Change Biology*, **25**, 1746–1764, https://doi.org/10.1111/gcb.14574.

Vonk, J., and Gustafsson, O. 2013. Permafrost-carbon complexities. *Nature Geoscience*, **6**, https://doi.org/10.1038/ngeo1937.

Wagner, B., Ortlepp, S., Doran, P.T., Kenig, F., Melles, M. and Burkemper, A. 2011. The Holocene environmental history of Lake Hoare, Taylor Valley, Antarctica, reconstructed from sediment cores. *Antarctic Science*, **23**, 307–319, https://doi.org/10.1017/S0954102011000125.

Wang, K.J., Huang, Y., *et al.* 2021. Group 2i Isochrysidales produce characteristic alkenones reflecting sea ice distribution. *Nature Communications*, **12**, 15, https://doi.org/10.1038/s41467-020-20187-z.

Weijers, J.W.H., Schouten, S., *et al*. 2006a. Membrane lipids of mesophilic anaerobic bacteria thriving in peats have typical archaeal traits. *Environmental Microbiology*, **8**, 648–657, https://doi.org/10.1111/j.1462-2920.2005.00941.x.

Weijers, J.W.H., Schouten, S., Spaargaren, O.C. and Sinninghe Damsté, J.S. 2006b. Occurrence and distribution of tetraether membrane lipids in soils: Implications for the use of the TEX_{86} proxy and the BIT index. *Organic Geochemistry*, **37**, 1680–1693, https://doi.org/10.1016/j.orggeochem.2006.07.018.

Weijers, J.W.H., Schouten, S., van den Donker, J.C., Hopmans, E.C. and Sinninghe Damsté, J.S. 2007a. Environmental controls on bacterial tetraether membrane lipid distribution in soils. *Geochimica et Cosmochimica Acta*, **71**, 703–713, https://doi.org/10.1016/j.gca.2006.10.003.

Weijers, J.W.H., Schouten, S., Sluijs, A., Brinkhuis, H. and Sinninghe Damsté, J.S. 2007b. Warm arctic continents during the Palaeocene–Eocene thermal maximum. *Earth and Planetary Science Letters*, **261**, 230–238, https://doi.org/10.1016/j.epsl.2007.06.033.

Wenban-Smith, F., Bates, M., Bridgeland, D., Harp, P., Pope, M. and Roberts, M. 2010. *South-East Region Research Frameworks: The Early Palaeolithic: Resource Assessment and Research Agenda. Kent County Council.*

Westbrook, R.E. 2014. *Evidence for a Glacial Refugium in South-Central Beringia Using Modern Analogs: A 152.2 Kyr Palynological Record from IODP Expedition 323 Sediment*. A Thesis, University of Alaska.

Wied, A. 2017. *Different Environmental Stressors and Their Effect on TEX$_{86}$ Signature of Marine Ammonia-Oxidizing Archaea*. Thesis, University of Washington.

Woese, C.R. 1987. Bacterial evolution. *Microbiological Reviews*, **51**, 221–271, https://doi.org/10.1128/mr.51.2.221-271.1987.

Woese, C.R. and Fox, G.E. 1977. Phylogenetic structure of the prokaryotic domain: The primary kingdoms. *Proceedings of the National Academy of Sciences*, **74**, 5088–5090, https://doi.org/10.1073/pnas.74.11.5088.

Woltering, M., Atahan, P., Grice, K., Heijnis, H., Taffs, K. and Dodson, J. 2014. Glacial and Holocene terrestrial temperature variability in subtropical east Australia as inferred from branched GDGT distributions in a sediment core from Lake McKenzie. *Quaternary Research*, **82**, 132–145, https://doi.org/10.1016/j.yqres.2014.02.005.

Woodgate, R.A., Weingartner, T.J. and Lindsay, R. 2012. Observed increases in Bering Strait oceanic fluxes from the Pacific to the Arctic from 2001 to 2011 and their impacts on the Arctic Ocean water column. *Geophysical Research Letters*, **39**, https://doi.org/10.1029/2012GL054092.

Worne, S. 2022. Updated age-depth ties for U1343. Email to Lauren Pankhurst, 13 June.

Worne, S., Kender, S., Swann, G.E.A., Leng, M.J. and Ravelo, A.C. 2019. Coupled climate and subarctic Pacific nutrient upwelling over the last 850,000 years. *Earth and Planetary Science Letters*, **522**, 87–97, https://doi.org/10.1016/j.epsl.2019.06.028.

Worne, S., Stroynowski, Z., Kender, S. and Swann, G.E.A. 2021. Sea-ice response to climate change in the Bering Sea during the Mid-Pleistocene Transition. *Quaternary Science Reviews*, **259**, 106918, https://doi.org/10.1016/j.quascirev.2021.106918.

Yang, G., Zhang, C.L., Xie, S., Chen, Z., Gao, M., Ge, Z. and Yang, Z. 2013. Microbial glycerol dialkyl glycerol tetraethers from river water and soil near the Three Gorges Dam on the Yangtze River. *Organic Geochemistry*, **56**, 40–50, https://doi.org/10.1016/j.orggeochem.2012.11.014.

Yang, Y., Saatchi, S.S., *et al.* 2018. Post-drought decline of the Amazon carbon sink. *Nature Communications*, **9**, 3172, https://doi.org/10.1038/s41467-018-05668-6.

Yang, Y., Zhang, C., *et al.* 2021. The Evolution Pathway of Ammonia-Oxidizing Archaea Shaped by Major Geological Events. *Molecular Biology and Evolution*, **38**, 3637–3648, https://doi.org/10.1093/molbev/msab129.

Yu, Z., Loisel, J., Brosseau, D.P., Beilman, D.W. and Hunt, S.J. 2010. Global peatland dynamics since the Last Glacial Maximum. *Geophysical Research Letters*, **37**, https://doi.org/10.1029/2010GL043584.

Zachos, J.C., Wara, M.W., *et al.* 2003. A transient rise in tropical sea surface temperature during the Paleocene-Eocene Thermal Maximum. *Science*, **302**, 1551–1554, https://doi.org/10.1126/science.1090110.

Zachos, J.C., Röhl, U., *et al.* 2005. Rapid Acidification of the Ocean During the Paleocene-Eocene Thermal Maximum. *Science*, **308**, 1611–1615, https://doi.org/10.1126/science.1109004.

Zachos, J.C., Schouten, S., *et al.* 2006. Extreme warming of mid-latitude coastal ocean during the Paleocene-Eocene Thermal Maximum: Inferences from TEX_{86} and Isotope Data. *Geology*, **34**, https://doi.org/10.1130/G22522.1.

Zell, C., Kim, J.-H., Abril, G., Sobrinho, R.L., Dorhout, D., Moreira-Turcq, P. and Sinninghe Damsté, J.S. 2013. Impact of seasonal hydrological variation on the distributions of tetraether lipids along the Amazon River in the central Amazon basin: implications for the MBT/CBT paleothermometer and the BIT index. *Frontiers in Microbiology*, **4**, 228, https://doi.org/10.3389/fmicb.2013.00228.

Zeng, Z., Chen, H., *et al.* 2022. Identification of a protein responsible for the synthesis of archaeal membrane-spanning GDGT lipids. *Nature Communications*, **13**, 1545, https://doi.org/10.1038/s41467-022-29264-x.

Zhang, F., Algeo, T.J., Romaniello, S.J., Cui, Y., Zhao, L., Chen, Z.-Q. and Anbar, A.D. 2018. Congruent Permian-Triassic δ^{238}U records at Panthalassic and Tethyan sites: Confirmation of global-oceanic anoxia and validation of the U-isotope paleoredox proxy. *Geology*, **46**, 327–330, https://doi.org/10.1130/G39695.1.

Zhang, Y. G., Zhang, C. L., Liu, X.-L., Li, L., Hinrichs, K.-U., & Noakes, J. E. 2011. Methane Index: A tetraether archaeal lipid biomarker indicator for detecting the instability of marine gas hydrates. *Earth and Planetary Science Letters*, **307**, 525–534. https://doi.org/10.1016/j.epsl.2011.05.031

Zhang, Y.G., Pagani, M., Liu, Z., Bohaty, S.M. and DeConto, R. 2013. A 40-million-year history of atmospheric CO_2. *Philosophical Transactions of the Royal Society A: Mathematical, Physical and Engineering Sciences*, **371**, 20130096, https://doi.org/10.1098/rsta.2013.0096.

Zhang, Y.G., Pagani, M. and Wang, Z. 2016. Ring Index: A new strategy to evaluate the integrity of TEX_{86} paleothermometry. *Paleoceanography*, **31**, 220–232, https://doi.org/10.1002/2015PA002848.

Zhang, Z., Wagner, S., Klockmann, M. and Zorita, E. 2022. *Evaluation of Statistical Climate Reconstruction Methods Based on Pseudoproxy Experiments Using Linear and Machine Learning Methods*. Preprint, https://doi.org/10.5194/cp-2022-5.

Zink, K.-G., Vandergoes, M.J., Mangelsdorf, K., Dieffenbacher-Krall, A.C. and Schwark, L. 2010. Application of bacterial glycerol dialkyl glycerol tetraethers (GDGTs) to develop modern and past temperature estimates from New Zealand lakes. *Organic Geochemistry*, **41**, 1060–1066, https://doi.org/10.1016/j.orggeochem.2010.03.004.

Appendix A

Table A.1. GDGT extraction methods used in previous studies (2000-2022). Modified from Foster (2015).

Study	Sample Size	Sediment Preparation	Extraction Method and Solvent	Column and Solvent	Final Dilution Solvent	Filter Size / µm	Standard Used
Hopmans *et al.* (2000)		Freeze-dried	Ultrasonic: 3× DCM:MeOH (1:1) and 3× DCM		Hexane:IPA (99:1)	0.45	
Schouten *et al.* (2000)	1-5 g	Freeze-dried	Ultrasonic: 3× DCM:MeOH (1:1) and 3× DCM		Hexane:IPA (99:1)	0.45	
Schouten *et al.* (2002)		Freeze-dried	Ultrasonic: 3× DCM:MeOH (1:1) and 3× DCM	Alumina Column DCM:MeOH (1:1)	Hexane:IPA (99:1)	0.45	
Sinninghe Damsté *et al.* (2002)			Soxhlet: DCM:MeOH (9:1)	Alumina Column DCM:MeOH (1:1)	Hexane:IPA (99:1)	0.45	
Hopmans *et al.* (2004)			Ultrasonic: 3× DCM:MeOH (1:1) and 3× DCM	Alumina Column DCM:MeOH (1:1)	Hexane:IPA (99:1)	0.45	
Powers *et al.* (2004)	5-10 g	Freeze-dried, Homogenised	Soxhlet: DCM:MeOH (2:1)	Alumina Column DCM:MeOH (1:1)	Hexane:IPA (99:1)		
Powers *et al.* (2005)	1-3 g	Freeze-dried, Homogenised	Soxhlet or ASE: DCM:MeOH (2:1)	Alumina Column DCM:MeOH (1:1)	Hexane:IPA (99:1)	0.45	
Weijers *et al.* (2006b)		Freeze-dried	ASE: DCM:MeOH (9:1)	Alumina Column DCM:MeOH (1:1)	Hexane:IPA (99:1)	0.45	
Weijers *et al.* (2007a)		Freeze-dried, Homogenised	ASE: DCM:MeOH (9:1)	Alumina Column DCM:MeOH (1:1)	Hexane:IPA (99:1)	0.45	
Blaga *et al.* (2009)		Freeze-dried, Homogenised	Ultrasonic: 3× DCM:MeOH (1:1) and 3× DCM then ASE: DCM:MeOH (9:1)	Alumina Column DCM:MeOH (1:1)	Hexane:IPA (99:1)	0.45	
Tierney & Russell (2009)		Freeze-dried, Homogenised	ASE: DCM:MeOH (9:1)	Alumina Column DCM:MeOH (1:1)	Hexane:IPA (99:1)	0.45	C_{46}
Bechtel *et al.* (2010)			MAE: 70 °C for 7 min DCM:MeOH (9:1)		Hexane:IPA (99:1)	0.45	C_{46}
Blaga *et al.* (2010)			ASE: DCM:MeOH (9:1)	Alumina Column DCM:MeOH (1:1)	Hexane:IPA (99:1)	0.45	
Kim *et al.* (2010)		Freeze-dried, Homogenised	ASE: DCM:MeOH (9:1)	Alumina Column DCM:MeOH (1:1)	Hexane:IPA (99:1)	0.4	
Powers *et al.* (2010)		Freeze-dried, Homogenised	Soxhlet or ASE: DCM:MeOH (2:1)	Alumina Column DCM:MeOH (1:1)	Hexane:IPA (99:1)	0.4	
Zink *et al* (2010)			ASE: DCM:MeOH (1:1)	Alumina Column DCM:MeOH (1:1)	Hexane:IPA (99:1)	0.45	
Pearson *et al.* (2011)	0.1-2 g		MAE: 70 °C ramp for 2 min and held for 5 min DCM:MeOH (9:1)		Hexane:IPA (99:1)	0.45	
Sun *et al.* (2011)		Freeze-dried, Homogenised	ASE: DCM:MeOH (9:1)	Alumina Column DCM:MeOH (1:1)	Hexane:IPA (98:2)	0.45	
Loomis *et al.* (2012)	0.02-2.2 g	Freeze-dried, Homogenised	ASE: DCM:MeOH (9:1)				C_{46}
Sinninghe Damsté *et al.* (2012)	1-3 g	Freeze-dried, Homogenised	ASE				
Shanahan *et al.* (2013)	1-5 g	Freeze-dried	ASE: DCM:MeOH (9:1)		Hexane:IPA (99:1)		
Woltering *et al.* (2014)	1-5 g	Freeze-dried	ASE: DCM:MeOH (9:1)	Alumina Column DCM:MeOH (1:1)	Hexane:IPA (99:1)	0.45	
De Jonge *et al.* (2014)		Freeze-dried, Homogenised	ASE: DCM:MeOH (9:1)	Alumina Column DCM:MeOH (1:1)	Hexane:IPA (99:1)	0.45	
Foster *et al.* (2015)	0.1-4.6 g	Freeze-dried, Homogenised	MAE: 70 °C ramp for 3 min and held for 5 min DCM:MeOH (9:1)		Hexane:IPA (99:1)	0.2	
Lei *et al.* (2016)	20 g	Freeze-dried, Homogenised	ASE: DCM:MeOH (9:1)	Silica Column MeOH	Hexane:EtOAc (84:16)	0.45	C_{46}
Ruan *et al.* (2017)	4-6 g	Freeze-dried, Homogenised	Ultrasonic: 3× DCM:MeOH (2:1)	Silica Column DCM:MeOH (1:1)	Hexane:IPA (99:1)	0.45	C_{46}
Dearing Crampton-Flood *et al.* (2020)		Freeze-dried, Homogenised	ASE: DCM:MeOH (9:1)	Alumina Column DCM:MeOH (1:1)	Hexane:IPA (99:1)	0.45	C_{46}
Lawrence *et al.* (2020)	~2 g	Freeze-dried	ASE: DCM	Alumina Column DCM:MeOH (1:1)		0.45	
Vickers *et al.* (2020)	~ 30 g	Freeze-dried, Homogenised	Soxhlet: DCM:MEOH (2:1)				
Peaple *et al.* (2022)	26-85 g	Freeze-dried	ASE		Hexane:IPA (99:1)	0.45	